

**INTEGRATED ARRAY TOMOGRAPHY:  
DEVELOPMENT AND APPLICATIONS OF A WORKFLOW  
FOR 3D CORRELATIVE LIGHT AND ELECTRON  
MICROSCOPY**



**INTEGRATED ARRAY TOMOGRAPHY:  
EVELOPMENT AND APPLICATIONS OF A WORKFLOW  
FOR 3D CORRELATIVE LIGHT AND ELECTRON  
MICROSCOPY**

**Proefschrift**

ter verkrijging van de graad van doctor  
aan de Technische Universiteit Delft,  
op gezag van de Rector Magnificus Prof. dr. ir. T.H.J.J. van der Hagen,  
voorzitter van het College voor Promoties,  
in het openbaar te verdedigen op dinsdag 1 januari 2022 om 10:00 uur

door

**Ryan LANE**

Master of Science in Physics,  
University of Oregon, Verenigde Staten van Amerika,  
geboren te Carlisle, Verenigde Staten van Amerika.

Dit proefschrift is goedgekeurd door de promotoren.

Samenstelling promotiecommissie:

Rector Magnificus,	voorzitter
Dr. ir. J.P. Hoogenboom,	Technische Universiteit Delft, promotor
Dr. E.C.M. Carroll,	Technische Universiteit Delft, copromotor

*Onafhankelijke leden:*

Prof. dr. A. Jansen	Technische Universiteit Delft
Prof. dr. ir. A.B.C.D. van de Lange-Achternaam	Technische Universiteit Delft
Prof. dr. N. Nescio	Politecnico di Milano, Italië
Prof. dr. ir. J. Doe,	Technische Universiteit Delft, reservelid

*Overige leden:*

Prof. dr. ir. J. de Wit,	Technische Universiteit Delft
Dr. ir. Q. de Zwart,	Technische Universiteit Eindhoven

**delmic** **Genentech**



*Keywords:* ...

*Printed by:* Johannes Gutenberg

*Front & Back:* Beautiful cover art that captures the entire content of this thesis in a single illustration.

*Funding:* This project was financially supported by the Building Blocks of Life (BBoL) program of the Netherlands Organization for Scientific Research (NWO), with cash and in-kind contributions from Delmic B.V. and Genentech.

Copyright © 2022 by R. Lane

ISBN 000-00-0000-000-0

An electronic version of this dissertation is available at  
<http://repository.tudelft.nl/>.

## Propositions

1. Researchers conducting SEM-based backscattered electron imaging of biological tissue without the use of a negative potential bias are (literally) wasting time.  
*This proposition pertains to this dissertation.*
2. Integrated array tomography is the most viable solution for acquiring large-scale correlative light and electron microscopy datasets with sub-micron registration precision.  
*This proposition pertains to this dissertation.*
3. By mitigating nonspecific labeling artefacts and correcting for registration errors, neural networks trained on correlative light and electron microscopy data are capable of providing higher quality fluorescence information than fluorescence microscopes.  
*This proposition pertains to this dissertation.*
4. The future of correlative light and electron microscopy relies on improved protocols for sample preparation rather than instrumentation.  
*This proposition pertains to this dissertation.*
5. The next revolution in dense reconstruction of biological specimens will come from X-ray nano-tomography.
6. By manufacturing women's clothing with impractical or nonexistent pockets, the fashion industry has exploited women into the purchasing of hand bags.
7. If intelligent lifeforms existed elsewhere in our galaxy, we would be aware of them by now.
8. Humanity and asteroids pose the two greatest existential threats to our planet; the best way to ensure the survival of our planet is therefore for all humans not contributing to an asteroid-detonation strategy to die.
9. Art is not open to interpretation; it means precisely what the artist meant it to and nothing more.
10. Inaccessibility of glass recycling facilities undermines the “green” credentials of TU Delft.

# CONTENTS

<b>1</b>	<b>Introduction</b>	<b>1</b>
1.1	So you want to know how the brain works? . . . . .	1
1.2	Volume electron microscopy . . . . .	2
1.3	Correlative light and electron microscopy . . . . .	2
1.4	Integrated microscopy . . . . .	3
1.5	Integrated correlative array tomography . . . . .	4
<b>2</b>	<b>Optimization of negative stage bias potential</b>	<b>9</b>
2.1	Introduction . . . . .	10
2.2	Results . . . . .	11
2.2.1	Negative bias potential enhances signal in routine EM samples . . . . .	11
2.2.2	Simulating signal electron trajectories with and without negative potential bias. . . . .	13
2.2.3	Experimental optimization of negative potential bias leads to increased throughput. . . . .	15
2.2.4	Potential bias allows for higher throughput EM and CLEM acquisitions. . . . .	16
2.3	Discussion . . . . .	18
2.4	Material & methods . . . . .	22
2.4.1	Modeling . . . . .	22
2.4.2	Tissue and sample preparation . . . . .	23
2.4.3	Signal-to-noise measurements . . . . .	23
2.4.4	Integrated microscopy workflow . . . . .	24
2.4.5	Reconstruction . . . . .	25
2.A	Supplementary material . . . . .	26
2.A.1	test subsection . . . . .	26
<b>3</b>	<b>Integrated array tomography</b>	<b>30</b>
3.1	Introduction . . . . .	31
3.2	Material & methods . . . . .	32
3.2.1	Tissue and sample preparation . . . . .	32
3.2.2	Digital light microscopy . . . . .	32
3.2.3	Integrated microscopy . . . . .	32
3.2.4	Alignment and reconstruction software . . . . .	33

3.3	Results . . . . .	33
3.3.1	Section detection and <i>in-situ</i> navigation . . . . .	33
3.3.2	Targeted correlative acquisition of an individual region of interest . . . . .	35
3.3.3	2D Stitching and correlation . . . . .	35
3.3.4	Correlative 3D reconstruction . . . . .	38
3.3.5	Proof of concept on zebrafish pancreas tissue . . . . .	39
3.4	Discussion . . . . .	41
3.5	Supplementary material . . . . .	44
<b>4</b>	<b>Label-free fluorescence predictions</b>	<b>50</b>
4.1	Introduction . . . . .	51
4.2	Results . . . . .	52
4.2.1	Network overview . . . . .	52
4.2.2	Network predictions on thin tissue sections . . . . .	52
4.2.3	Human evaluation of fluorescence vs label-free prediction . . . . .	53
4.2.4	Network robustness . . . . .	55
4.2.5	Weakly supervised, semi-automated segmentation . . . . .	57
4.3	Discussion . . . . .	60
4.4	Methods . . . . .	62
4.4.1	Tissue and sample preparation . . . . .	62
4.4.2	CLEMnet architecture . . . . .	62
4.4.3	Data acquisition . . . . .	63
4.4.4	Robustness & validation . . . . .	64
4.4.5	Quantitative analysis . . . . .	67
4.4.6	Segmentation . . . . .	68
4.5	Supplementary material . . . . .	72
<b>5</b>	<b>Valorisation, outlook, and conclusion</b>	<b>77</b>
5.1	Prospects for integrated array tomography . . . . .	77
5.2	Applications for multibeam SEM . . . . .	80
5.3	Conclusion . . . . .	81
<b>A</b>	<b>Automatic focusing of the fluorescence microscope</b>	<b>85</b>
1.1	Original autofocus implementation . . . . .	85
1.2	Analysis of FM focus sweeps . . . . .	87



# 1

## INTRODUCTION

### 1.1. So you want to know how the brain works?

How a convoluted network of synapses can enable an animal to think and exhibit complex behavior has been a motivating question of neuroscience since the discovery of neurons in the late 19<sup>th</sup> century [2, 3]. Neuronal circuit diagrams, maps delineating the connections between synapses, have shown to be useful tools for better understanding cognitive function and neural architecture [4, 5]. Although several full brain circuit diagrams have been completed (*C. elegans* [6], fruit fly larva [7], tunicate tadpole larva [8], zebrafish larva [9], and adult fruit fly [10]), such “connectomes” are a herculean task given that the resolution required to discern synapses is on the nanometer scale, while the organ as a whole spans millimeters or larger, depending on the organism [11, 12, 13]. Electron microscopy (EM), an imaging technique able to reach magnification scales several orders of magnitude higher than light microscopy by illuminating a specimen with a beam of accelerated electrons, is currently the only imaging method capable of resolving such fine features across such vast spatial extents [4, 10]. The drawback for high-magnification imaging over organ-scale dimensions is, however, the inherently limited throughput, leading to hours or days of acquisition time for a single two-dimensional cross section. Extending acquisitions of biological material to the third dimension has long remained a challenge for EM.

While the brain is perhaps the most prominent, it is certainly not the only example in biology where multi-scale microscopy can assist in mapping connectivity relations crucial to functional performance. Molecular-scale processes taking place within cells or organelles are highly regulated in health, and defects or deviations at the smallest scales can lead to dysfunction or disease at the organ or organism level. Simply put, the big things are made out of lots of little things, and to figure out how the big thing works, you have to look at all the little things. EM

---

Parts of this chapter have been published in: RI Koning et al. “Integrated Light and Electron Microscopy”. *Correlative Imaging: Focusing on the Future* (2019), pp. 119–135.

is the only technique that can see the littlest things and that might do this over the full size of the big things.

## 1.2. Volume electron microscopy

There are a variety of techniques for three-dimensional imaging of biological specimen via electron microscopy (EM) [14]. Modern volume EM techniques can be divided into two broader methods: array tomography approaches, in which ultrathin serial sections are cut from a block of tissue prior to EM (e.g. serial section scanning EM or transmission EM), and blockface approaches, in which the tissue block is sectioned as it is imaged (e.g. serial blockface or focused ion beam SEM). While both of these approaches have their respective advantages and disadvantages [15, 14], an important distinction is that array tomography allows for re-evaluation of sections whereas the specimen is irrevocably lost in blockface approaches [16].

Despite the success these techniques have had in generating high-quality three-dimensional reconstructions, significant challenges remain. At present, one of the most stringent constraints facing high-resolution (< 10 nm) volume EM is throughput. To scan an entire mouse cortical column, for example, a  $400 \times 400 \times 1000 \mu\text{m}^3$  volume, at 4 nm/px with 30 nm section thickness (the resolution necessary to reliably discern synapses [17, 18]), Briggman and Bock [15] estimated that it would require ~500 days of uninterrupted imaging with a single beam. For this reason, it is advantageous to locate regions of interest prior to large-scale EM in order to minimize the imaging volume.

One approach, taken by Hildebrand et al. [9] for whole-brain serial section SEM reconstruction of a larval zebrafish, was to utilize multiple rounds of targeted EM at successively higher levels of magnification. Similar approaches have been taken in other large-scale neural reconstruction endeavors such as partial brain imaging of a mouse visual cortex [12] and full brain imaging of an adult fruit fly [10] where certain synapses were re-imaged at higher resolution. Although these multiscale approaches have been implemented with great success, the need for intermediate analysis of the EM dataset hinders throughput. The selection of sub-regions of interest for subsequent imaging rounds is driven by localization of the biological material of interest, which can only be done after manual or machine-learning-assisted analysis of the preceding EM dataset. While machine-learning techniques have made tremendous progress in reducing human involvement, interpretation and annotation of EM datasets remain a tedious and error-prone practice. These methods are therefore not yet appropriate for selecting sub-regions at higher magnification scales, meaning selection cannot be done either automatically or in real time.

## 1.3. Correlative light and electron microscopy

In addition to low throughput, EM has the additional limitation that it does not contain the protein- and molecular-specific information available from fluorescence microscopy (FM)—unless the proteins are known to be specifically linked

to a structural component. This information is not only crucial for understanding biological function but can also be used to guide to regions of interest (ROI) based on molecular expression. Thus, while EM is successful at providing ultrastructural information, it is not always useful for localizing ROIs. Functional fluorescence microscopy has been employed to identify the biological material of interest, particularly in blockface approaches [19]. However, workflows to retrieve selected regions from the specimen and trim the block to the appropriate size can be both complicated and time-consuming or involve further rounds of multimodal inspection, e.g. with X-ray tomography [20]. Linking between the structural information conveyed by EM and the dynamic, functional data obtained with live-cell FM can furthermore be challenging when EM is performed following FM and the intermediate sample preparation [21].

As the advantages afforded by merging targeted biological information with ultrastructural detail often outweigh the challenges, methods have been developed for combining FM and EM in correlative light and electron microscopy (CLEM). In the past decades, CLEM has evolved from being used by only a few pioneering, specialist labs to a collection of techniques and workflows practiced by a broad group of researchers in structural biology [21, 22]. In most cases, CLEM involves a distinct set of sequentially used specimen preparation and labeling techniques, followed by diverse types of light and electron microscopy techniques, with specific workflows for sample transfer and relocation of regions of interest. A key advantage of sequential CLEM is the wide diversity of available microscopes: in principle, any type of microscope can be added to the workflow, provided requirements on sample preparation and handling can be met. Procedures to combine different light and electron microscopes can, however, be tedious, involving extensive manual labor, transfers, and cumbersome ROI retrieval.

## 1.4. Integrated microscopy

Microscopes that integrate a light and an electron microscope in one have been developed as early as the 1980s and a wide variety of integrated microscopes with different modalities has been reported in literature in recent years [23, 24]. Several of these have now also become commercially available. For a specific CLEM experiment, the choice between an experimental workflow with standalone microscopes or with an integrated microscope depends on a variety of factors: the precise goal and requirements of the experiment, amenable sample preparation protocols, and local availability of microscopes, probes, and expertise. If only a single or very few samples have to be carried through the CLEM workflow, adopting sample preparation protocols towards integrated inspection may not be worth the effort. On the other hand, integrated microscopes offer advantages in terms of throughput, avoiding sample contamination, achievable precision of ROI retrieval, and ease and accuracy of image correlation.

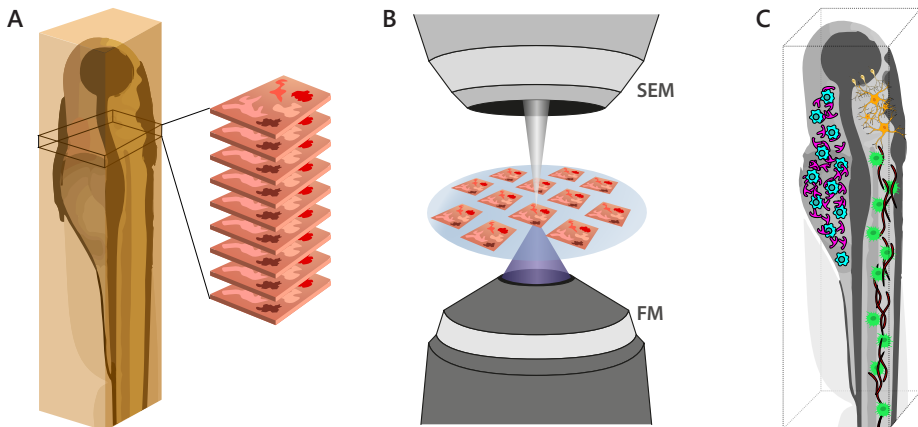


**Figure 1.1.** Conceptual overview of the integrated array tomography workflow. (A) Serial sections are cut from a resin-embedded specimen; a larval zebrafish is illustrated here as an example. (B) The sections are placed onto an ITO-coated glass slide which is mounted onto the translation stage of the integrated microscope. A series of registered EM-FM image pairs are acquired according to a semi-automated imaging pipeline. (C) The EM images are computationally aligned in 3D, revealing the structure of the zebrafish. The fluorescence data, comprising the targeted organelles, proteins, or biomolecules, is then overlaid onto the EM, resulting in a volume CLEM reconstruction of the zebrafish. Larval zebrafish illustration derived from original artwork by Lizzy Griffiths.

## 1.5. Integrated correlative array tomography

The advantages offered by integrated microscopy extend to volume imaging. In conventional array tomography, a tissue specimen is chemically fixed, embedded in resin, and cut into a series of ultrathin sections which are collected as ribbons on a solid substrate or on flexible, sticky Kapton tape. The sections are then immunostained for imaging in a widefield or confocal fluorescence microscope, possibly in several rounds to target multiple molecules. Next, the sections are washed and reprocessed for EM with e.g. osmium tetroxide or uranyl acetate and transferred to a scanning or transmission electron microscope [25, 26]. Integrated array tomography seeks to advance this workflow by combining FM and EM acquisition with the high alignment accuracy and automation afforded by an integrated light and electron microscope. While the need for intermediate sample preparation is removed, it does, however, impose stricter constraints on the amount of heavy metal staining that can be used for EM to avoid quenching fluorophores [27, 28]. To circumvent the loss of signal without increasing the dwell time, a negative bias potential can be used to enhance the collection of backscattered electrons (Chapter 2).

The workflow for integrated correlative array tomography (iCAT; Fig. 1.1) begins by following a customized protocol for fixating, embedding, cutting, and im-

munolabeling a sample such that the fluorescence is maintained. Serial sections are then loaded into the integrated microscope and imaged sequentially, while an automated procedure for EM-FM registration [29] ensures consistent overlay accuracy. Custom-built alignment routines are then used to reconstruct the correlative datasets in three-dimensions. The acquisition and reconstruction procedures for integrated array tomography comprise the basis of Chapter 3.

Future applications of CLEM will demand greater precision, further automation, and higher throughput, for which iCAT offers a number of potential advantages. Above all, iCAT enables large numbers of serial sections to be sequentially and automatically imaged to generate reconstructed volumes of overlaid FM and EM datasets with matching axial resolution. Moreover, specimen warping and shrinkage, which might otherwise occur in conventional array tomography methods, is prevented due to the absence of intermediate sample preparation. This ensures a precise overlay of biological molecules and structural context at high resolution in all three dimensions. Additionally, precisely overlaid fluorescence data has the potential to vastly improve classification of ultrastructural features in EM data. While modern machine-learning-based segmentation methods (e.g. ilastik [30], SuRVoS [31]) are quite sophisticated, they nevertheless require some degree of manual annotation. Because high-accuracy overlaid correlative datasets contain, in a sense, the classification data that these methods seek to provide, such datasets could reduce the need for supervised learning while opening up new possibilities for machine learning applications such as artificial fluorescence predictions (Chapter 4).

# REFERENCES

- [1] RI Koning et al. “Integrated Light and Electron Microscopy”. *Correlative Imaging: Focusing on the Future* (2019), pp. 119–135.
- [2] Santiago Ramón et al. *Textura del sistema nervioso del hombre y de los vertebrados: estudios sobre el plan estructural y composición histológica de los centros nerviosos adicionados de consideraciones fisiológicas fundadas en los nuevos descubrimientos*. Vol. 1. Moya, 1899.
- [3] Stanley Finger. *Origins of neuroscience: a history of explorations into brain function*. Oxford University Press, USA, 2001.
- [4] Moritz Helmstaedter, Kevin L Briggman, and Winfried Denk. “3D structural imaging of the brain with photons and electrons”. *Current opinion in neurobiology* 18.6 (2008), pp. 633–641.
- [5] Narayanan Kasthuri et al. “Saturated reconstruction of a volume of neocortex”. *Cell* 162.3 (2015), pp. 648–661.
- [6] John G White et al. “The structure of the nervous system of the nematode *Caenorhabditis elegans*”. *Philos Trans R Soc Lond B Biol Sci* 314.1165 (1986), pp. 1–340.
- [7] Tomoko Ohyama et al. “A multilevel multimodal circuit enhances action selection in *Drosophila*”. *Nature* 520.7549 (2015), pp. 633–639.
- [8] Kerrianne Ryan, Zhiyuan Lu, and Ian A Meinertzhagen. “The CNS connectome of a tadpole larva of *Ciona intestinalis* (L.) highlights sidedness in the brain of a chordate sibling”. *Elife* 5 (2016), e16962.
- [9] David Grant Colburn Hildebrand et al. “Whole-brain serial-section electron microscopy in larval zebrafish”. *Nature* 545.7654 (2017), pp. 345–349.
- [10] Zhihao Zheng et al. “A complete electron microscopy volume of the brain of adult *Drosophila melanogaster*”. *Cell* 174.3 (2018), pp. 730–743.
- [11] Jeff W Lichtman and Joshua R Sanes. “Ome sweet ome: what can the genome tell us about the connectome?” *Current opinion in neurobiology* 18.3 (2008), pp. 346–353.
- [12] Davi D Bock et al. “Network anatomy and in vivo physiology of visual cortical neurons”. *Nature* 471.7337 (2011), pp. 177–182.
- [13] Jörgen Kornfeld and Winfried Denk. “Progress and remaining challenges in high-throughput volume electron microscopy”. *Current opinion in neurobiology* 50 (2018), pp. 261–267.
- [14] Christopher J Peddie and Lucy M Collinson. “Exploring the third dimension: volume electron microscopy comes of age”. *Micron* 61 (2014), pp. 9–19.

- [15] Kevin L Briggman and Davi D Bock. “Volume electron microscopy for neuronal circuit reconstruction”. *Current opinion in neurobiology* 22.1 (2012), pp. 154–161.
- [16] Martina Schifferer et al. “Niwaki Instead of Random Forests: Targeted Serial Sectioning Scanning Electron Microscopy With Reimaging Capabilities for Exploring Central Nervous System Cell Biology and Pathology”. *Frontiers in neuroanatomy* (2021), p. 79.
- [17] Kristen M Harris and John K Stevens. “Dendritic spines of CA 1 pyramidal cells in the rat hippocampus: serial electron microscopy with reference to their biophysical characteristics”. *Journal of Neuroscience* 9.8 (1989), pp. 2982–2997.
- [18] Ian A Meinertzhagen and SD O’neil. “Synaptic organization of columnar elements in the lamina of the wild type in *Drosophila melanogaster*”. *Journal of comparative neurology* 305.2 (1991), pp. 232–263.
- [19] Matthia A Karreman et al. “Fast and precise targeting of single tumor cells in vivo by multimodal correlative microscopy”. *Journal of Cell Science* 129.2 (2016), pp. 444–456.
- [20] Matthia A Karreman et al. “Intravital correlative microscopy: imaging life at the nanoscale”. *Trends in cell biology* 26.11 (2016), pp. 848–863.
- [21] Pascal De Boer, Jacob P Hoogenboom, and Ben NG Giepmans. “Correlated light and electron microscopy: ultrastructure lights up!” *Nature methods* 12.6 (2015), pp. 503–513.
- [22] Toshio Ando et al. “The 2018 correlative microscopy techniques roadmap”. *Journal of physics D: Applied physics* 51.44 (2018), p. 443001.
- [23] AC Zonnevylle et al. “Integration of a high-NA light microscope in a scanning electron microscope”. *Journal of microscopy* 252.1 (2013), pp. 58–70.
- [24] Frank Jan Timmermans and Cornelis Otto. “Contributed review: Review of integrated correlative light and electron microscopy”. *Review of scientific instruments* 86.1 (2015), p. 011501.
- [25] Kristina D Micheva and Stephen J Smith. “Array tomography: a new tool for imaging the molecular architecture and ultrastructure of neural circuits”. *Neuron* 55.1 (2007), pp. 25–36.
- [26] Irene Wacker and RR Schroeder. “Array tomography”. *Journal of microscopy* 252.2 (2013), pp. 93–99.
- [27] Jeroen Kuipers, Pascal de Boer, and Ben NG Giepmans. “Scanning EM of non-heavy metal stained biosamples: Large-field of view, high contrast and highly efficient immunolabeling”. *Experimental Cell Research* 337.2 (2015), pp. 202–207.
- [28] Christopher J Peddie et al. “Correlative super-resolution fluorescence and electron microscopy using conventional fluorescent proteins in vacuo”. *Journal of structural biology* 199.2 (2017), pp. 120–131.

- [29] Martijn T Haring et al. “Automated sub-5 nm image registration in integrated correlative fluorescence and electron microscopy using cathodoluminescence pointers”. *Scientific reports* 7.1 (2017), pp. 1–9.
- [30] Christoph Sommer et al. “Ilastik: Interactive learning and segmentation toolkit”. *2011 IEEE international symposium on biomedical imaging: From nano to macro*. IEEE. 2011, pp. 230–233.
- [31] Imanol Luengo et al. “SuRVoS: super-region volume segmentation workbench”. *Journal of Structural Biology* 198.1 (2017), pp. 43–53.

# 2

## OPTIMIZATION OF NEGATIVE STAGE BIAS POTENTIAL FOR FASTER IMAGING IN LARGE-SCALE ELECTRON MICROSCOPY

Large-scale electron microscopy (EM) allows analysis of both tissues and macromolecules in a semi-automated manner, but acquisition rate forms a bottleneck. We reasoned that a negative bias potential may be used to enhance signal collection, allowing shorter dwell times and thus increasing imaging speed. Negative bias potential has previously been used to tune penetration depth in block-face imaging. However, optimization of negative bias potential for application in thin section imaging will be needed prior to routine use and application in large-scale EM. Here, we present negative bias potential optimized through a combination of simulations and empirical measurements. We find that the use of a negative bias potential generally results in improvement of image quality and signal-to-noise ratio (SNR). The extent of these improvements depends on the presence and strength of a magnetic immersion field. Maintaining other imaging conditions and aiming for the same image quality and SNR, the use of a negative stage bias can allow for a 20-fold decrease in dwell time, thus reducing the time for a week long acquisition to less than 8 hr. We further show that negative bias potential can be applied in an integrated correlative light electron microscopy (CLEM) application, allowing fast acquisition of a high precision overlaid LM-EM dataset. Application of negative stage bias potential will thus help to solve the current bottleneck of image acquisition of large fields of view at high resolution in large-scale microscopy.

---

This chapter has been published as: Ryan Lane et al. “Optimization of negative stage bias potential for faster imaging in large-scale electron microscopy”. *Journal of structural biology: X* 5 (2021), p. 100046.

## 2.1. Introduction

Mapping the full ultrastructural layout of complex biological systems at nanometer-scale resolution is a major challenge in cell biology. Electron microscopy (EM) is uniquely capable of stretching the vast spatial scales necessary to identify macromolecular complexes, subcellular structures, and intercellular architecture. As a consequence, interest in large-scale EM, where many high-resolution tiles are stitched into a gigapixel image frame, has exploded in recent years. Large-scale EM, however, suffers from the long acquisition times necessary to acquire sufficient signal at high resolution [2].

A variety of approaches have been undertaken to advance throughput. While throughput is already a bottleneck for large-scale 2D imaging [3], most of these approaches have been developed under the framework of 3D imaging. Throughput is particularly relevant to the field of connectomics in which it typically takes months to acquire the image data necessary for neuronal reconstruction [4]. To image the brain of a larval zebrafish, for example, Hildebrand et al. [5] conducted multiple imaging rounds at successively higher magnification. Regions of interest (ROI) were selected between imaging rounds for successive, targeted acquisitions down to 4 nm/px resolution, thereby reducing the time it would otherwise take to fully image the full brain at high resolution. Similarly, Delpiano et al. [6] used detection of in-resin preserved fluorescence in an integrated light and electron microscope for automated guiding to ROIs for subsequent acquisition. Other approaches involve parallelizing the imaging load across multiple instruments. This has been employed in focused ion beam scanning electron microscopy (FIB-SEM) for the reconstruction of thick slices of *Drosophila* brain tissue at isotropic ( $8 \text{ nm} \times 8 \text{ nm} \times 8 \text{ nm}$ ) voxel resolution [7] as well as in serial section transmission electron microscopy (ssTEM) for the yearlong acquisition of a cubic millimetre of mouse brain tissue [8]. Dedicated instrumentation for faster imaging of serial thin sections has also been developed in recent years. In some instances conventional microscopes have been equipped with specialized detection optics to allow for larger fields of view [9, 10]. Multi-beam instruments in which a sample is simultaneously imaged by multiple focused electron beams have also been developed [11, 12].

Faster imaging could also be achieved by increasing signal collection in established thin sections approaches, which would allow for reduced acquisition time while maintaining a sufficient signal-to-noise ratio (SNR). It has previously been shown that the use of a retarding field increases SNR in SEM [13, 14], but for biological imaging the use of a retarding field has thus far been investigated in detail only for serial blockface scanning EM (SBF-SEM) [15, 16, 17]. Additionally, a high negative bias potential is employed in the Zeiss multibeam to allow for secondary electron (SE) detection from individual beamlets [11]. Conversely, the use of a positive stage bias has been examined for the suppression of secondary electrons [18]. The full benefits of stage bias remain underutilized because optimization criteria and signal detection in a magnetic immersion field, in particular, have yet to be addressed.

In the cases in which a negative bias potential has been used, a voltage is ap-

plied to the stage while the pole piece of the electron microscope is kept at ground such that an electric field is generated between the specimen and detector planes. While the primary electron beam experiences a deceleration, the signal electrons experience an acceleration from the specimen towards the dedicated detector. The ensuing acceleration results in an increase to the collected signal [19] and—if the detector geometry, landing energy, and potential bias are tuned properly—can be used to filter out secondary electrons [17]. The same signal can then be obtained with a shorter acquisition time.

Identification of biological structures and molecules in large-scale EM is typically complemented with approaches to label and visualize specific biomolecules or organelles. Aside from immuno-EM and genetically-encoded enzymatic tags that can deposit osmophilic polymers, CLEM is perfectly suited to identify entities across spatial scales (reviewed in De Boer et al. [20]). However, if one wants to avoid intermediate processing of the sample, the sample preparation protocol must be adjusted to limit concentrations of heavy metal staining to prevent quenching of fluorophores [3]. The reduced amount of staining material then needs to be countered by increased dwell time, further necessitating optimization of EM signal collection. Here we present faster imaging of tissue sections that have been prepared following conventional array tomography protocols through the use of a negative bias potential. No post-staining was applied as the tissue was immunostained for fluorescence post-sectioning.

## 2.2. Results

### 2.2.1. Negative bias potential enhances signal in routine EM samples

We first illustrate how the use of a potential bias can improve signal collection in a typical SEM experiment. A potential bias of  $-1\text{ kV}$  is applied to the stage of an SEM with an integrated fluorescence microscope (Figure 2.1A & B). The bias is applied via an external power supply connected to a custom stage plate such that the sample is electrically isolated from the rest of the fluorescence microscope and electrical components of the stage [21]. By generating an electric field between the sample and the BSE detector, the bias potential accelerates signal electrons inwards away from their otherwise linear trajectories. Because of their lower energy, secondary electrons ( $< 50\text{ eV}$ ) are redirected inside the inner annulus of the BSE detector, while higher energy backscattered electrons ( $> 50\text{ eV}$ ) are redirected over a wider area depending on their initial emission angle and energy.

Pancreas tissue was prepared for integrated fluorescence-electron microscopy as described in Section 2.4.2. No post-staining was applied resulting in lower contrast relative to other EM sample preparation protocols [3]. EM images of EPON-embedded,  $80\text{ nm}$  tissue were acquired in immersion mode with and without a  $-1\text{ kV}$  bias potential (Figure 2.1A & B). When subject to a bias potential, EM images demonstrate noticeably higher contrast and less noise (Figure 2.1C & G). The primary beam energy was increased by  $1\text{ kV}$  such that the landing energy was held constant at  $1.5\text{ keV}$  in accordance with the section thickness. Data acquired with increased primary energy but without the use of stage bias (Figure 2.1D) reveals

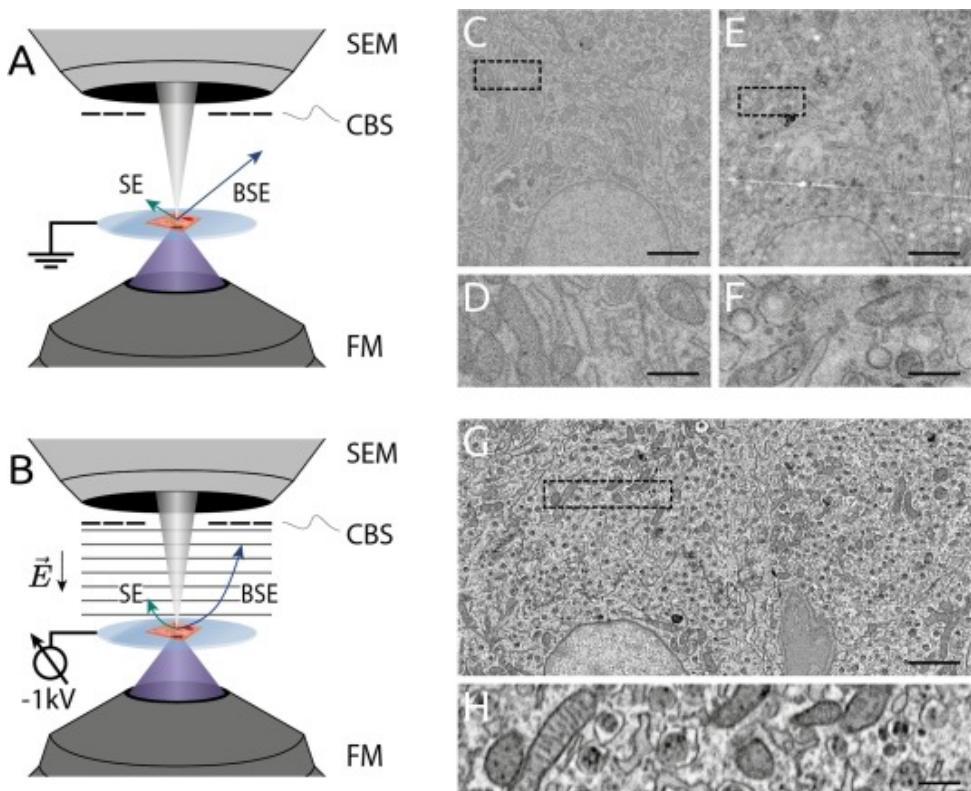


**Figure 2.1.** Negative bias potential significantly enhances EM contrast in tissue. Schematic of integrated microscope without (A) and with (B) an applied stage bias. Electric field induced by the bias potential accelerates electrons emitted from the sample to the CBS detector. EM images of rat pancreas tissue without (C – F) and with (G & inset H) the use of stage bias. Biased images (G & inset H) were acquired at 2.5 keV primary energy with a -1 kV bias potential—hence, a 1.5 keV landing energy. For the sake of comparison, unbiased images (C & inset D) were acquired with the same landing energy, while unbiased images (E & inset F) were acquired with the same primary energy. The per-pixel dwell is held constant across all images at 5  $\mu$ s. Vast improvement in EM signal and contrast can be seen by comparing insets (D & F) with (H). Scale bars: 2  $\mu$ m (C, E, & G); 0.5  $\mu$ m (D, F, & H). Raw data at full resolution is available at [Nanotomy](#).

that the increase in apparent signal does not arrive solely from an increased primary energy. Moreover, the importance of maintaining a sufficiently low landing energy becomes clear by the visible artefacts from the ITO-coated glass substrate that appear with higher energies. The 0.4 nA beam current and 5  $\mu$ s/px dwell time are held constant in each acquisition. The gain of the BSE detector had to be decreased while applying the negative bias to prevent the detector from saturating.

### 2.2.2. Simulating signal electron trajectories with and without negative potential bias

Electron trajectories were simulated to better ascertain how a negative bias potential may give rise to better signal detection. Secondary electron and backscattered electron (BSE) trajectories were simulated for a variety of EM imaging conditions (Figure 2.2). A model of the optical layout within the integrated microscope was developed in Electron Optical Design (EOD) [22] incorporating the geometry of the Verios 460 SEM objective lens and concentric backscatter (CBS) detector. The negative potential bias is factored into the model by implementing the sample plane as an additional lens element, which can then be biased to an arbitrary voltage. To mirror the 5 mm working distance of our microscope, the end of the pole piece (grey element in Figure 2.2) and start of the sample plane (red) are situated at  $z = 0$  mm and  $z = 5$  mm respectively. The roughly 0.5 mm thick CBS detector (blue) is then located immediately below the pole piece.

Simulations were done for both non-immersion (high resolution or HR) and immersion (ultra-high resolution or UHR) SEM operation modes. For the case of non-immersion mode (Figure 2.2A & B), the magnetic focusing field is contained within the objective lens and therefore does not play a role in the signal electron trajectories. In these instances, the trajectories of the SEs and BSEs are dictated entirely by their initial velocity and the electric field due to the bias potential. In UHR-mode (Figure 2.2C & D), however, the sample is immersed in a strong magnetic field that both focuses the primary beam and—together with the electric field—alters the paths taken by the signal electrons. For this reason, the magnetic field strength is calculated by the field strength required to focus a parallel beam propagating in the  $+z$  direction at the sample plane.

For each scenario shown, a bundle of secondary ( $E_0 = 5$  eV) and backscattered electrons ( $E_0 = 1$  keV) is emitted from the origin at  $z = 5$  mm. The angular distribution is given by Lambert's cosine distribution [23]. A screen is placed at the detector plane to record the radial position of the signal electrons, from which the scatter plots are generated (Figure 2.2). The grey rings of varying diameter represent the individual segments of the CBS detector. For the case of non-immersion mode and no potential bias (Figure 2.2A), the region between the detector and sample planes is field-free and the signal electrons travel freely in straight paths coinciding with one another. Only when a bias potential is added (Figure 2.2B) do the higher energy BSEs diverge from the secondaries, which, due to their low initial energy, are accelerated inside the BSE detector before they are able to spread out radially. The trajectories change when under the influence of a magnetic immersion field (Figure 2.2C) in which case the Lorentz force causes the signal electrons to spiral about the optical axis [24]. The low energy SEs remain tightly coiled as they propagate up through the BSE detector while the higher energy BSEs stretch out over greater radial distances. Whether the BSEs collide into the detector depends largely on the emission angle. The addition of a 1 kV bias potential (Figure 2.2D) enables BSEs with a wider distribution of emission angles to reach the detector, resulting in the collection of more signal. These results suggest no secondary electron is ever registered as a count by the BSE detector—either because it is accelerated inside the

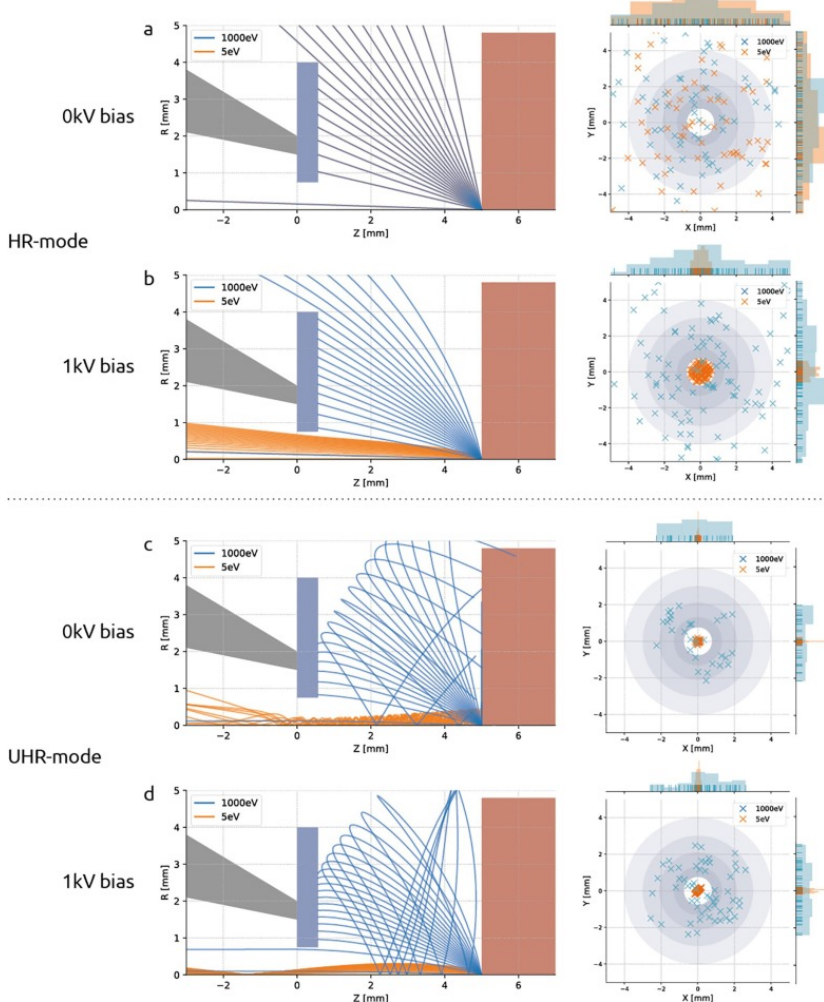


**Figure 2.2.** Signal electron trajectories demonstrate the efficacy of stage bias in redirecting BSEs to the detector while simultaneously filtering out secondary electrons. Trajectory plots for SE and BSE bundles launched from the sample plane (left) and scatter plots (right) show the spatial distribution of signal electrons at the detector plane. In HR-mode, SEs and BSEs travel in overlapping, linear paths without the presence of an electric field (A), but BSEs get accelerated towards the detector when a negative bias potential is introduced (B). Signal electrons take on spiral trajectories in the presence of an immersion magnetic field (C), but are again steered to the detector when an electric field is added (D). In each set of simulations, BSEs (blue) and SEs (orange) are launched from the sample plane at  $z = 5$  mm. Trajectory plots show geometry of the pole piece (grey), CBS detector (blue), and stage plate (red). Scatter plots show  $x, y$  coordinates of signal electrons at the detector plane ( $z = 5$  mm). Spatial distributions of signal electrons are plotted on the margins of the scatter plots.

detector or (in the field-free case) because it is of too little energy to generate an electron-hole pair [19].

The collection efficiency of BSEs increases monotonically with increasing negative bias potential for both imaging modes (Figure S1). These results agree with what is suggested by the trajectory plots of Figure 2.2—that the electric field generated by the stage bias tapers the radial spread of the BSEs leading to a greater percentage of BSEs collected. Note that the percentage of BSEs detected is greater for HR-mode across the range of bias potentials simulated. It therefore seems advantageous to prefer non-immersion mode, however, greater collection efficiency is only one factor to consider. The magnetic immersion field results in lower aberrations, meaning that for high resolution imaging, UHR mode is still often favourable. While the geometry modelled here is specific to our particular electron microscope, simulations were extended over a range of working distances and were found to follow the same general trends.

### 2.2.3. Experimental optimization of negative potential bias leads to increased throughput

EM imaging was expanded to encompass a wider imaging parameter space across a sequence of dwell times and negative bias potentials for both immersion and non-immersion mode based on the simulations (Figure 2.3). The primary beam energy was increased together with the bias potential to hold the landing energy constant at 1.5 keV. Likewise, the gain of the CBS detector was adjusted with each bias potential to keep the intensity levels from clipping. The detector gain and offset were manually calibrated to acquire over the full 16-bit range of the detector. This was not always possible, however, as many of the images acquired with low or no bias potential took up only a fraction of the detector's bandwidth, even at maximum gain.

An increase in image signal with increasing negative bias potential for both imaging modes up to roughly  $-1500$  V was recorded (Figure 2.3), after which it becomes difficult to perceive notable differences in image quality. The signal appears to improve more gradually in non-immersion mode, whereas the improvement for immersion mode is more abrupt. Furthermore, in certain instances, increasing the integration time by several factors results in a less substantial increase to the apparent SNR than a 500 V increase to the negative bias potential. This is significant as the integration time is typically the primary imaging parameter to improve image quality—and large increases come at the direct expense of throughput.

Quantitative SNR measurements, based on the spectral signal-to-noise ratio (SSNR) [25], were made on the collection of images and averaged for each combination of bias potential, dwell, and imaging mode (Figure 2.4). These measurements were corroborated using a separate cross-correlation-based SNR method [26] (Figure S2). In particular, these measurements reveal that an image acquired in non-immersion mode with a  $1\text{ }\mu\text{s}$  dwell time and  $-1.5\text{ kV}$  bias potential yields roughly the same SNR as an image acquired with a  $5\text{ }\mu\text{s}$  dwell but with no applied bias. The effect of the potential bias is even more pronounced in immersion mode where the SNR of a  $1\text{ }\mu\text{s}$  image with a  $1.5\text{ kV}$  stage bias exceeds that of a  $20\text{ }\mu\text{s}$  image acquired without a bias.

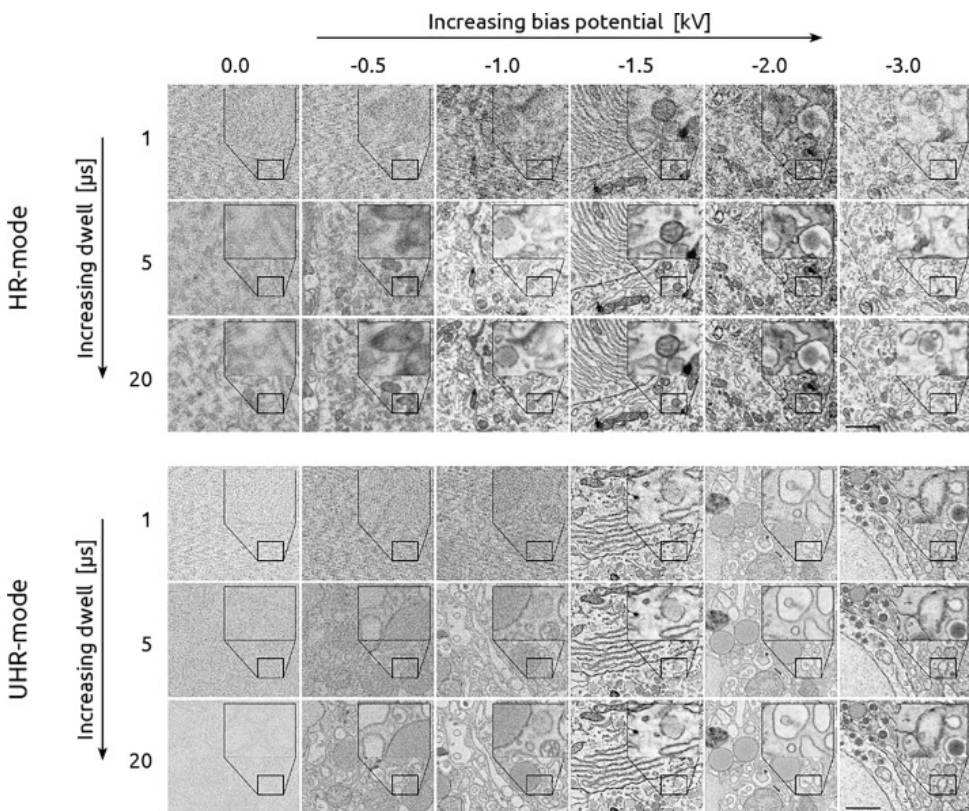


**Figure 2.3.** Negative bias potential delivers 5–20 times faster imaging while maintaining image quality. Bias potential varies from 0 to  $-3\text{ kV}$  (left to right) while the integration time varies from 1 to  $20\text{ }\mu\text{s}$  (top to bottom) for both the non-immersion (top) and immersion mode (bottom) image matrices. All images acquired with  $1.5\text{ keV}$  landing energy to match penetration depth. Scale bars:  $1\text{ }\mu\text{m}$ . Raw data is available at [Nanotomy](#).

Fourier analysis was done to analyse the effect of the bias potential in different frequency domains (Figure 2.5). The center spot of the 2D FFTs—containing most of the signal—becomes more prominent with increasing bias potential. This growth is reflected in the SSNR spectra, which show order of magnitude increases in amplitude in the low spatial frequency domain. Furthermore, the high frequency streak artefacts present in the lower bias potential images—visible in the 2D FFTs—become suppressed at higher bias potentials.

## 2.2.4. Potential bias allows for higher throughput EM and CLEM acquisitions

Only small regions of interest are typically recorded at high resolution EM given that full section imaging at sub-10 nm resolution often takes an excessive amount

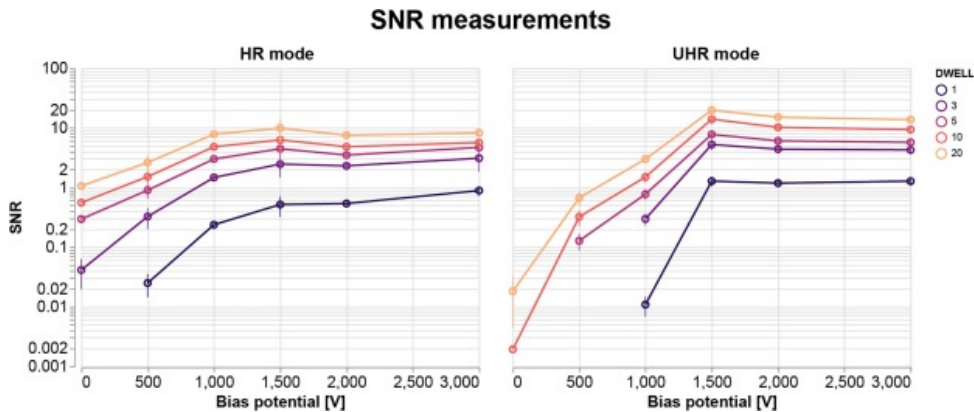


**Figure 2.4.** Optimization of bias potential delivers SNR increases of multiple orders of magnitude. At bias potentials greater than 1.5 kV, the SNR is found to level off for both imaging modes. Images are comprised of varying stage bias potentials, integration times, and imaging modes but with fixed 1.5 keV landing energy and 5 mm working distance. Different color lines represent different dwell times as indicated by the legend. SNR measurements are averaged over five EM images at different areas of the tissue for each combination of bias potential, dwell time, and imaging mode. Error bars indicate the standard deviation in the SNR over the five images. Missing data points indicate a negative SNR, which may occur for images with extremely high noise.

of time. As a result of the enhanced signal-to-noise ratio afforded to us by the use of a negative bias potential, we are able to significantly expedite the imaging of a thin section of HeLa cells at 5 nm resolution (Figure 2.6). Based on our empirical results (Figure 2.4), a negative potential bias of  $-1.5\text{ kV}$  was chosen for EM imaging in immersion mode. A per-pixel dwell time of  $2\text{ }\mu\text{s}$  was chosen to balance high SNR and image clarity with overall imaging time. Control images of the same cell were acquired without the use of a bias potential at the same landing energy (Figure 2.6A) and primary energy (Figure 2.6B). The total imaging time for this  $550\text{ }\mu\text{m} \times 350\text{ }\mu\text{m}$  area was 5.6 hr.

To demonstrate the application of a negative bias potential on samples also prepared for immunofluorescence, a large-scale acquisition was conducted on a section of rat pancreas tissue (Figure 2.7). Full section ( $0.5\text{ mm}^2$ ) acquisition including fluorescence imaging, stage translations, and additional overhead factors was completed in 8 hr. Table 2.1 provides an overview of the time spent on each aspect of the workflow, and exemplifies the potential time savings afforded by using a bias potential. We note that no post-staining was applied to this section in order to allow integrated acquisition of fluorescence for high-precision overlaid FM. Fluorescence images were acquired prior to EM to prevent quenching of the fluorescence due to electron beam irradiation. The insulin-producing beta cells—clustered within the islet of Langerhans—were immunolabelled and given a Hoechst counterstain to target cell nuclei as well as the rough endoplasmic reticulum in the exocrine region of the tissue (blue) (Figure 2.7A). The section edges

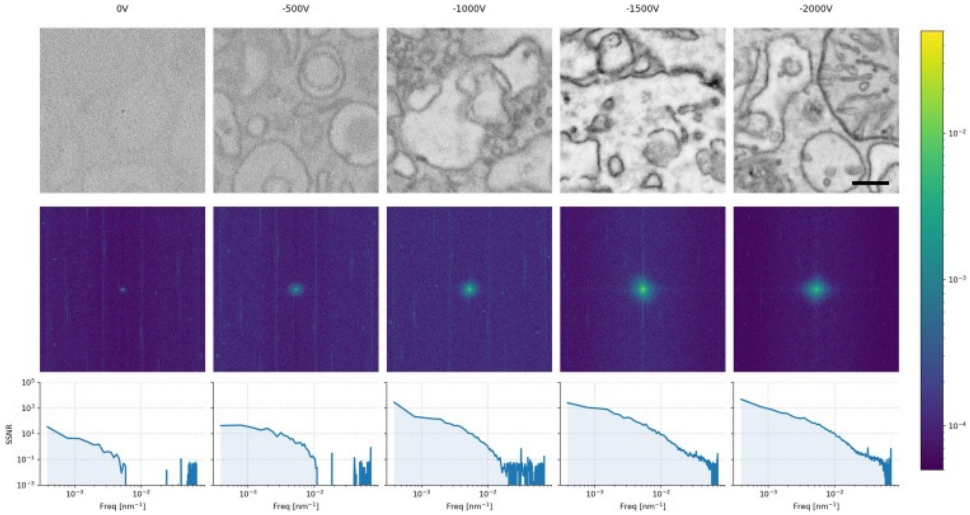


**Figure 2.5.** Noise contributions suspected to originate from the scanning electronics are suppressed with increasing bias potential. Top: sequence of 5  $\mu\text{s}$  dwell tissue images acquired in immersion mode with varying amounts of stage bias. Center: 2D FFTs of tissue images showing the central spot, which represents most of the signal, becoming more prominent with increasing bias potential up to  $-1.5 \text{ kV}$ . The 2D FFTs exhibit noticeable streak artefacts at higher frequencies, particularly in the lower bias potential images. We attribute these streaks to electric interference from the scanning electronics. Furthermore, there is a constant offset, which is likely a combination of shot noise from various sources, and may also include a component from the scanning electronics. Bottom: SSNR spectra show a division between the low frequency (primarily signal) and high frequency (primarily noise) portions of the tissue images. As the suspected scanning electronics noise is drowned out, the SNR improves dramatically. Scale bar: 500 nm.

can easily be discerned from the FM images, facilitating the area selection for subsequent EM imaging (Figure 2.7B). Here the islet (light grey region) can be seen surrounded by the exocrine tissue (dark grey). An automated registration procedure [27] was done to overlay the fluorescence signal onto the EM images (Figure 2.7C) such that the fluorescence signal is correlated at high resolution across the entire EM field of view (Figure 2.7D & E). Additional details of how the correlative acquisition and reconstruction were done are provided in Sections 2.4.4 and 2.4.5 respectively.

## 2.3. Discussion

We have shown that the SNR of a  $1 \mu\text{s}/\text{px}$  image subject to a bias potential outperforms that of a  $5 \mu\text{s}/\text{px}$  unbiased image or  $20 \mu\text{s}/\text{px}$  in the case of immersion mode. This has important ramifications for large-scale and volume EM studies in which throughput is a primary concern. Due to practical limitations on time, it is often the case that large-scale EM studies are conducted on a single specimen. Negative

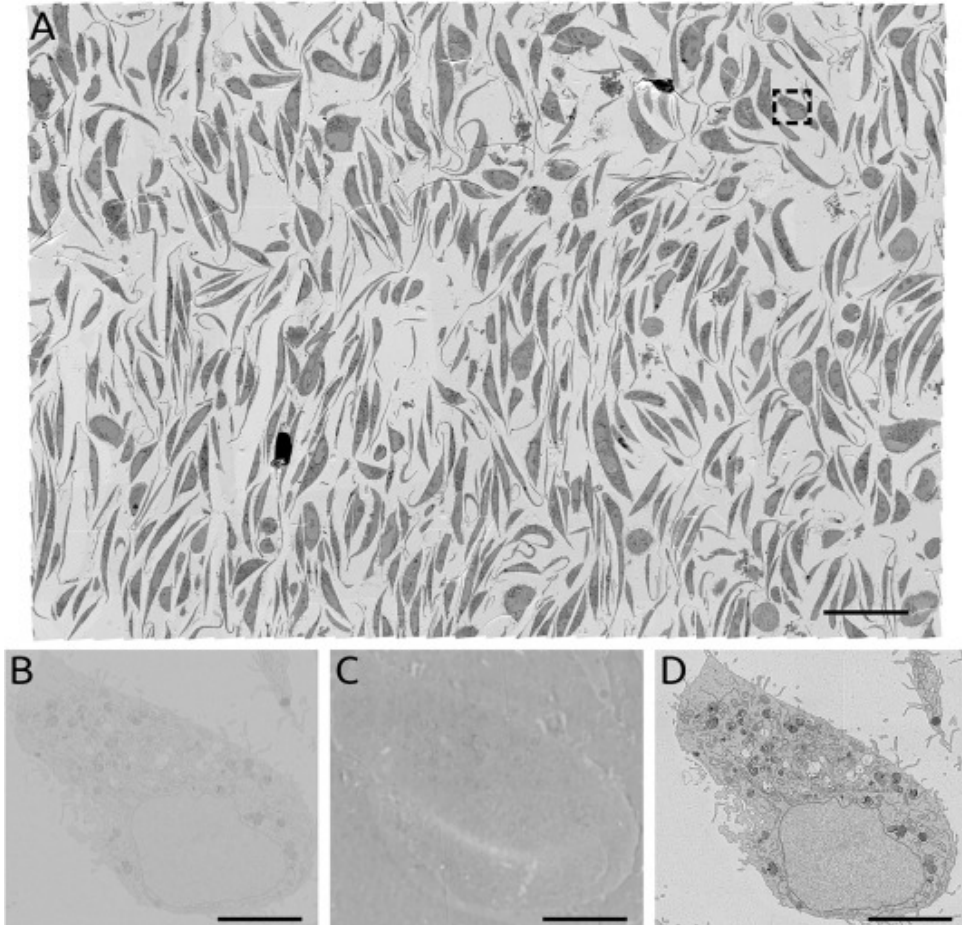


**Figure 2.6.** Fast, high resolution EM gigapixel image of cultured cells. (A) EM acquisition of a 100 nm section of HeLa cells as a nanotomy map. Section imaged at 1.5 keV LE and with a  $-1.5\text{ kV}$  bias potential. For the sake of comparison, one HeLa cell was acquired at multiple energy settings: (B) 1.5 keV LE with no bias potential; (C) 3 keV LE with no bias potential; (D) 1.5 keV LE with  $-1.5\text{ kV}$  bias potential—identical to that of the large-scale acquisition. Scale bars: 50  $\mu\text{m}$  (A); 5  $\mu\text{m}$  (B, C, & D). Raw data is available for viewing via [Nanotomy](#).

potential bias facilitates comparison studies by allowing for multiple specimens to be acquired in the same timeframe that would otherwise be necessary for a single specimen. Experiments on specimens prone to electron beam irradiation damage are likewise facilitated as the same SNR can be achieved with a considerably smaller electron dose. Furthermore, a negative bias potential has recently been utilized to deliver enhanced EM contrast to tissue sections in which the fluorescence is preserved [21]. Due to the minimal amounts of heavy metal staining [29], such samples have thus far been challenging to image—in certain instances requir-

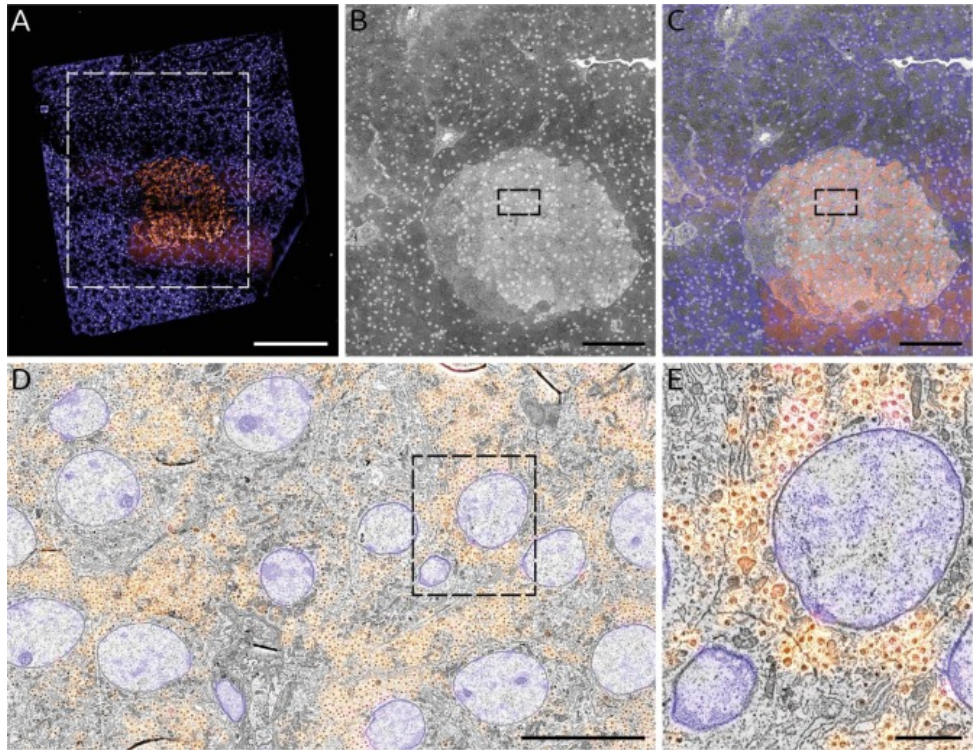


**Figure 2.7.** Fast, correlative imaging of a complete EM section at high resolution. 80 nm rat pancreas tissue was imaged at 3 keV beam energy with a  $-1.5$  kV stage bias (1.5 keV landing energy) with  $2\ \mu\text{s}$  dwell as a nanotomy map. (A) Composite two-channel FM image of the tissue section: cell nuclei (blue) stained by Hoechst; insulin-producing beta cells (orange) immunolabeled with Alexa 594. (B) Composite EM image of the area outlined in (A) comprising the islet of Langerhans identified via FM imaging. (C) Correlative overlay of the islet and surrounding exocrine tissue. (D) Zoomed-in area of islet outlined in (B & C) with inset (E) exhibiting the native resolution (5 nm pixel size) that exists across the entirety of the nanotomy map. Total imaging time is 8 hr, the majority of which is taken up by the high-resolution EM imaging. Note that a similar area at this pixel size (see e.g. Ravelli et al. [28]) typically takes upwards of 24 hr with TEM. Scale bars: 200  $\mu\text{m}$  (A); 100  $\mu\text{m}$  (B & C); 10  $\mu\text{m}$  (D); 2  $\mu\text{m}$  (E). Raw data is available via [Nanotomy](#).

ing dwell times of up to 60  $\mu\text{s}/\text{px}$  [30].

Our simulations show that BSE collection is enhanced by an effective increase of the detector numerical aperture—by applying the bias potential we increase the range of angular distributions of the BSEs able to be collected. However, this does not fully explain the extent of the increase in SNR observed experimentally. In particular, the simulations predict roughly a factor two increase in signal collection as the bias voltage is raised to our maximum of 3 kV, while our empirical measurements show SNR improvements of one to two orders of magnitude. This disparity

**Table 2.1.** Use of optimized potential bias leads to an 80% reduction in total imaging time for a typical large-scale acquisition. The total imaging time is highly dependent on the ROI size, which may vary widely depending on the biological application. Here the typical diameter of an islet of Langerhans is given, while in Figure 2.7 a  $700\text{ }\mu\text{m} \times 700\text{ }\mu\text{m}$  area was chosen as the ROI—resulting in the 8 hr total acquisition time. Total imaging times for arbitrary ROI sizes can be determined by first calculating the number of image tiles needed:  $N = \text{ceil}((L - ow) - (w - ow))^2$  where  $L$  is the typical section or ROI width,  $o$  is the percentage overlap between image tiles, and  $w$  is the field of view. Note that the negative overlap given for the low-magnification CLEM tiles reflects that these tiles do not overlap with one another.

		Low-mag CLEM		Hi-mag EM	
		No bias	Bias	No bias	Bias
EM	Pixel size	36.6 nm		4.88 nm	
	Dwell	10 $\mu\text{s}$	2 $\mu\text{s}$	10 $\mu\text{s}$	2 $\mu\text{s}$
	Field of View	150 $\mu\text{m}$		20 $\mu\text{m}$	
	Overlap (b/w images)	-36 $\mu\text{m}$ (-24%)		2.4 $\mu\text{m}$ (12%)	
	N. pixels	16.8 Mpx		16.8 Mpx	
	Acquisition time	168 s	33.6 s	168 s	33.6 s
FM	Exposure time	5 s			
	N. channels	2			
	Acquisition time	10 s			
Overhead	Registration procedure	20 s			
	Stage translation	4 s		2 s	
Total	Total acquisition time (per CLEM/EM image)	202 s	68 s	170 s	36 s
Large-scale acquisition	Typical size	700 $\mu\text{m}$		250 $\mu\text{m}$	
	N. image tiles	16		225	
	Total acquisition time	54 min	18 min	11 hr	133 min

can be explained in part by the electron gain factor of the detector. Šakić et al. [19] shows that the signal generated in the detector by the incident electrons increases linearly with energy between 200–10 000 eV. Thus, in addition to increasing the amount of collected BSEs, the bias potential also leads to signal enhancement via BSE acceleration. At low bias voltages the images appear to be dominated by one particular source of noise—which we suspect derives from the scanning electronics. Increasing the bias potential in this regime leads to an exponential rise in the SNR as this noise source is drowned out (Figure 2.4; Figure 2.5). At sufficiently high bias voltages, the image noise is instead dominated by shot noise, constraining the exponential rise in SNR beyond 1.5 kV. The practical limit to the amount of bias potential we are able to apply is limited by the dielectric breakdown in vacuum. We estimate for our particular setup that the breakdown voltage occurs above 3 kV—well beyond the point at which the SNR plateaus.

Other volume EM methods such as SBF-SEM or FIB-SEM also stand to gain from the use of a negative potential bias. The gains in imaging speeds have the potential to shift the bottlenecks in these approaches to overhead factors such as time spent slicing or milling [4]. If unaccounted for, the non-planar geometries in these

techniques may induce more pronounced charging artefacts. Bouwer et al. [17] show that charging artefacts can be mitigated by successfully filtering out SEs. We have found that SE filtering is accomplished at moderate potential biases, though in Bouwer et al. [17] the innermost rings of the BSE detector had to be selectively turned off to achieve the same effect. Negative bias potential could similarly be combined with the multi-scale approach taken by Hildebrand et al. [5]. The combination with an integrated microscope as demonstrated here could then offer a further benefit by in-situ selection of the regions of interest for high magnification acquisition. We envision a strategy in which regions of interest are first identified via fluorescence microscopy, then automatically navigated to and imaged with high resolution EM [31]. Higher throughput could then be realized through a combination of faster acquisition via the negative bias potential, the removal of additional rounds of imaging, and the elimination of overhead from the entire imaging pipeline.

Further throughput enhancement could be obtained in several ways. One option would be to increase the beam current, thus increasing the per-pixel electron dose. Higher currents, however, require larger aperture sizes which result in greater chromatic and spherical aberration. This can be problematic for many biological applications in which keeping aberrations at a minimum is critical for reaching a desired resolution, e.g. resolving neuronal connections, nuclear pores, or cell-cell junctions. Hence, it only makes to image with the maximum current acceptable for one's application. At the same time, the use of a negative bias potential has previously been shown to result in improved resolution due to reduced space charge and aberrations [13, 32]. Thus, the use of a negative bias potential may allow for a marginally higher beam current to further increase throughput. Alternatively, the signal may be strengthened by increasing the landing energy. This may also be disadvantageous—as evidenced in Figure 2.1 and Figure 2.6—since too great a landing energy will result in partial transmission of electrons through the tissue section. In addition to reducing the number of generated BSEs in the tissue, this will increase the noise level by detection of accelerated BSEs generated in the underlying substrate. Finally, more signal could be generated by increasing the amount of staining material in the sample. This is a common approach for certain applications within large-scale EM such as neuronal connectomics, where an almost binary level of contrast may still be acceptable [3]. Our stage bias approach holds promise to decrease acquisition times also in these applications, provided the lower limit imposed on dwell time by the detector response time is not reached.

## 2.4. Material & methods

### 2.4.1. Modeling

All simulations were performed in Electron Optical Design (EOD) [22]. Descriptions of how the simulations were carried out are provided in the main text. The angular distribution of signal electrons generated by a beam of primary electrons at a normal incident angle can be approximated by Lambert's cosine law [23]. The

probability of sampling a ray with angle  $\theta$  to the normal of the surface is then proportional to  $\cos \theta \sin \theta = \sin 2\theta$ . If  $U$  is a random uniform distribution between 0 and 1, then

$$\int_0^\theta \sin(2\theta) d\theta = U \quad (2.1)$$

$$\theta = \cos^{-1}(\sqrt{U}) \quad (2.2)$$

from which the initial angle of a signal electron can be chosen at random for use in simulations.

### 2.4.2. Tissue and sample preparation

Fixed rat pancreas tissue were post fixed for 2 hr in 1% osmiumtetroxide and 1.5% potassium ferrocyanide in 0.1 M cacodylate for 2 hr at 4 °C. Followed by dehydration in a graded series of ethanol and finally embedded in EPON. Ultrathin section of 80 nm were cut and placed on ITO glass. Sections were blocked for 30 min with 1% bovine serum albumin (BSA; Sanquin, The Netherlands) in tris-buffered saline (TBS), pH 7.4. Next, anti-insulin (guinea pig; 1:50 in 1% BSA/TBS) was incubated for 2 hr, followed by three washes of 5 min with TBS and subsequent incubation for 1 hr with biotinylated secondary antibody (donkey-anti-guinea pig; 1:400 in 1% BSA/TBS, Jackson Immunoresearch, UK) followed by three washes in TBS. Finally, streptavidin conjugated Alexa594 (1:200, in 1% BSA/TBS, Life Technologies) was added for 1 hr followed by three washes in TBS and two with MilliQ water. Hoechst staining was performed for 10 min followed by a washing step with MilliQ water.

HeLa cells were cultured in a 37 °C, 5% CO<sub>2</sub> incubator, in T75 culture bottles (Corning). Cells were maintained in Dulbecco's Modified Eagle's Medium (DMEM; Gibco) supplemented with 10% fetal bovine serum, 2 mM L-glutamin, 100 U/mL penicillin, 100 mg/mL streptomycin (referred to as complete DMEM). Cells were passaged when confluence reached 85% to 90% were grown in 6 cm dishes. Cells were incubated for 3 hr with endocytic fiducial markers at a concentration of 1 mg/mL dissolved in complete DMEM, rinsed, and then fixed with 2.5% glutaraldehyde + 2% formaldehyde in 0.1 M Phosphate buffer. Fixed HeLa cells were scraped, embedded in agarose and prepared for electron microscopy according to the protocol described in [33] with minor modifications. Briefly, samples were postfixated using 1% osmium tetroxide (w/v) with 1.5% potassium ferrocyanide (w/v) for 1 hr on ice, and stained with 2% uranyl acetate in dH<sub>2</sub>O for 30 min. Dehydration was performed using a graded ethanol series. Samples were embedded in EPON resin and polymerized for 48–60 hr at 65 °C. Ultrathin sections of 100 nm were cut using a microtome (Leica, U67) and placed on ITO glass. Hoechst staining was performed for 120 min followed by a washing step with MilliQ water, and air dried.

### 2.4.3. Signal-to-noise measurements

The SNR is calculated by averaging the spectral signal-to-noise ratio (SSNR) [25] over the full frequency space of the set of input images. Here, the input images are composed of alternating scan lines from individual images acquired with a pixel

size on par with the resolution of the electron beam. The SSNR is given by

$$R_n = \frac{\text{cov}(I_i, I_{i+1})}{\text{var}(I_i) \text{var}(I_{i+1})} \quad (2.3)$$

where  $F_k(r)$  is the Fourier transform of the  $k^{\text{th}}$  image, there are  $K$  images in total,  $\bar{F} = \frac{1}{K} \sum_k F_k(r)$  is the mean of the Fourier transformed images, and  $R$  is the region of interest. A single SNR value for the entire image (Figure 2.4; Figure S2) is obtained when  $R$  is the full image; when spectrally resolved (bottom row of Figure 2.5),  $R$  is a ring in Fourier space.

Additional SNR measurements based on a cross-correlation approach presented in Joy [26] were made to verify the SSNR-based calculations. In this approach, the SNR is calculated from computing the cross-correlation coefficient,  $R_n$ , between successive scan lines,  $I_i$  and  $I_{i+1}$ , of individual EM images. The cross-correlation coefficient is given by

$$R_n = \frac{\text{cov}(I_i, I_{i+1})}{\text{var}(I_i) \text{var}(I_{i+1})} \quad (2.4)$$

The signal-to-noise ratio is then calculated from

$$\text{SNR} = \frac{R_n}{1 - R_n} \quad (2.5)$$

#### 2.4.4. Integrated microscopy workflow

Fluorescence microscopy was done in the integrated microscope via the SECOM (Delmic B.V.), which has been retrofitted into the vacuum chamber of a Verios 460 SEM (Thermo Fisher Scientific) such that the two microscopes share a common sample stage and optical axis [34, 35]. With this configuration we are able to achieve high overlay precision without a reliance on fiducial markers or manual input [27]. The SECOM was equipped with a CFI S Plan Fluor ELWD 60XC microscope objective (Nikon), which was chosen for its high magnification in combination with an extra-long working distance (2.60–1.80 mm). This lens enabled greater bias potentials to be reached without risking electrical breakdown in vacuum—at the cost of a somewhat lower numerical aperture (0.70 NA). Each FM image was comprised of two 5 s exposures: (1) 555 nm excitation for Alexa 594 labelling of insulin and (2) 405 nm excitation for the Hoechst counterstain.

An overview of imaging conditions is provided in Table 2.2. Fluorescence microscopy image tiles were acquired in a  $4 \times 3$  grid encompassing the tissue section. Low-magnification EM images of the same (but slightly smaller) field of view were acquired immediately following the acquisition of each FM image tile. An automated alignment procedure was then executed to register each set of FM and EM image pairs [27]. The information necessary for registration was stored in the metadata of the image tiles for use in post-processing (Section 2.4.5). The stage was then translated by 170  $\mu\text{m}$  such that the FM images overlapped by a significant margin, whereas the low-magnification EM tiles did not. This was done to prevent damage to the FM tiles due to e-beam irradiation. Following low-magnification

CLEM, a  $40 \times 30$  grid of high-magnification EM image tiles was acquired over the section. Each image was acquired in immersion mode at 3 keV primary beam energy with a -1.5 kV bias applied to the stage, resulting in a 1.5 keV landing energy. Of the 1200 high-magnification EM images acquired, 113 were discarded as they consisted of only either EPON or the substrate.

**Table 2.2.** Imaging parameters used for the full-section acquisition of 80 nm rat pancreas tissue via the integrated light-electron microscope.

	<b>FM</b>	<b>EM (Low-mag)</b>	<b>EM (High-mag)</b>
Resolution	107.8 nm/px	38.8 nm/px	4.86 nm/px
Dwell		5 $\mu$ s	2 $\mu$ s
Exposure	5 s		
Field of View	220 $\mu$ m	160 $\mu$ m	20 $\mu$ m

## 2.4.5. Reconstruction

Following image acquisition, EM images were post-processed with histogram matching to correct for variations in intensity thought to have arisen from electron source drift during acquisition (variation in the bias potential delivered by the external power supply was negligible). No corrections were performed on the FM images. FM and EM image dataset was then uploaded to a local server running an instance of render-ws.<sup>1</sup> EM images were stitched together using the method presented in Khairy et al. [36]. The correlative overlay between the FM and low magnification EM image tiles was done using the registration metadata collected at time of acquisition as described in Section 2.4.4.

The process of correlating the FM and stitched, high-magnification EM image tiles consisted of several steps. First, for each low-magnification EM tile, the set of overlapping high mag EM tiles was found. A composite image of the overlapping tiles was then rendered and processed with SIFT to find corresponding point matches with the low mag EM tile [37]. An affine transformation was then computed for this set of features and propagated to the FM tiles such that they overlaid precisely with the stitched together, high mag EM image tiles. The entire sequence of post-processing steps is compiled in a series of jupyter notebooks available in an online repository.<sup>2</sup>

Small  $1024 \times 1024$  px<sup>2</sup> images of the reconstructed dataset are then rendered and exported in a pyramidal format for visualization with CATMAID [38]. Within CATMAID, the FM images are given a false color transformation and the EM images are contrast-inverted for visualization purposes.

---

<sup>1</sup><https://github.com/saalfeldlab/render>

<sup>2</sup><https://github.com/hoogenboom-group/iCAT-workflow>

## 2.A. Supplementary material

### 2.A.1. test subsection

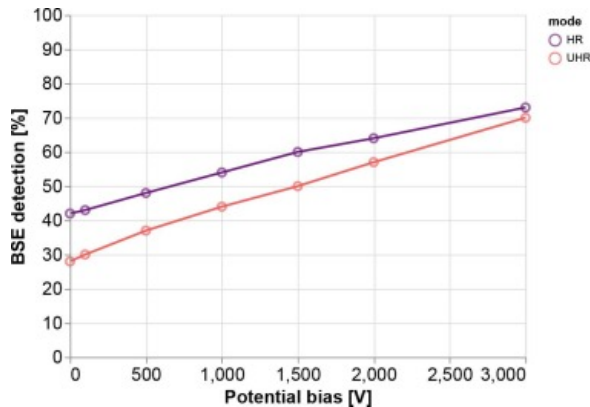


**Figure S1.** BSE collection efficiency increases monotonically down to  $-3\text{ kV}$  potential bias for both non-immersion (HR) and immersion (UHR) imaging modes. **TODO: negative x-axis**

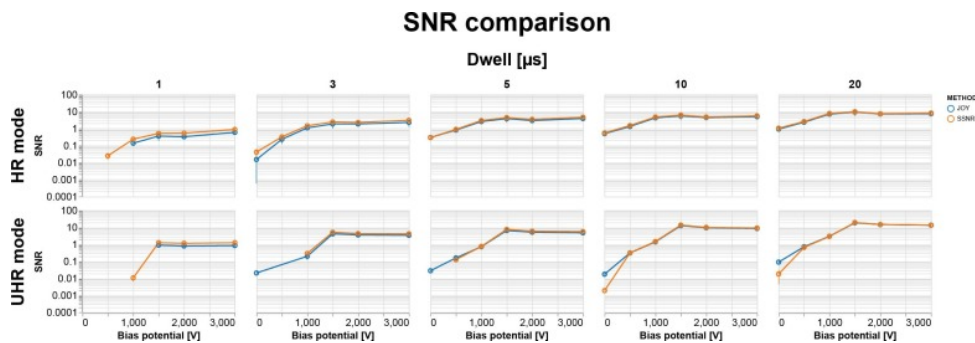


**Figure S2.** Caption.

# REFERENCES

- [1] Ryan Lane et al. “Optimization of negative stage bias potential for faster imaging in large-scale electron microscopy”. *Journal of structural biology: X* 5 (2021), p. 100046.
- [2] Christopher J Peddie and Lucy M Collinson. “Exploring the third dimension: volume electron microscopy comes of age”. *Micron* 61 (2014), pp. 9–19.
- [3] Jeroen Kuipers, Pascal de Boer, and Ben NG Giepmans. “Scanning EM of non-heavy metal stained biosamples: Large-field of view, high contrast and highly efficient immunolabeling”. *Experimental Cell Research* 337.2 (2015), pp. 202–207.
- [4] Jörgen Kornfeld and Winfried Denk. “Progress and remaining challenges in high-throughput volume electron microscopy”. *Current opinion in neurobiology* 50 (2018), pp. 261–267.
- [5] David Grant Colburn Hildebrand et al. “Whole-brain serial-section electron microscopy in larval zebrafish”. *Nature* 545.7654 (2017), pp. 345–349.
- [6] J Delpiano et al. “Automated detection of fluorescent cells in in-resin fluorescence sections for integrated light and electron microscopy”. *Journal of microscopy* 271.1 (2018), pp. 109–119.
- [7] Kenneth J Hayworth et al. “Ultrastructurally smooth thick partitioning and volume stitching for large-scale connectomics”. *Nature methods* 12.4 (2015), pp. 319–322.
- [8] Wenjing Yin et al. “A Petascale Automated Imaging Pipeline for Mapping Neuronal Circuits with High-throughput Transmission Electron Microscopy”. *bioRxiv* (2019), p. 791889.
- [9] Davi D Bock et al. “Network anatomy and in vivo physiology of visual cortical neurons”. *Nature* 471.7337 (2011), pp. 177–182.
- [10] Zhihao Zheng et al. “A complete electron microscopy volume of the brain of adult *Drosophila melanogaster*”. *Cell* 174.3 (2018), pp. 730–743.
- [11] AL Eberle et al. “High-resolution, high-throughput imaging with a multibeam scanning electron microscope”. *Journal of microscopy* 259.2 (2015), pp. 114–120.
- [12] Yan Ren and Pieter Kruit. “Transmission electron imaging in the Delft multibeam scanning electron microscope 1”. *Journal of Vacuum Science & Technology B, Nanotechnology and Microelectronics: Materials, Processing, Measurement, and Phenomena* 34.6 (2016), 06KF02.

- [13] RS Paden and WC Nixon. "Retarding field scanning electron microscopy". *Journal of Physics E: Scientific Instruments* 1.11 (1968), p. 1073.
- [14] D Phifer et al. "Improving SEM imaging performance using beam deceleration". *Microscopy Today* 17.4 (2009), pp. 40–49.
- [15] Keisuke Ohta et al. "Beam deceleration for block-face scanning electron microscopy of embedded biological tissue". *Micron* 43.5 (2012), pp. 612–620.
- [16] Benjamin Titze and Winfried Denk. "Automated in-chamber specimen coating for serial block-face electron microscopy". *Journal of microscopy* 250.2 (2013), pp. 101–110.
- [17] James C Bouwer et al. "Deceleration of probe beam by stage bias potential improves resolution of serial block-face scanning electron microscopic images". *Advanced structural and chemical imaging* 2.1 (2016), pp. 1–13.
- [18] C Shan Xu et al. "Enhanced FIB-SEM systems for large-volume 3D imaging". *Elife* 6 (2017), e25916.
- [19] Agata Šakić et al. "Boron-layer silicon photodiodes for high-efficiency low-energy electron detection". *Solid-state electronics* 65 (2011), pp. 38–44.
- [20] Pascal De Boer, Jacob P Hoogenboom, and Ben NG Giepmans. "Correlated light and electron microscopy: ultrastructure lights up!" *Nature methods* 12.6 (2015), pp. 503–513.
- [21] Yoram Vos et al. "Retarding field integrated fluorescence and electron microscope". *Microscopy and Microanalysis* 27.1 (2021), pp. 109–120.
- [22] Bohumila Lencová and Jakub Zlámal. "A new program for the design of electron microscopes". *Physics Procedia* 1.1 (2008), pp. 315–324.
- [23] Ludwig Reimer. "Emission of backscattered and secondary electrons". *Scanning Electron Microscopy*. Springer, 1998, pp. 135–169.
- [24] I Müllerová and I Konvalina. "Collection of secondary electrons in scanning electron microscopes". *Journal of microscopy* 236.3 (2009), pp. 203–210.
- [25] Michael Unser, Benes L Trus, and Alasdair C Steven. "A new resolution criterion based on spectral signal-to-noise ratios". *Ultramicroscopy* 23.1 (1987), pp. 39–51.
- [26] David C Joy. "SMART—a program to measure SEM resolution and imaging performance". *Journal of Microscopy* 208.1 (2002), pp. 24–34.
- [27] Martijn T Haring et al. "Automated sub-5 nm image registration in integrated correlative fluorescence and electron microscopy using cathodoluminescence pointers". *Scientific reports* 7.1 (2017), pp. 1–9.
- [28] Raimond BG Ravelli et al. "Destruction of tissue, cells and organelles in type 1 diabetic rats presented at macromolecular resolution". *Scientific reports* 3.1 (2013), pp. 1–6.
- [29] Wanda Kukulski et al. "Correlated fluorescence and 3D electron microscopy with high sensitivity and spatial precision". *Journal of Cell Biology* 192.1 (2011), pp. 111–119.

- [30] Christopher J Peddie et al. “Correlative and integrated light and electron microscopy of in-resin GFP fluorescence, used to localise diacylglycerol in mammalian cells”. *Ultramicroscopy* 143 (2014), pp. 3–14.
- [31] RI Koning et al. “Integrated Light and Electron Microscopy”. *Correlative Imaging: Focusing on the Future* (2019), pp. 119–135.
- [32] Ilona Mullerova and Ludek Frank. “Scanning low-energy electron microscopy”. *Advances in imaging and electron physics* 128 (2003), pp. 310–445.
- [33] Jantina Fokkema et al. “Fluorescently labelled silica coated gold nanoparticles as fiducial markers for correlative light and electron microscopy”. *Scientific reports* 8.1 (2018), pp. 1–10.
- [34] Nalan Liv et al. “Simultaneous correlative scanning electron and high-NA fluorescence microscopy”. *PloS one* 8.2 (2013), e55707.
- [35] AC Zonnevylle et al. “Integration of a high-NA light microscope in a scanning electron microscope”. *Journal of microscopy* 252.1 (2013), pp. 58–70.
- [36] Khaled Khairy, Gennady Denisov, and Stephan Saalfeld. “Joint deformable registration of large EM image volumes: a matrix solver approach”. *arXiv preprint arXiv:1804.10019* (2018).
- [37] David G Lowe. “Object recognition from local scale-invariant features”. *Proceedings of the seventh IEEE international conference on computer vision*. Vol. 2. Ieee. 1999, pp. 1150–1157.
- [38] Stephan Saalfeld et al. “CATMAID: collaborative annotation toolkit for massive amounts of image data”. *Bioinformatics* 25.15 (2009), pp. 1984–1986.

# 3

## INTEGRATED ARRAY TOMOGRAPHY FOR 3D CORRELATIVE LIGHT AND ELECTRON MICROSCOPY

Volume electron microscopy (EM) of biological systems has grown exponentially in recent years due to innovative large-scale imaging approaches. As a standalone imaging method, however, large-scale EM typically has two major limitations: slow rates of acquisition and the difficulty to provide targeted biological information. We developed a 3D image acquisition and reconstruction pipeline that overcomes both of these limitations by using a wide-field fluorescence microscope integrated inside of a scanning electron microscope. The workflow consists of acquiring large field of view fluorescence microscopy (FM) images, which guide to regions of interest for successive EM (integrated correlative light and electron microscopy). High precision EM-FM overlay is achieved using cathodoluminescent markers. We conduct a proof-of-concept of our integrated workflow on immunolabelled serial sections of tissues. Acquisitions are limited to regions containing biological targets, expediting total acquisition times and reducing the burden of excess data by tens or hundreds of GBs.

---

This chapter has been published as: Ryan Lane et al. “Integrated array tomography for 3D correlative light and electron microscopy”. *Frontiers in neuroscience* (2022).

### 3.1. Introduction

A central objective within neuroscience and cell biology is to produce high-resolution (1–10 nm), three-dimensional reconstructions of biological specimen. Volume electron microscopy (EM) is the preferred imaging method in this arena because of its unique ability to resolve features across a wide spectrum of spatial scales [2, 3]. While EM provides highly relevant structural information and precise localization of targets, immunogold labeling can only be visualized at high resolution, and in Tokuyasu labeling section areas are typically limited to  $0.01\text{ mm}^2$  for analysis [4, 5]. Fluorescence microscopy (FM) provides biologically relevant information by tagging specific biomolecules with fluorescent labels at large scale [6]. Regions of interest (ROI) can in this way be quickly and reliably identified for subsequent high magnification EM imaging. The information from these two imaging modalities are combined in correlative light and electron microscopy (CLEM). ROI retrieval across different microscopes is, however, nontrivial at large scales, particularly when spread across multiple sections [7, 8, 9, 10, 11]. Other challenges associated with CLEM include the reliance on fiducial markers and intermediate sample preparation [12, 13]. One means of combating these challenges is by merging these separate imaging systems into a single, integrated fluorescence and electron microscope [14]. By detecting fluorescence expression *in-situ*, it can further be decided in an automated fashion which areas to scan at high magnification and which areas to omit for the sake of higher throughput [15]. For array tomography applications, ROIs can be targeted with increasing magnification through a sequence of feedback loops [16]. Similarly, strategies for rapidly screening sections have been developed for sequential CLEM to limit volume acquisitions to select ROI [17, 18].

Despite these potential benefits, an integrated microscope presents new challenges. In conventional array tomography sample preparation, the sample is eluted and restained between imaging methods [19]. Hence, there is no need to preserve fluorescence labelling, which allows for post-staining to enhance EM contrast [20, 21]. The traditional way to compensate for diminished contrast is to boost the EM signal by increasing the dwell time per pixel, but this comes at the expense of throughput. An additional complication in integrated CLEM is electron-beam-induced quenching of the fluorescence [22]. This imposes the constraint that the fluorescence in a given area must be acquired prior to exposure from the electron beam, which prohibits uniformly pre-irradiating the sample with the electron beam to enhance and stabilize contrast [23]. Conversely, in conventional serial-section EM, there are scarce constraints regarding the number of times a particular sample may be scanned, making possible approaches such as that by Hildebrand et al. [24].

Our goal is to establish a workflow capable of quickly and efficiently rendering three-dimensional CLEM volumes from serial sections in such a way as to overcome these challenges. Three key initiatives steered the design of our integrated correlative array tomography (iCAT) procedure. First, to prevent damaging or quenching of the fluorescence signal via electron-beam irradiation, each FM field of view must be acquired prior to EM exposure. Second, to compensate for the reduced

application of contrast agents, backscattered electron (BSE) collection efficiency is enhanced via a negative stage bias, allowing for higher throughput [25, 26]. Finally, a high precision EM-FM overlay is facilitated by the use of cathodoluminescent (CL) points, which eliminates the need for artificial fiducial markers [27]. An alignment method was then developed to reconstruct the correlative image stack. Islets of Langerhans from both rat and zebrafish pancreas tissue were chosen to prototype the imaging and reconstruction workflows. By offering a more holistic visualization of tissue, our integrated approach to 3D CLEM could lead to greater insights in (patho)biology [28].

## 3.2. Material & methods

### 3.2.1. Tissue and sample preparation

Rat pancreas was prepared as follows: fresh pancreas was cut from an 83 day old rat into small pieces and fixed in 4% paraformaldehyde (PFA; Merck) + 0.1% glutaraldehyde (GA; Polysciences) as described in Ravelli et al. [29]. A complete zebrafish larva (120 hpf) was fixed in 2% PFA + 2% GA. Both samples were post-fixed in 1% osmium tetroxide and 1.5% potassium ferricyanide in 0.1 M cacodylate buffer, dehydrated through ethanol and embedded in EPON (Serva). 100 nm serial sections were cut and placed onto formvar-covered ITO-coated glass coverslips (Optics Balzers). Immunolabeling was performed as described previously [23]. Samples were etched with 1% periodic acid for 10 min, followed by a 30 min blocking step: 1% bovine serum albumin (BSA; Sanquin, Netherlands) in tris-buffered saline (TBS), pH 7.4. Next, anti-insulin was incubated for 2 hr (guinea pig; 1:50, Invitrogen, PA1-26938, RRID: AB\_794668, for rat pancreas and anti-insulin; 1:100, Abcam, ab210560, for zebrafish pancreas), followed by washing and subsequent incubation for 1 hr with biotinylated secondary antibody (donkey-anti-guinea pig; 1:400, Jackson Immunoresearch, for rat pancreas and goat-anti-rabbit; 1:400, Dako, for zebrafish pancreas) followed by washing steps. Finally, streptavidin conjugated AF594 (1:100, Jackson Immunoresearch, for rat pancreas) and streptavidin conjugated TRITC (1:100, Jackson Immunoresearch, for zebrafish pancreas) were added for 1 hr followed by washing.

### 3.2.2. Digital light microscopy

The sections, after being placed on the ITO-coated glass slide, are imaged at 30 X magnification ( $\sim 7 \mu\text{m}/\text{px}$ ) using a VHX-6000 digital light microscope (Keyence) operating in reflection mode. To capture every section on the 22 mm  $\times$  22 mm ITO-coated glass slide, a 3  $\times$  3 grid of RGB images is acquired and automatically stitched together.

### 3.2.3. Integrated microscopy

The integrated microscope is a widefield SECOM fluorescence microscope (Delmic B.V.) retrofitted into the vacuum chamber of a Verios 460 SEM (Thermo Fisher Scientific) [14, 30]. The microscopes share a common optical axis, translation stage,

and control software. FM images are obtained with 10 s exposures, recorded by a Zyla 4.2 sCMOS camera (Andor - Oxford Instruments). Excitation wavelengths of 405 nm and 555 nm are used to excite Hoechst and AF594. The SECOM is equipped with a CFI S Plan Fluor ELWD 60XC (0.70 NA) objective (Nikon), which allows for long working distance imaging (1.8–2.6 mm), to prevent electrical breakdown in vacuum, which must be accounted for due to the presence of high electric fields induced by the stage bias [31].

SEM imaging is conducted in two rounds: (1) low-magnification (38 nm/px) scans accompanying each fluorescent acquisition; (2) high-magnification (5 nm/px) acquisitions on ROI identified by fluorescence expression. Both low and high magnification imaging are performed at 2.5 keV primary beam energy with a -1 kV bias potential applied to the sample stage such that the landing energy is 1.5 keV, which proved optimal for ~100 nm sections. The negative potential bias enhances the backscattered electron (BSE) signal, which is collected by the insertable concentric backscattered detector (Thermo Fisher Scientific) [26].

### 3.2.4. Alignment and reconstruction software

Image data from the integrated microscope is uploaded to a local storage server running an instance of render-ws,<sup>1</sup> a collection of open-source web services for rendering transformed image tiles. The tiles and their respective metadata are organized into stacks, configured as MongoDB databases. The alignment routines are arranged in a series of Jupyter notebooks,<sup>2</sup> which parse the image metadata for the EM-FM overlay as well as make calls to render-ws via a python wrapper (render-python<sup>3</sup>). EM image stitching and volume alignment are based on the scale-invariant feature transform (SIFT)—an algorithm designed to detect and match local features in corresponding images [32]. SIFT features are stored in render-ws databases where they can be processed by BigFeta,<sup>4</sup> a linear least squares solver for scalable 2D and 3D image alignment based on point correspondences. CLEM datasets are ultimately exported to CATMAID [33] for google-maps-like visualization. 3D visualizations are done in Fiji [34] using the Volume Viewer plugin.<sup>5</sup>

## 3.3. Results

### 3.3.1. Section detection and *in-situ* navigation

Simple navigation between serial sections within the integrated microscope is crucial. Following joint EM-FM sample preparation (Figure S1A), the sections are imaged by the digital light microscope (DLM) (Figure S1B). To facilitate navigation within the integrated microscope (Figure S1C), the resulting overview image is used for detecting the boundaries of each section on the ITO-coated glass sub-

<sup>1</sup><https://github.com/saalfeldlab/render>

<sup>2</sup><https://github.com/hoogenboom-group/iCAT-workflow>

<sup>3</sup><https://github.com/AllenInstitute/render-python>

<sup>4</sup><https://github.com/AllenInstitute/BigFeta>

<sup>5</sup><https://imagej.net/plugins/volume-viewer>

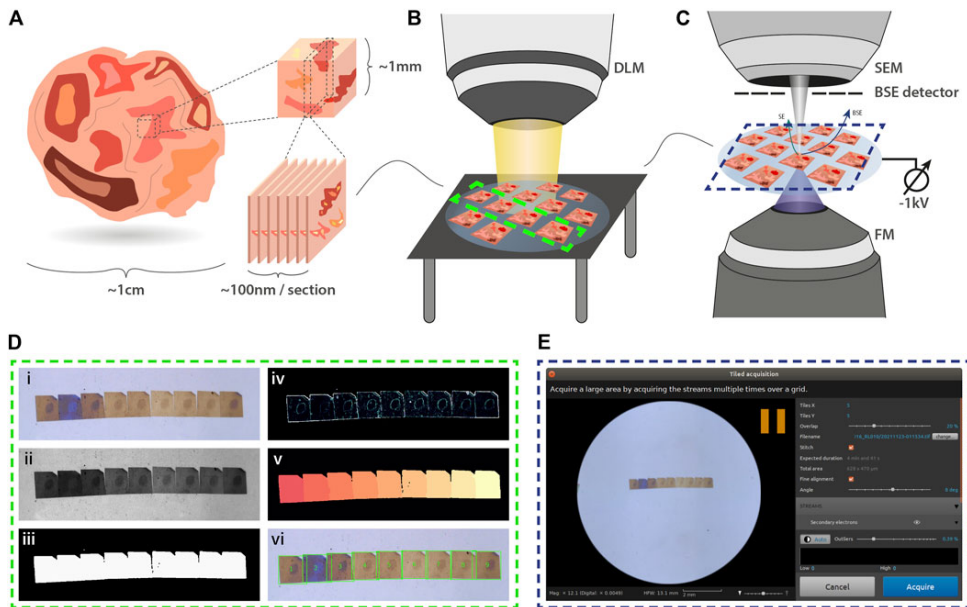


**Figure S1.** Integrated array tomography. (A) Ultrathin sections are prepared for simultaneous FM and EM imaging. (B) An overview image of the sections on the ITO-coated glass slide is then acquired by a digital light microscope (DLM). (C) Next, the sample is transferred to the integrated microscope for CLEM imaging. SEM imaging is performed using a -1 kV bias potential applied to the sample stage to enhance BSE collection from the non-post-stained sections. (D) The overview image obtained by the DLM is used for instance segmentation of the serial sections. Descriptions of the image processing steps (i-vi) is provided in the main text. (E) The section overview image and bounding box coordinates of each serial section are fed to the microscope software to facilitate navigation.

strate via a segmentation routine<sup>6</sup> (Figure S1D). The overview image (inset i) is first contrast enhanced and converted to grayscale (inset ii). Intensity-based thresholding is used to create a binary mask image (inset iii), which is then applied to the grayscale image. To retrieve outlines of the section boundaries, the gradient is computed (inset iv). Watershed segmentation is then implemented by flooding the gradient image with a number of markers equal to the number of serial sections in the image (inset v). The resulting labelled image (inset vi) then serves as input for navigation using a plugin within Odemis,<sup>7</sup> the open-source software that controls the microscope (Figure S1E).

<sup>6</sup><https://github.com/hoogenboom-group/secdetect>

<sup>7</sup><https://github.com/delmic/odemis>

### 3.3.2. Targeted correlative acquisition of an individual region of interest

To identify ROI in the integrated microscope for subsequent EM acquisition, the correlative imaging scheme is engineered to obtain fluorescence overviews of each section, undamaged by the electron beam. The workflow starts by acquiring a FM and low-magnification EM image tile (Figure S2A). The FM tile is acquired prior to the EM tile to preserve the fluorescence signal. An automated registration routine guided by cathodoluminescent (CL) spots is then run to register the image pair [27]. This sequence of correlative imaging is automatically repeated in a grid-like pattern, encompassing the entire section. FM image tiles are acquired with a 20% overlap such that they can be stitched together to allow for fluorescence-based ROI detection within each section (Figure S2B). The field width of the EM tile ( $\sim 140 \mu\text{m}$ ) is chosen such that it spans the maximum extent possible without entering the overlap region of the neighboring FM image tiles,

$$w_{EM} = w_{FM} - 2o_{FM}w_{FM} \quad (3.1)$$

where  $w_{EM}$  and  $w_{FM}$  are the respective EM and FM fields of view, and  $o_{FM}$  is the overlap between adjacent FM tiles. In this way EM-FM registration is performed over as large an area as possible, while avoiding bleaching of the fluorescence. Fluorescence imaging of the entire section prior to EM would fulfil the same objective while circumventing the need for gaps between low-magnification EM image tiles. This would require manually registering the tilesets, however, as the transformation obtained from the CL registration procedure is unique to each image pair.

Fluorescence expression is then used to target areas for additional EM imaging at higher magnification (5 nm/px) (Figure S2C). The ROI is manually navigated to via stage translation, whereby an automated tileset acquisition is initiated (Figure S2D). The tiles are spaced with a 10–15% overlap such that they can be stitched during post-processing. The correlative imaging pipeline is then repeated on the remaining serial sections.

### 3.3.3. 2D Stitching and correlation

Overlaying the fluorescence onto the high-magnification EM requires correlating the datasets across different modalities and spatial scales. Each FM tile is first overlaid onto the corresponding low-magnification EM tile using the metadata generated by the CL registration procedure. A grid of CL spots is recorded with the camera of the fluorescence microscope in the absence of excitation light (Figure S3A). The appropriate affine transformation is calculated by localizing each CL spot and matching it with the known position of the electron beam (“cross-modal” registration) [27]. The stage coordinates are extracted to then correlate and position each image pair in the tileset (Figure S3A).

The high-magnification EM tileset is stitched independently of both the FM and low-magnification EM tiles (Figure S3B). Stage coordinates are used to first establish a set of potential neighboring tiles. For each tile, SIFT features are extracted and matched between the candidate neighbors. Affine transformation parameters

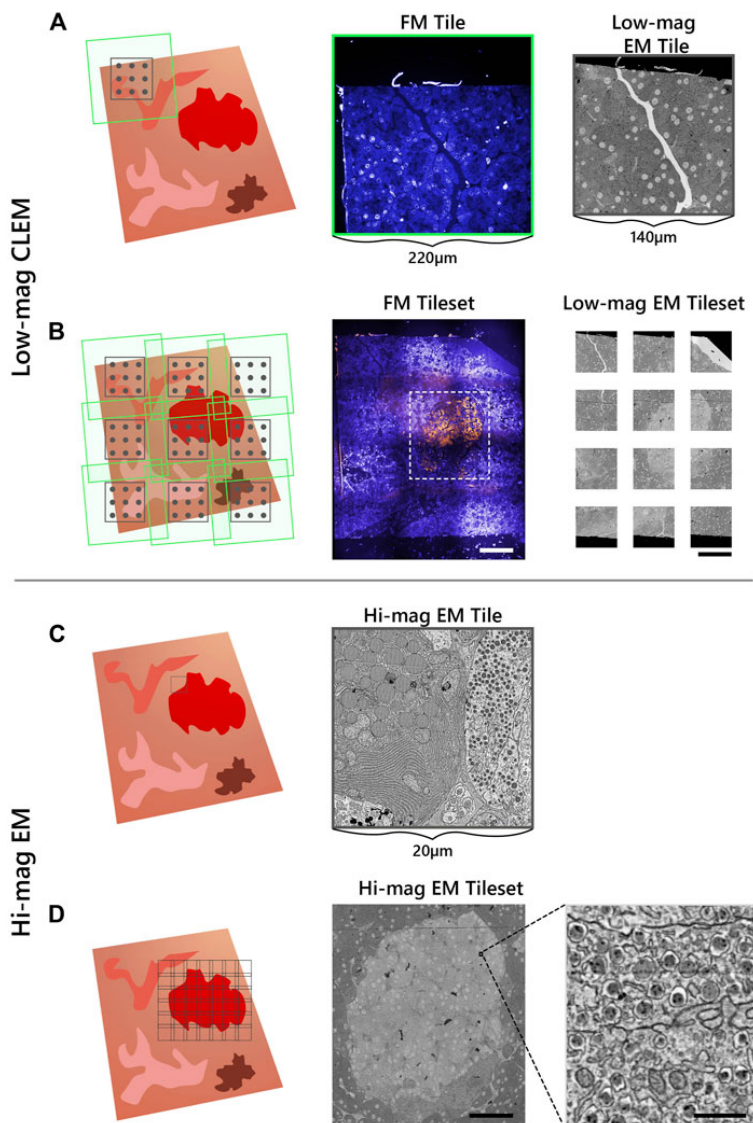


**Figure S2.** Integrated array tomography provides efficient, high-precision EM-FM imaging without bleaching of the fluorescence. (A) Acquisition of correlative FM (green outline) and low-magnification EM (black outline) images, followed by a registration procedure involving CL spots (grey circles) to register the image pair. (B) The stage is translated in a grid-like fashion such that there is sufficient overlap between neighboring FM image tiles—leaving a gap between adjacent EM tiles. (C) The fluorescence signal is used to identify targets for subsequent EM imaging (black outline). (D) The target ROI is captured by an automated tileset of high magnification EM tiles. Scalebars: (B) 100  $\mu$ m; (D) 50  $\mu$ m (inset, 0.5  $\mu$ m).

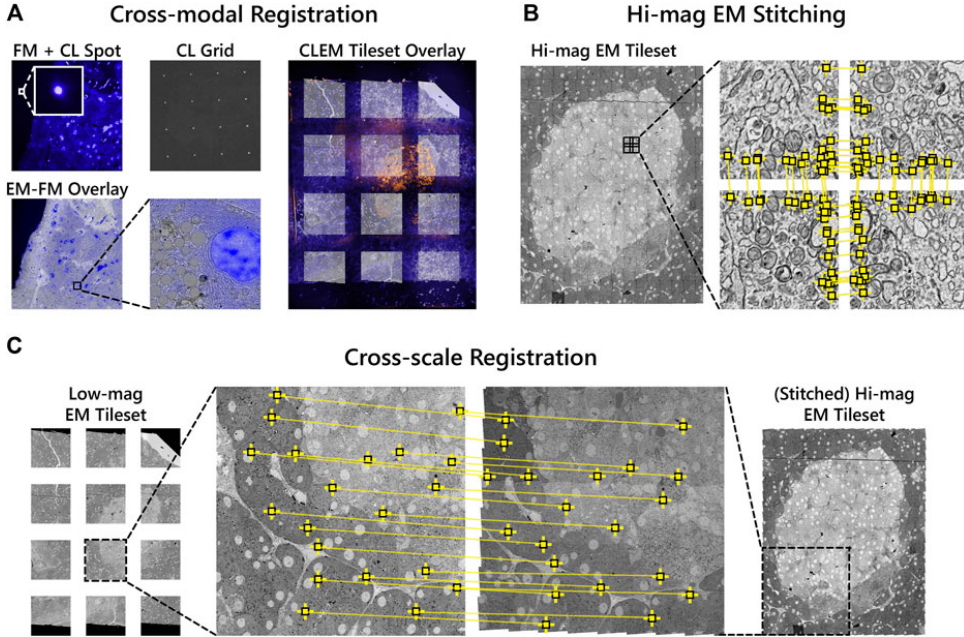


**Figure S3.** Correlative alignment routine registers tilesets across modalities and scales. (A) Automated registration procedure for registering FM and low-magnification EM image pairs using CL spots. FM tiles are then overlaid onto the low-magnification EM tiles of each section. (B) SIFT features (yellow squares) are extracted and used to stitch together neighboring high-magnification EM tiles within each section. (C) Low-magnification EM images are registered to the corresponding area of the stitched together high-magnification EM tileset. The low-magnification tiles thereby serve as a reference to ultimately overlay the fluorescence onto the high-magnification EM.

for each tile are then estimated by minimizing the squared distance between corresponding features [35, 36].

Next, the low-magnification image tiles are registered to the corresponding area of the stitched high-magnification EM tileset (“cross-spatial” registration, Figure S3C). Stage coordinates are used to determine the set of high-magnification tiles that overlap with each low-magnification tile. A composite image of the overlapping tiles is rendered, processed with SIFT, and matched with the features in the low-magnification tile. The affine transformation computed from the feature matching is then propagated to each of the FM tiles such that they are overlaid onto the high-magnification EM tileset. In this way, the low-magnification EM serves as a proxy to correlate the fluorescence to the high-magnification EM. The overlay accuracy is reduced in the areas between low-magnification tiles where the transformation is extrapolated (Supplementary Figure 3.S1A – F). This can be corrected for via (manual) landmark registration by e.g. aligning the Hoechst signal to nuclei recognized in the EM using software such as ec-CLEM [37], which is routinely

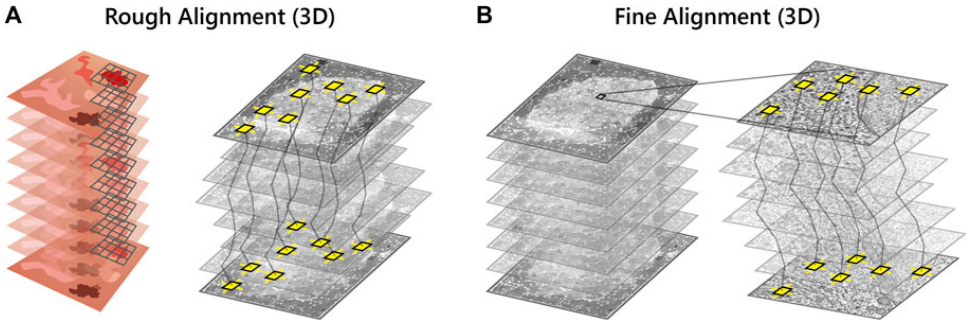


**Figure S4.** Volume reconstruction of the high-magnification EM stack. (A) SIFT features (yellow squares) are used to roughly align the high-magnification EM stack in  $z$ . A downsampled image of each section is rendered as the full resolution EM tileset is too large (several GB) for feature extraction. (B) The EM stack alignment is refined by least squares optimization of the displacement between matched features.

used for image registration in sequential CLEM experiments [38, 39, 40]. In general, the overlay accuracy cannot be expected to be below the pixel size of the low magnification EM.

### 3.3.4. Correlative 3D reconstruction

A robust and scalable solution is required for volume alignment of the high-magnification EM stack, the “backbone” of the multimodal dataset. The stitched sections are downsampled and roughly aligned in  $z$  (Figure S4A) to facilitate feature mapping between image tiles in adjacent sections. A system of linear equations consisting of SIFT features is then solved to finely align the image stack in 3D (Figure S4B) [36]. The features extracted during stitching are reused, enabling a faster and more efficient reconstruction of the EM volume.

The 2D correlative alignment procedure (Figure S3) is then run on each section, mapping the fluorescence onto the high-magnification EM volume. The nine serial sections of rat pancreas were thereby used to realize a proof-of-concept of the iCAT workflow (Figure S5A). An islet of Langerhans was identified from anti-insulin immunofluorescence of AF594 and chosen for subsequent, high-magnification EM imaging (Figure S5B). The fluorescence data clearly delineates the endocrine region from the surrounding exocrine tissue, which is characterized by dense endoplasmic reticulum (ER) and the absence of insulin labeling (Figure S5C). Although it was chosen as a nuclear marker, Hoechst also binds to the RNA present in the ER. The endocrine region, in contrast, is characterized by an abundance of insulin-secreting beta cells with distinct nuclei. The high EM-FM registration accuracy afforded by iCAT enables a clear distinction between different types of granules present in the endocrine tissue (Figure S5D). Discerning insulin from other hormone granules is nontrivial as all are roughly 100 nm in diameter. Making this differentiation from EM data alone requires expert-level interpretation.

By limiting high-magnification EM to only the islet, the total imaging volume is

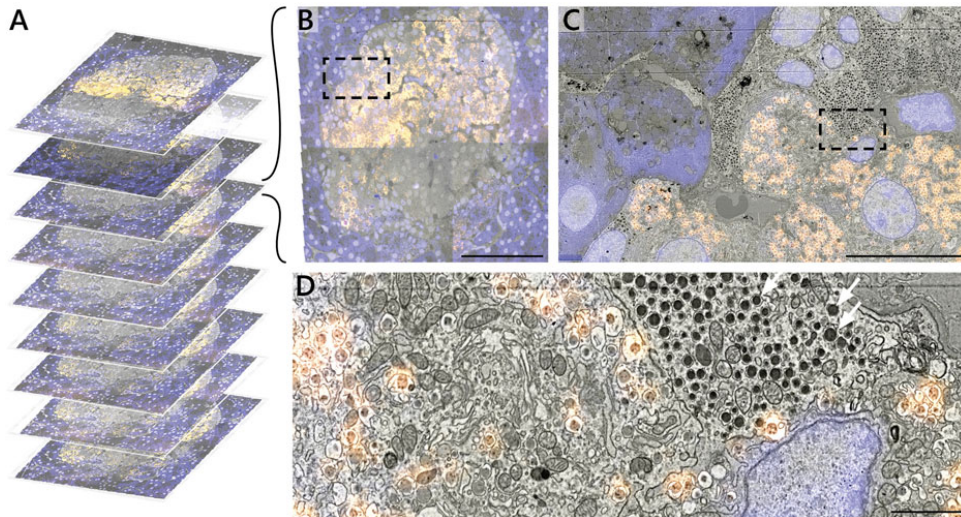


**Figure S5.** Correlative reconstruction of nine sections of pancreas. (A) 2D and 3D alignment routines are combined to yield a CLEM stack of nine serial sections of rat pancreas tissue. (B – D) CLEM imaging of the islet of Langerhans at varying spatial resolution. Hoechst (blue) and AF594 (orange) fluorescence signals are superimposed onto the EM ultrastructure. The AF594 signal, in particular, facilitates recognition of insulin granules from e.g. non-fluorescent glucagon granules (white arrows, D). Scale bars: (B) 50  $\mu\text{m}$ ; (C) 5  $\mu\text{m}$ ; (D) 1  $\mu\text{m}$ . Raw data at full resolution is available via Nanotomy.

reduced by a factor  $\sim 10$  with respect to the full section volume ( $0.03 \text{ mm}^2$  per islet vs  $0.4 \text{ mm}^2$  per section). Similar reductions are realized in the total dataset size (0.1 vs  $\sim 1 \text{ TB}$ ) easing data management requirements. This initial proof of concept was designed around only a limited number of serial sections to more efficiently optimize each procedure in the workflow.

### 3.3.5. Proof of concept on zebrafish pancreas tissue

To demonstrate the scalability of the workflow, we applied it to a larger volume of larval zebrafish (Figure S6). The Hoechst signal was useful in identifying the exocrine region of the pancreas (Figure S6B) as the insulin immunofluorescence from TRITC was weak. TRITC was chosen for its stronger fluorescence in vacuum compared to Alexa dyes (manuscript in preparation); potential causes for the weak immunofluorescence in the zebrafish pancreas are still under investigation. The exocrine region, encompassing an islet of Langerhans, together with the underlying muscle tissue was selected for high magnification EM. The reconstruction of the CLEM volume was cropped to remove the background fluorescence in the swim bladder (Figure S6C). Sub-stacks within the correlative volume were then extracted for further analysis (Figures S6D, G). Note that the ultrastructure is better preserved in most tissues than in the islet (Figure S6H, I), a phenomenon previously seen in other species (unpublished results).

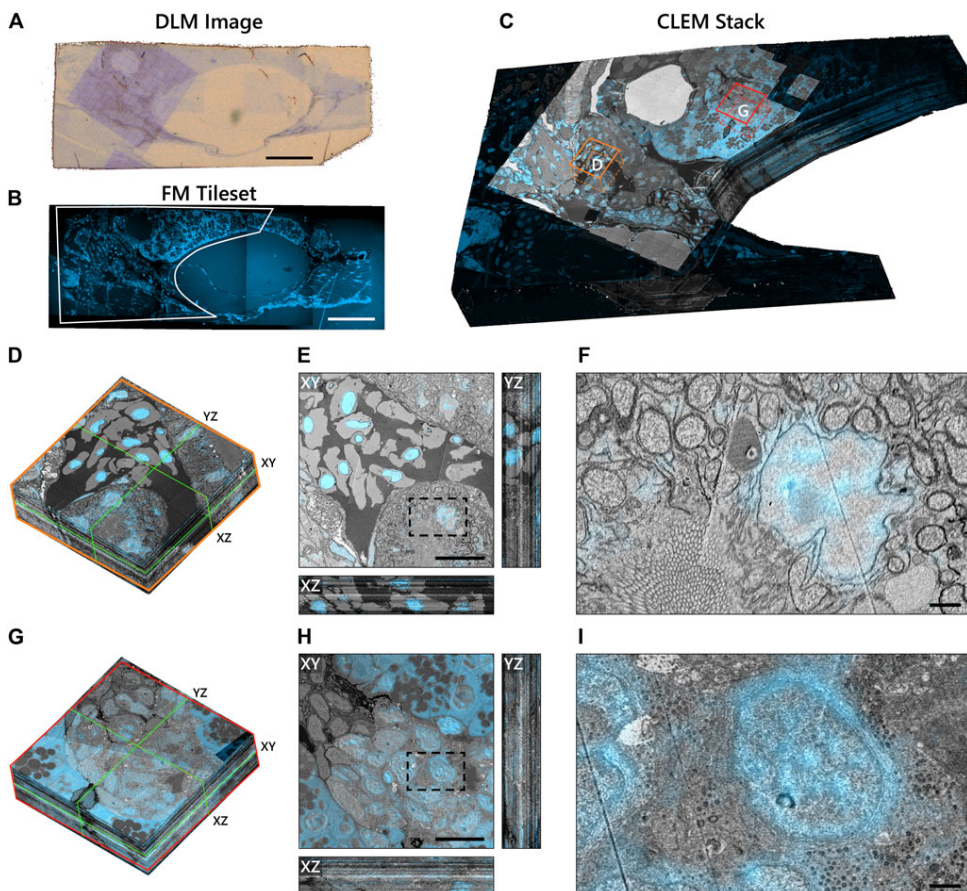


**Figure S6.** Integrated correlative array tomography applied to 63 serial sections of zebrafish pancreas. (A) Contrast-enhanced optical image of an individual serial section obtained by the DLM. The section was re-acquired post-EM imaging, revealing the region of interest irradiated by the electron beam. The biological material can be seen in pale blue in contrast with the bare EPON (brown background). (B) Hoechst signal of an individual serial section, outlining (white) the portion of the tissue shown in (C). (C) CLEM volume of the zebrafish tissue cropped to the ROI selected for high-magnification EM imaging—plus a portion of the surrounding fluorescence signal. Sub-stacks for inspection are denoted by orange (D – F) and red (G – I) boxes. (D) 3D sub-stack of muscle tissue within the zebrafish pancreas. Green lines indicate orthoslices of the XY, XZ, and YZ planes shown in (E). (F) Zoomed-in region of the XY plane showing high-precision FM overlay of Hoechst onto a cell nucleus. (G – I) Same as in (D – F), but for an islet of Langerhans. Ill-defined cell and organelle membranes in (H) and (I) indicate suboptimal preservation of the ultrastructure in this region of the pancreas. Scale bars: (A, B) 100 µm; (E, H) 10 µm; (F, I) 1 µm. Raw data at full resolution is available via Nanotomy.

We generally observe high EM-FM overlay precision as evidenced by the Hoechst signal confined to the nuclear envelope in the muscle tissue (Figure S6E, F). The registration accuracy does, however, exhibit variability in several sections—more so than is seen in the rat pancreas tissue where it appears limited to the gaps between low-magnification EM tiles. In these instances, the inaccuracy stems from a malfunction in the CL registration procedure itself (Supplementary Figure 3.S1G–N). Variations in the EM image intensity, particularly in the islet, can also be observed for a number of sections (Figure S6H: XZ and YZ cross-sections). We attribute these artifacts primarily to ultrastructure preservation as they do not appear to be as prevalent in the muscle tissue. While the SEM imaging parameters and detection settings were held constant throughout the acquisition, day-to-day changes in the environment (e.g. temperature, humidity levels) may have varied.

In total, 66 sections were prepared, of which three ( $z = 9, 10, 34$ ) were discarded due to excess surface debris. The omission of consecutive sections was mitigated by extending the SIFT feature depth search from 2 to 3 such that sections  $z = 8$  and  $z = 11$  could be registered. Total acquisition times for low-magnification CLEM and high-magnification EM were 7.2 hr and 71 hr respectively, versus 335 hr for full section imaging at high-magnification.

### 3.4. Discussion

A new workflow for integrated array tomography for the semi-automated acquisition and reconstruction of volume CLEM data is presented. High-resolution EM is limited to select ROI by targeting areas based on fluorescence expression. This not only expedites acquisition time, but eases the burden on data management requirements. Interpretation of EM data is in turn facilitated by the addition of fluorescent labels. The workflow demonstrated here extends the work of Liv et al. [14], which introduced the integrated microscope, and Haring et al. [27], which presented the fiducial-free CL registration procedure, to targeted correlative imaging of serial sections. Gabarre et al. [16] presented an alternative method for integrated array tomography in which light microscopy and EM are combined to localize structures through a series of feedback loops. Our approach differs in several ways. First, fluorescence imaging is done *in-vacuo* as opposed to transmitted light microscopy done at ambient pressure. This allows for more automated EM-FM (or EM-LM) overlay, as the CL registration procedure can only be done in high vacuum [27]. Additionally, the multi-modal alignment methodology conceived here offers a more scalable solution for generating volumetric CLEM data. Integrated array tomography was inspired in part by the multi-scale approach of Hildebrand et al. [24], in which full brain EM imaging of a larval zebrafish was conducted by selecting ROI for subsequent acquisition based on inspection between imaging rounds. In this work, conversely, ROI are identified by *in-situ* fluorescence, bypassing the need for post-processing and alignment between magnification scales.

On-section immunofluorescence and fluorescent staining constitute viable options for FM imaging of resin-embedded sections in high vacuum. Pancreas tissue in particular is well-suited for immunofluorescence due to the prevalence of

insulin epitopes. While in both nature and technique development, immunolabeling approaches are always dependent on the capacity for antibodies and epitopes to interact, this is typically inefficient for most antibodies, and particularly so for EPON-embedded sections. We find that approximately 1 in 10 antibodies tested in our lab are applicable for EPON labeling. While acrylic resins (e.g. Lowicryl, LR White) have been shown to be more compatible with immunolabeling, a trade-off must be made between the strength of the fluorescence signal and the quality of the ultrastructure [41, 42]. Complications with serial sectioning and ultrastructure preservation (beyond that shown in the zebrafish pancreas) arose when experimenting with Lowicryl; hence EPON was selected as the embedding medium for this study.

Probes typically used for live FM, such as fluorescent proteins, are likewise incompatible with conventional EM sample preparation techniques [12]. Although protocols have been developed for retaining fluorescence post-embedding [43, 41, 44, 45], the same compromises exist between fluorescence retention and ultrastructure preservation. Fluorescent proteins have the additional limitation that the specimen must be genetically modified, rendering them unsuitable for use in native animals and humans. In-resin fluorescence preservation thus remains a challenge—only made more difficult by imposing high vacuum conditions, which may lower fluorescence intensities for biological probes typically optimized for use in aqueous environments [44]. We are nevertheless confident that future developments in fluorescent proteins and embedding media will present compelling opportunities to apply integrated array tomography to a variety of biological questions.

We foresee that the multimodal datasets obtained using this method will be instrumental in forthcoming machine learning applications [46, 47, 48]. Thus far, applications of registered EM-FM datasets appear to be limited to facilitating registration of sequential CLEM data using artificial predictions for the fluorescence signal [49, 50]. Volume EM datasets, particularly in connectomics, are now routinely segmented via deep convolutional neural networks [51, 48]. Acquisition rates and manual annotation of datasets, however, both serve as bottlenecks for reconstructing dense networks of cells and organelles [3]. Given its ability to provide labeled biological information as well as reduce imaging volumes to select regions, integrated array tomography is poised to deliver significant gains in this arena.

Future work will be directed towards further refinement and automation. The CL registration procedure could be made more robust by illuminating the sample with a greater number of CL spots or by increasing the camera integration time. Updates to the alignment software could furthermore allow for the distortion field correction used in Haring et al. [27] to achieve sub-5 nm overlay precision. Cutting sections manually remains a significant bottleneck for throughput, as it is prone to error and requires expert training [52]. We expanded from a single section to nine, to 63, and have now placed more than 100 serial sections onto ITO-coated coverslips. Increasing beyond ~10 µm of biological material, however, is cumbersome without more sophisticated sectioning techniques such as automated tape-collecting ultramicrotome (ATUM) [53] or magnetic collection [54]. These may in-

introduce their respective complications; ATUM, for example, is designed to collect sections on (opaque) Kapton tape. More extensive automation strategies can alternatively be applied to the correlative imaging pipeline. Delpiano et al. [15] devised a way to automatically detect fluorescent cells using an integrated light and electron microscope. We envision a workflow for fully automated integrated array tomography in which fluorescent ROIs are automatically recognized, navigated to, and acquired, rendering three-dimensional CLEM datasets tailored to answer the specific biological research question.

### 3.5. Supplementary material

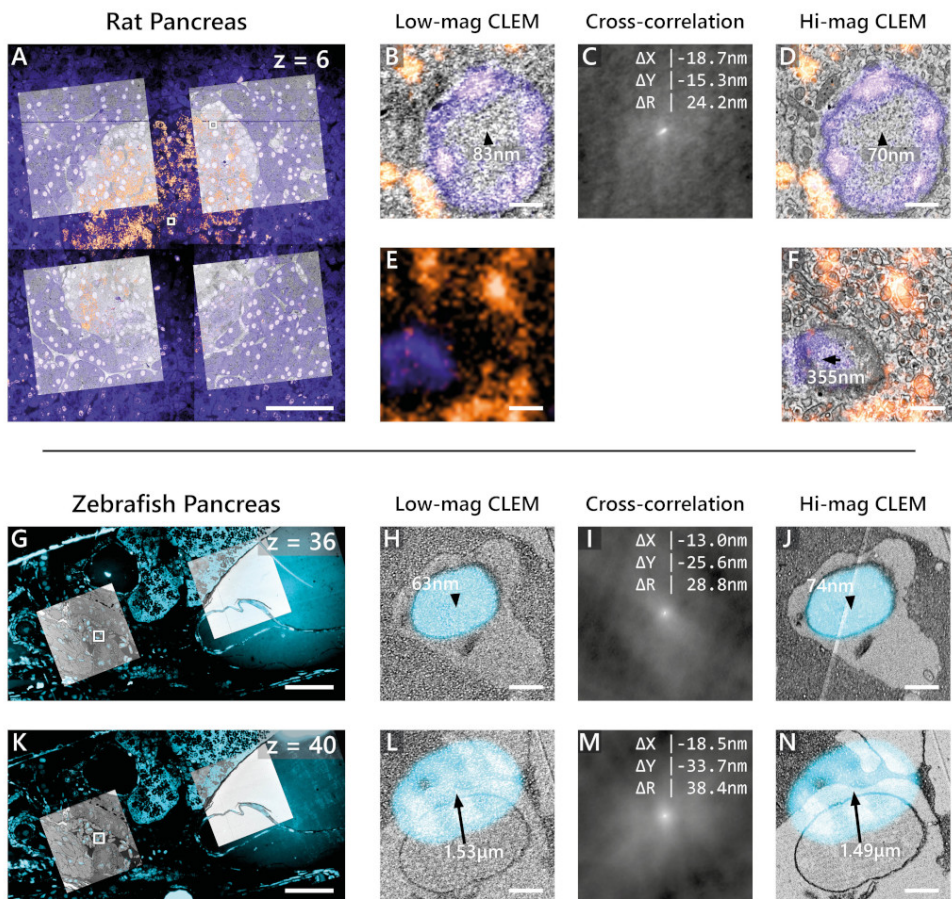


**Figure 3.S1.** Reduced overlay accuracy due to extrapolation and errors in the CL registration procedure. Overlay (in)accuracy is a combination of the errors in the cross-modal and cross-spatial registration procedures. (A) Partial low-magnification CLEM tileset of rat pancreas from which features inside (B – D) and outside (E – F) a low-magnification EM tile were selected to assess the overlay accuracy (denoted by white squares). (B) Cross-modal registration error for a cell nucleus in low-magnification CLEM, measured by calculating the centroid of the nucleus in both modalities and computing the relative displacement. (C) Cross-spatial registration error as measured by the phase correlation between the low and high-magnification EM. (D) Sub-100 nm overlay accuracy for the cell nucleus in high-magnification CLEM. (E – F) Same as in (B) and (D) for a cell nucleus acquired outside of a low-magnification EM tile. Overlay accuracy is reduced to several hundred nanometers due to the imprecision incurred by extrapolating the cross-modal registration. (Continued on next page...)

**Figure 3.S1.** (G) Partial low-magnification CLEM tilesset of zebrafish pancreas from a section in which the CL registration procedure achieved the expected precision. (H – J) Same as in (B – D) but for a nucleus in the zebrafish pancreas. (K – N) Same as in (G – J) but for the section with the lowest apparent overlay accuracy ( $1.5\text{ }\mu\text{m}$ ). The inaccuracy is dominated by an error in the cross-modal registration as the phase correlation (M) shows a sub-50 nm translation. Possible causes for the error include poor CL spot localization due to noise in the CL signal. Scale bars: (A)  $50\text{ }\mu\text{m}$ ; (B, D, E, F)  $0.5\text{ }\mu\text{m}$ ; (G, K)  $50\text{ }\mu\text{m}$ ; (H, J, L, N)  $1\text{ }\mu\text{m}$ .

# REFERENCES

- [1] Ryan Lane et al. “Integrated array tomography for 3D correlative light and electron microscopy”. *Frontiers in neuroscience* (2022).
- [2] Christopher J Peddie and Lucy M Collinson. “Exploring the third dimension: volume electron microscopy comes of age”. *Micron* 61 (2014), pp. 9–19.
- [3] Jörgen Kornfeld and Winfried Denk. “Progress and remaining challenges in high-throughput volume electron microscopy”. *Current opinion in neurobiology* 50 (2018), pp. 261–267.
- [4] Willisa Liou, Hans J Geuze, and Jan W Slot. “Improving structural integrity of cryosections for immunogold labeling”. *Histochemistry and cell biology* 106.1 (1996), pp. 41–58.
- [5] Carolien Van Rijnsoever, Viola Oorschot, and Judith Klumperman. “Correlative light-electron microscopy (CLEM) combining live-cell imaging and immunolabeling of ultrathin cryosections”. *Nature methods* 5.11 (2008), pp. 973–980.
- [6] Ben NG Giepmans et al. “The fluorescent toolbox for assessing protein location and function”. *science* 312.5771 (2006), pp. 217–224.
- [7] Roman S Polishchuk et al. “Correlative light-electron microscopy reveals the tubular-saccular ultrastructure of carriers operating between Golgi apparatus and plasma membrane”. *The Journal of cell biology* 148.1 (2000), pp. 45–58.
- [8] Derron Bishop et al. “Near-infrared branding efficiently correlates light and electron microscopy”. *Nature methods* 8.7 (2011), pp. 568–570.
- [9] Matthia A Karreman et al. “Correlating intravital multi-photon microscopy to 3D electron microscopy of invading tumor cells using anatomical reference points”. *PloS one* 9.12 (2014), e114448.
- [10] Lucy M Collinson, Elizabeth C Carroll, and Jacob P Hoogenboom. “Correlating 3D light to 3D electron microscopy for systems biology”. *Current Opinion in Biomedical Engineering* 3 (2017), pp. 49–55.
- [11] Daniel G Booth et al. “SuperCLEM: an accessible correlative light and electron microscopy approach for investigation of neurons and glia in vitro”. *Biology open* 8.5 (2019), bio042085.
- [12] Pascal De Boer, Jacob P Hoogenboom, and Ben NG Giepmans. “Correlated light and electron microscopy: ultrastructure lights up!” *Nature methods* 12.6 (2015), pp. 503–513.

- [13] Matthia A Karreman et al. “Intravital correlative microscopy: imaging life at the nanoscale”. *Trends in cell biology* 26.11 (2016), pp. 848–863.
- [14] Nalan Liv et al. “Simultaneous correlative scanning electron and high-NA fluorescence microscopy”. *PLoS one* 8.2 (2013), e55707.
- [15] J Delpiano et al. “Automated detection of fluorescent cells in in-resin fluorescence sections for integrated light and electron microscopy”. *Journal of microscopy* 271.1 (2018), pp. 109–119.
- [16] Sergio Gabarre et al. “A workflow for streamlined acquisition and correlation of serial regions of interest in array tomography”. *BMC biology* 19.1 (2021), pp. 1–15.
- [17] Agnes Burel et al. “A targeted 3D EM and correlative microscopy method using SEM array tomography”. *Development* 145.12 (2018), dev160879.
- [18] Paolo Ronchi et al. “High-precision targeting workflow for volume electron microscopy”. *Journal of Cell Biology* 220.9 (2021), e202104069.
- [19] Kristina D Micheva and Stephen J Smith. “Array tomography: a new tool for imaging the molecular architecture and ultrastructure of neural circuits”. *Neuron* 55.1 (2007), pp. 25–36.
- [20] Michael L Watson. “Staining of tissue sections for electron microscopy with heavy metals”. *The Journal of Cell Biology* 4.4 (1958), pp. 475–478.
- [21] Juan Carlos Tapia et al. “High-contrast en bloc staining of neuronal tissue for field emission scanning electron microscopy”. *Nature protocols* 7.2 (2012), pp. 193–206.
- [22] Aditi Srinivasa Raja et al. “Electron-Beam Induced Luminescence and Bleaching in Polymer Resins and Embedded Biomaterial”. *Macromolecular bioscience* (2021), p. 2100192.
- [23] Jeroen Kuipers, Pascal de Boer, and Ben NG Giepmans. “Scanning EM of non-heavy metal stained biosamples: Large-field of view, high contrast and highly efficient immunolabeling”. *Experimental Cell Research* 337.2 (2015), pp. 202–207.
- [24] David Grant Colburn Hildebrand et al. “Whole-brain serial-section electron microscopy in larval zebrafish”. *Nature* 545.7654 (2017), pp. 345–349.
- [25] James C Bouwer et al. “Deceleration of probe beam by stage bias potential improves resolution of serial block-face scanning electron microscopic images”. *Advanced structural and chemical imaging* 2.1 (2016), pp. 1–13.
- [26] Ryan Lane et al. “Optimization of negative stage bias potential for faster imaging in large-scale electron microscopy”. *Journal of structural biology: X* 5 (2021), p. 100046.
- [27] Martijn T Haring et al. “Automated sub-5 nm image registration in integrated correlative fluorescence and electron microscopy using cathodoluminescence pointers”. *Scientific reports* 7.1 (2017), pp. 1–9.

- [28] Pascal de Boer et al. “Large-scale electron microscopy database for human type 1 diabetes”. *Nature communications* 11.1 (2020), pp. 1–9.
- [29] Raimond BG Ravelli et al. “Destruction of tissue, cells and organelles in type 1 diabetic rats presented at macromolecular resolution”. *Scientific reports* 3.1 (2013), pp. 1–6.
- [30] AC Zonnevylle et al. “Integration of a high-NA light microscope in a scanning electron microscope”. *Journal of microscopy* 252.1 (2013), pp. 58–70.
- [31] Yoram Vos et al. “Retarding field integrated fluorescence and electron microscope”. *Microscopy and Microanalysis* 27.1 (2021), pp. 109–120.
- [32] David G Lowe. “Object recognition from local scale-invariant features”. *Proceedings of the seventh IEEE international conference on computer vision*. Vol. 2. Ieee. 1999, pp. 1150–1157.
- [33] Stephan Saalfeld et al. “CATMAID: collaborative annotation toolkit for massive amounts of image data”. *Bioinformatics* 25.15 (2009), pp. 1984–1986.
- [34] Johannes Schindelin et al. “Fiji: an open-source platform for biological-image analysis”. *Nature methods* 9.7 (2012), pp. 676–682.
- [35] Stephan Saalfeld et al. “Elastic volume reconstruction from series of ultra-thin microscopy sections”. *Nature methods* 9.7 (2012), pp. 717–720.
- [36] Khaled Khairy, Gennady Denisov, and Stephan Saalfeld. “Joint deformable registration of large EM image volumes: a matrix solver approach”. *arXiv preprint arXiv:1804.10019* (2018).
- [37] Perrine Paul-Gilloteaux et al. “eC-CLEM: flexible multidimensional registration software for correlative microscopies”. *Nature methods* 14.2 (2017), pp. 102–103.
- [38] Christian Franke et al. “Correlative single-molecule localization microscopy and electron tomography reveals endosome nanoscale domains”. *Traffic* 20.8 (2019), pp. 601–617.
- [39] Maarten W Tijntel et al. “Correlative cryo super-resolution light and electron microscopy on mammalian cells using fluorescent proteins”. *Scientific reports* 9.1 (2019), pp. 1–11.
- [40] Chia-Wei Lee et al. “Selective autophagy degrades nuclear pore complexes”. *Nature cell biology* 22.2 (2020), pp. 159–166.
- [41] Shigeki Watanabe et al. “Protein localization in electron micrographs using fluorescence nanoscopy”. *Nature methods* 8.1 (2011), pp. 80–84.
- [42] Maria G Paez-Segala et al. “Fixation-resistant photoactivatable fluorescent proteins for CLEM”. *Nature methods* 12.3 (2015), pp. 215–218.
- [43] Wanda Kukulski et al. “Correlated fluorescence and 3D electron microscopy with high sensitivity and spatial precision”. *Journal of Cell Biology* 192.1 (2011), pp. 111–119.

- [44] Christopher J Peddie et al. “Correlative and integrated light and electron microscopy of in-resin GFP fluorescence, used to localise diacylglycerol in mammalian cells”. *Ultramicroscopy* 143 (2014), pp. 3–14.
- [45] Zhifei Fu et al. “mEosEM withstands osmium staining and Epon embedding for super-resolution CLEM”. *Nature methods* 17.1 (2020), pp. 55–58.
- [46] Nils Eckstein et al. “Microtubule Tracking in Electron Microscopy Volumes”. *International Conference on Medical Image Computing and Computer-Assisted Intervention*. Springer. 2020, pp. 99–108.
- [47] Jing Liu et al. “Automatic reconstruction of mitochondria and endoplasmic reticulum in electron microscopy volumes by deep learning”. *Frontiers in neuroscience* 14 (2020), p. 599.
- [48] Larissa Heinrich et al. “Whole-cell organelle segmentation in volume electron microscopy”. *Nature* 599.7883 (2021), pp. 141–146.
- [49] Chawin Ounkomol et al. “Label-free prediction of three-dimensional fluorescence images from transmitted-light microscopy”. *Nature methods* 15.11 (2018), pp. 917–920.
- [50] Rick Seifert et al. “DeepCLEM: automated registration for correlative light and electron microscopy using deep learning”. *F1000Research* 9.1275 (2020), p. 1275.
- [51] Julia Buhmann et al. “Automatic detection of synaptic partners in a whole-brain Drosophila electron microscopy data set”. *Nature Methods* 18.7 (2021), pp. 771–774.
- [52] AA Wanner, MA Kirschmann, and C Genoud. “Challenges of microtome-based serial block-face scanning electron microscopy in neuroscience”. *Journal of microscopy* 259.2 (2015), pp. 137–142.
- [53] Kenneth J Hayworth et al. “Imaging ATUM ultrathin section libraries with WaferMapper: a multi-scale approach to EM reconstruction of neural circuits”. *Frontiers in neural circuits* 8 (2014), p. 68.
- [54] Thomas Templier. “MagC, magnetic collection of ultrathin sections for volumetric correlative light and electron microscopy”. *Elife* 8 (2019), e45696.

# 4

## LABEL-FREE FLUORESCENCE PREDICTIONS FROM LARGE-SCALE CORRELATIVE LIGHT AND ELECTRON MICROSCOPY DATA

Electron microscopy (EM) provides high-resolution images of (sub-)cellular ultrastructure. Identifying particular organelles or proteins of interest from EM images alone, however, is often a challenge. Deep learning-based approaches have rapidly been adopted within biological EM to perform structural recognition tasks, such as organelle segmentation, due to their strength in pattern inference and analyzing visual imagery. Such approaches require large training datasets, typically at the expense of hundreds of hours of human annotation. As an alternative means of providing biological labels to EM datasets, we developed CLEMnet, a deep convolutional neural network that has been trained on large-scale (~16 GB) correlative light and electron microscopy (CLEM) data. These datasets have been compiled via integrated array tomography such that manual annotation is not required for generating predictions. CLEMnet predictions generated on EM images unseen by the network are highly correlated with the measured fluorescence signal. As the biological labels generated by the network are localized to specific cellular features and organelles, we additionally assess the feasibility of the correlative fluorescence data and network-generated predictions as training masks for organelle segmentation. We find that while segmentation models trained on these masks significantly underperform those trained on masks made by hand, overall segmentation performance can be greatly improved by minimal human annotation.

---

This chapter is in preparation for a manuscript to be submitted for publication: Ryan Lane et al. “Label-free fluorescence predictions from large-scale correlative light and electron microscopy data”. *In Preparation* (2022).

## 4.1. Introduction

Electron microscopy (EM) has transformed the way in which biologists understand intra- and inter-cellular systems. Due to the lack of inherent biological specificity, however, interpretation of EM datasets typically requires tedious expert analysis and annotation. For this reason, fluorescence microscopy (FM) is often used in conjunction with EM, complementing structural data with targeted biological labels. Fluorescent labelling, however, comes with several drawbacks. Sample preparation protocols are often laborious, time-consuming, and potentially damaging to the sample [2]. Protocols must also be adapted to limit concentrations of heavy metal staining if intermediate processing of the sample is to be avoided [3, 4]. Fluorescent labelling is also susceptible to bleedthrough when multiple fluorophores are expressed in a single sample as well as varying specificity—Hoechst dyes, for instance, bind to both DNA and RNA. Furthermore, registering the separate imaging modalities across large spatial extents remains a technically challenging and primarily manual task [5, 6, 7]. Correlative fluorescence and electron microscopy experiments are therefore typically limited in scope to the micron or tens of microns scale, and thus so are the regions for which biological labels can be provided [8, 7].

As recognition of organelles and other subcellular structures remains a pivotal obstacle in biological EM, we questioned whether large-scale EM datasets [9, 10] could be supplemented with biological labels through alternate means. To address this question, we sought to leverage recent advances in deep learning. Deep convolutional neural networks (CNN) in particular have been shown to be capable of inferring complex, non-linear relationships from image data [11, 12]. Prior work involving deep CNNs in the context of electron microscopy data has primarily been limited to applications in segmentation, denoising, and compressed sensing [13]. Semantic segmentation, the classification of pixels into discrete categories, does ultimately serve the purpose of adding biological labels to EM data. However, modern deep learning approaches require hours of tedious expert segmentation [14, 15, 16, 17, 18, 19]. In order to perform whole-cell organelle segmentation, for instance,  $28 \mu\text{m}^3$  of training data was manually segmented; each cubic micron block required one person two weeks of manual segmentation [20].

Although relatively little attention has been paid to alternative applications in deep learning for EM data, recent work has focused on generating biological labels from other imaging modalities. Christiansen et al. [2] designed a deep neural network to predict fluorescence labels from transmitted light images. Ounkomol et al. [21] extended the technique to generate 3D fluorescence from stacks of transmitted light microscopy data and further demonstrated the possibility of predicting immunofluorescence from EM images in order to facilitate automatic registration of fluorescence data with EM. Seifert et al. [22] similarly developed a CNN for registering correlative datasets, releasing it as a FIJI plugin. To address the challenge of adding biological specificity to large-scale EM datasets, we thus explored the potential for a CNN to make label-free fluorescence predictions from electron microscopy image data.

In this work we present a deep CNN, CLEMnet, for generating fluorescence predictions on large-scale EM data of tissue and cellular samples. We demonstrate the performance of our model on thin sections of rat pancreas tissue, which have been immunolabelled with Alexa Fluor 594 and given a Hoechst counterstain, as well as Hoechst-stained sections of resin-embedded mouse breast tumor cells. Network predictions are quantitatively evaluated against corresponding true fluorescence images based on the Pearson correlation coefficient (PCC, or  $\rho$ ) as well as by assessing human recognition of fluorescence predictions on cell nuclei. We additionally assess the network's robustness by measuring its predictive power on EM datasets acquired with a diverse range of imaging parameters. Finally, we explore the potential of correlative and predicted fluorescence signals for use as labels in segmentation experiments.

## 4.2. Results

### 4.2.1. Network overview

To train a CNN to predict the fluorescence signal from EM images, we create training datasets comprised of high-magnification EM and FM image pairs. The FM images are acquired by a fluorescence microscope integrated into the chamber of a scanning electron microscope (SEM) [23, 24]. This experimental setup allows for high accuracy overlay precision without a reliance on fiducial markers or manual input [25]. This is advantageous as it prevents the network from learning on extrinsic markers or bias in the image registration. It further allows for the semi-automated accumulation of correlative datasets, scalable to several GBs [4].

To optimize performance for GPU clusters, the large-scale correlated datasets are divided into small tiles which serve as input for the model (Figure 3.S1A). Image tiles are shuffled to diversify the training area, reducing the likelihood of overfitting to a particular region of the specimen. A deep CNN was chosen for the model architecture for its strength in recognizing structural detail in EM images as well as for its superhuman pattern recognition capabilities [26]. To address the resolution mismatch between EM-FM image pairs, the model is designed with more contraction than expansion paths, which results in an elongated, backwards “J”-shape as opposed to the more typical “U” (Figure 3.S1B). Once trained, the model is able to generate predictions of the fluorescence intensity on individual EM image tiles. Separate correlative EM-FM datasets are set aside for validating and testing the model. By stitching together the model’s output it is possible to render large-scale predictions of the fluorescence intensity, which can then be overlaid onto the EM test dataset (Figure 3.S1C).

### 4.2.2. Network predictions on thin tissue sections

To characterize the performance of our network, we first apply it to routinely prepared ultrathin sections of rat pancreas tissue [27]. The sections are stained with Hoechst, targeting cell nuclei, and immunolabelled with AF594, targeting insulin granules. The prediction (green) is found to correlate well with the measured fluo-

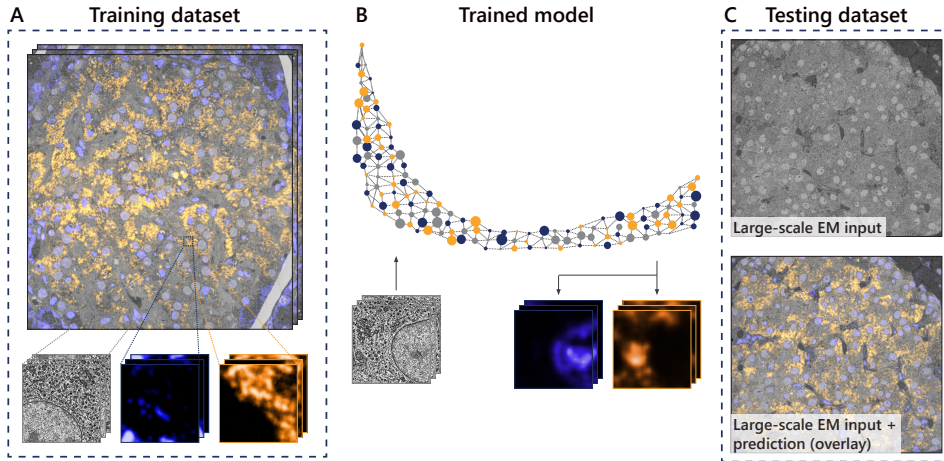


**Figure 3.S1.** Procedure for fluorescence intensity predictions. (A) Training data for the model consists of registered, large-scale CLEM datasets. For the rat pancreas tissue shown here, the fluorescent channels consist of a Hoechst stain (blue), targeting cell nuclei, and AF594 (orange), targeting insulin granules. (B) The correlative image data is input to an asymmetric convolutional neural network which maps EM to FM. The model is illustrated as a backwards “J” due to the resolution mismatch between EM and FM. (C) Once trained, the network generates predictions on EM test data such that the predictions can be overlaid to amass large-scale, artificial CLEM datasets.

rescence (red); PCCs of 0.67 for Hoechst (Figure 3.S2A) and 0.76 for AF594 (Figure 3.S2F) are computed when averaged across an entire islet of Langerhans. At high magnification, the measured and predicted intensities for Hoechst are found to exhibit a close qualitative resemblance ( $\rho = 0.73$ ; Figure 3.S2B–E). Notably, both signals are more heavily concentrated along the nuclear envelope and areas of denser chromatin within the nucleus. The predicted AF594 signal matches well with that of the measured fluorescence ( $\rho = 0.73$ ; Figure 3.S2H–J) with the caveat that the predicted intensity appears to spread out more uniformly over adjacent insulin granules—possibly due to the granules being diffraction-limited.

There are other factors that may contribute to a diminished PCC that are extraneous to the network. These include bleedthrough of one fluorescence channel into another (Figure S1B), errors in the EM-FM registration (Figure S1C), and aberrations in the fluorescence microscope (Figure S1D). Not only do these cases warrant a reduced correlation coefficient, but they demonstrate the network’s ability to effectively correct for imperfections in the measured fluorescence.

#### 4.2.3. Human evaluation of fluorescence vs label-free prediction

To further characterize the performance of the model, we assess human recognition of cell nuclei in the network-generated predictions versus the measured fluorescence (Figure 3.S3). In order to quantify recognition proficiency, we establish a

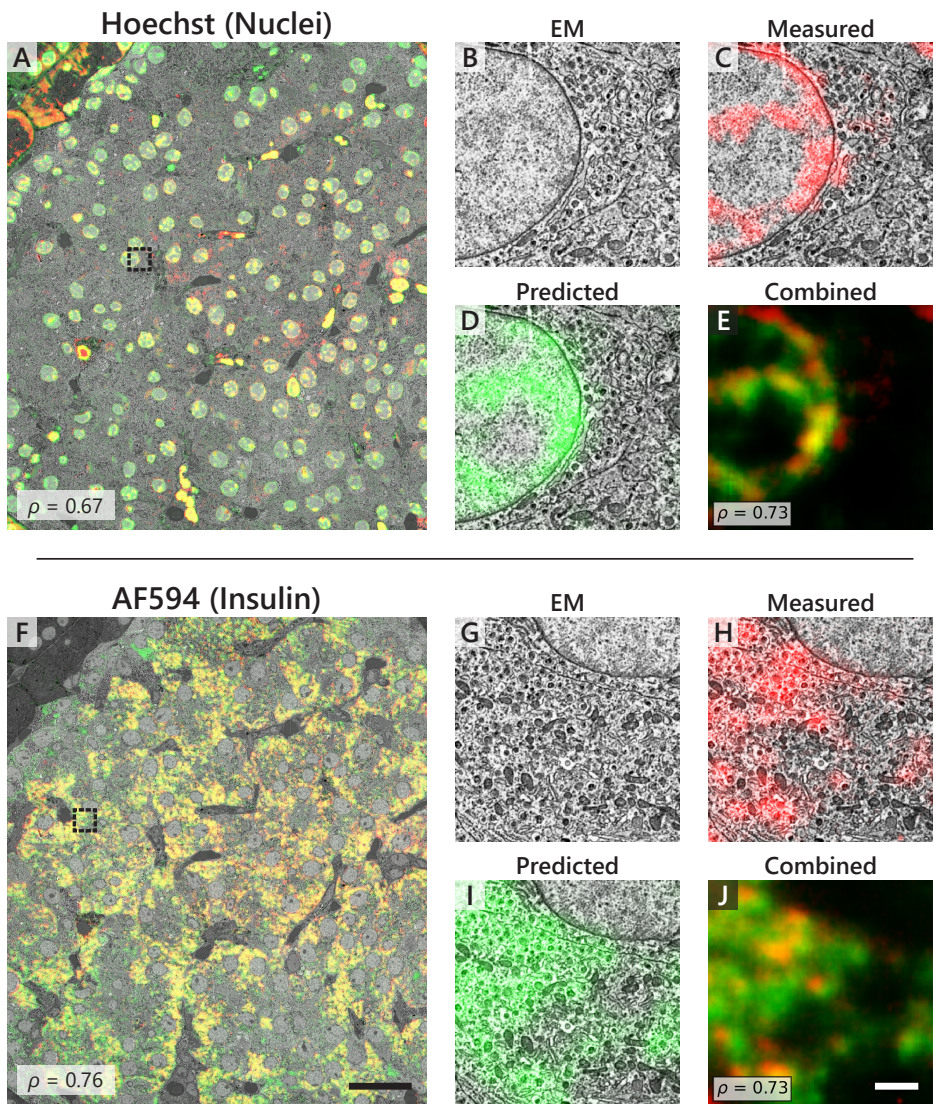


**Figure 3.S2.** Network predictions of the fluorescence intensity correlate well with the measured fluorescence signal. (A) The measured (red) and predicted (green) fluorescence for a nucleus marker overlaid onto a large-scale EM dataset of an islet of Langerhans. Regions of high correlation appear as yellow. Zoomed insets show the EM (B); measured (C), predicted (D), and combined (E) fluorescence for an individual cell nucleus. (F) Same as in (A) but for AF594 targeting insulin granules. (G – J) Same as in (B – E) but for a cluster of insulin granules. Scale bars: (A, F) 20  $\mu\text{m}$ ; (B – E, G – J) 1  $\mu\text{m}$ .

ground truth (GT) set of cell nuclei based on EM (Figure 3.S3A). Approximately 200 cell nuclei were manually annotated by a combination of experts and trained volunteers. Spurious annotations were filtered out using unsupervised, brute-force nearest neighbors.  $k$ -means clustering was then used to partition the remaining annotations into point clouds from which the centroids were computed and added to the GT.

The experts and trained volunteers were then asked to recognize cell nuclei in the measured and predicted fluorescence datasets (Figure 3.S3B–C). Nuclei are considered to be correctly identified (true positive, TP) when they are detected within a certain threshold distance—approximately the average radius of a nucleus—from a nucleus in the GT. Incorrectly identified nuclei (points for which there is no nearby nucleus) are considered to be false positives (FP), while those that are missed entirely are considered to be false negatives (FN).

The precision, recall, and Sørensen–Dice index (F1 score) are calculated for each of the expert and trained volunteer annotation sets (Figure 3.S3C). Similar average precision scores for the measured and predicted fluorescence (72% vs 74%) suggest that a comparable number of false positives were identified in both, while the notably higher recall for the predicted dataset (80% vs 58%) indicates that a substantially higher number of cell nuclei become recognizable from the predicted signal. This is visibly apparent throughout the dataset (Figure 3.S3B–C insets), but is particularly noticeable in the periphery where the fluorescence is marginally weaker due to non-uniform illumination and nuclei become obscured due to Hoechst expression from RNA in the endoplasmic reticulum. The F1 scores (76% predicted vs 64% measured) reveal the improved recognition ability afforded by the network-generated predictions. The same assessment cannot be done for insulin granules as the typical size is  $\sim$ 100 nm—well below the diffraction limit.

#### 4.2.4. Network robustness

We evaluated the network’s ability to make fluorescence predictions from EM data acquired with different imaging settings. To address this question, we first acquired CLEM data from serial sections of Hoechst-stained mouse breast tumor cells embedded in lowicryl HM20. Ten regions from three different sections were acquired with the same imaging settings to establish a baseline set of imaging parameters for the training data (Section 4.4.3). The training dataset was supplemented with CLEM data from the rat pancreas endocrine tissue (Hoechst channel only), which was also acquired with the same baseline settings. Individual imaging parameters were then adjusted for subsequent CLEM acquisitions of additional regions of tumor cells (Table 4.1). Section S006B, for instance, was acquired with a decreased landing energy (1000 eV versus 1500 eV baseline). Various types of data augmentation including elastic deformation, affine transformations, brightness/contrast adjustment, and noise augmentation were applied during training to improve the model’s robustness (Section 4.4.4).

Fluorescence intensity predictions were made on 1  $\mu$ s EM data in order to assess the network’s ability to generate predictions on lower signal-to-noise ratio (SNR) images (Figure 3.S4A<sub>I</sub>–IV). The prediction shows good qualitative agreement with

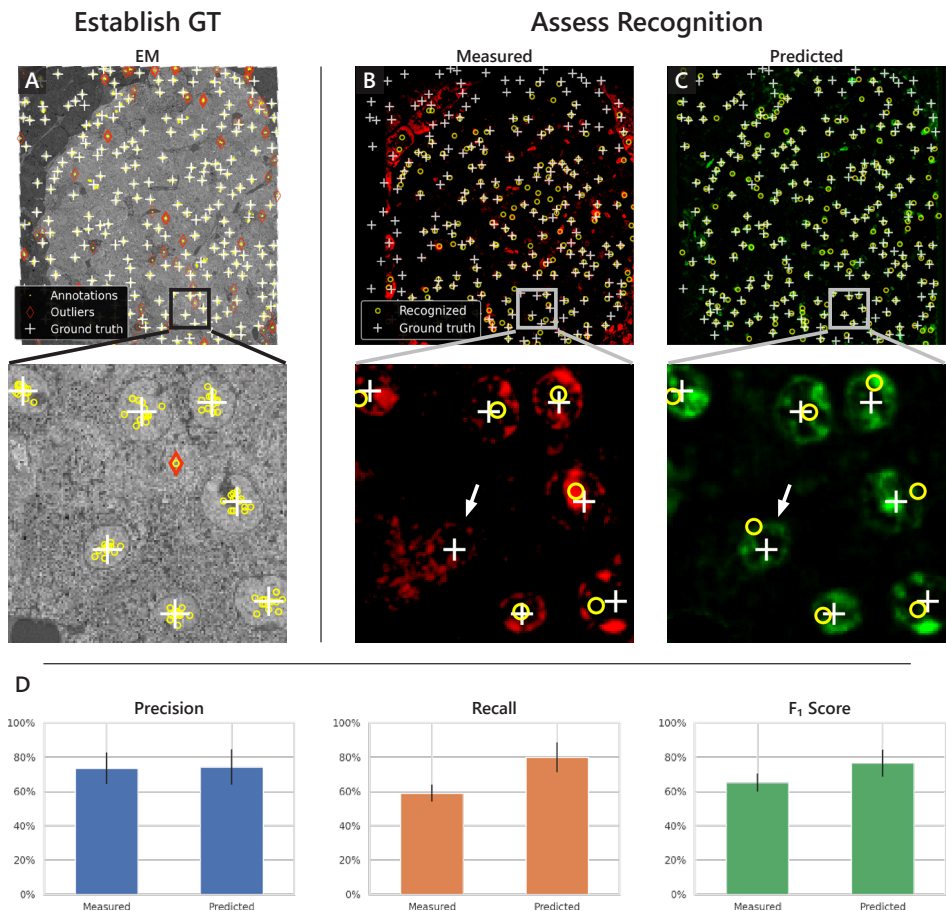


**Figure 3.S3.** Network-generated predictions facilitate human recognition of cell nuclei. (A) Annotations (yellow circles) of EM data are aggregated to establish a ground truth set of cell nuclei. GT nuclei (white crosses) are those that were chosen by a supermajority of annotators, while outliers (red diamonds) were discarded. Cell nuclei recognized by an individual annotator in the measured fluorescence (B) and network-generated prediction (C) are measured against the GT nuclei. A yellow circle marks where the annotator has identified a nucleus. Correctly identified nuclei (TP) are therefore denoted by an (approximately) overlapping white cross and yellow circle, while FPs and FNs are denoted by solitary yellow circles and white crosses, respectively. The white arrows indicate an instance of a cell nucleus that went unrecognized in the measured fluorescence (FN), but was identified in the prediction (TP). (D) Mean scores for the precision, recall, and F1 score are calculated by aggregating the TPs, FPs, and FNs across 15 sets of annotations.

the measured fluorescence, suggesting the model is moderately robust to noise. The prediction is furthermore localized only to the cell nucleus in spite of the moderate streak pattern through the EM, an artefact of sectioning. The relatively poor

PCC (0.23) is due in large part to autofluorescence of the resin, which is strongly anti-correlated with the predicted fluorescence intensity (apparent in Figure 3.S4A<sub>IV</sub>). We find that autofluorescence is more pronounced in cell samples as there is more bare resin between cells than in tissue.

The network is also capable of predicting cell nuclei on EM images acquired with a larger pixel size (Figure 3.S4B<sub>I-IV</sub>), demonstrating some degree of scale invariance. The relatively low PCC (0.49) is again negatively affected by autofluorescence in the measured fluorescence image. Predictions on EM images with a reduced landing energy (1 keV as opposed to 1.5 keV baseline) demonstrate high qualitative and quantitative agreement with the measured fluorescence (Figure 3.S4C<sub>I-IV</sub>). It is unknown why autofluorescence was less prevalent at this region of the section. We note that we encountered one instance in which the network was deceived by a ring-like structure for which no Hoechst fluorescence was measured (Figure 3.S4C<sub>II-III</sub>, insets), but which the network may have incorrectly recognized as a chromatin-rich nuclear region.

#### 4.2.5. Weakly supervised, semi-automated segmentation

We next assessed whether the correlative data, either measured fluorescence or label-free CLEMnet predictions, could facilitate segmentation of targeted organelles. To this end, we deployed an instance of ResNet-34 [11] to perform organelle segmentation. Typically, ResNet-34 is trained with labelled images obtained by manually segmenting hundreds if not thousands of EM images by hand. While shown to be highly effective, this method is also extremely time consuming [28, 12, 19, 29, 30]. To expedite the process for generating labelled image data, we evaluated three different approaches (Figure 3.S5): (i) simple thresholding of the correlative images to generate segmentation masks for training, (ii) equivalent thresholding but then on CLEMnet predictions, and (iii) a combination of partial points annotation with  $k$ -means clustering and Voronoi partitioning. These approaches classify pixels as either nucleus, background, or, in the case of (iii), initially unclassified.

We anticipated that the first approach would result in a significant amount of incorrect labels due to the issues mentioned previously (nonspecific labelling, EM-FM registration errors, autofluorescence, etc.). However, because the incorrect labels would be uncorrelated (in the case of EM-FM registration errors) or on featureless areas of the EM (in the case of autofluorescence), we suspected that the model could disregard them to the same extent as was found for the fluorescence predictions (Figure S1). The more fundamental problem with this simple approach is that the fluorescence signal may not be uniformly distributed throughout an organelle. In cell nuclei, for example, the fluorescence from the Hoechst staining is localized to the nuclear envelope and chromatin-dense subregions. The result from training ResNet-34 on these masks is hence a fragmented segmentation that largely resembles the measured fluorescence itself (Figure 3.S6A, “Measured FM Masks”)—nuclei are segmented with high-precision (low FPs), but portions of many nuclei are missed (high FNs). This is in contrast to the segmentation results from the traditional approach of training the network on manually segmented nuclei (Figure 3.S6A, “GT Masks”).

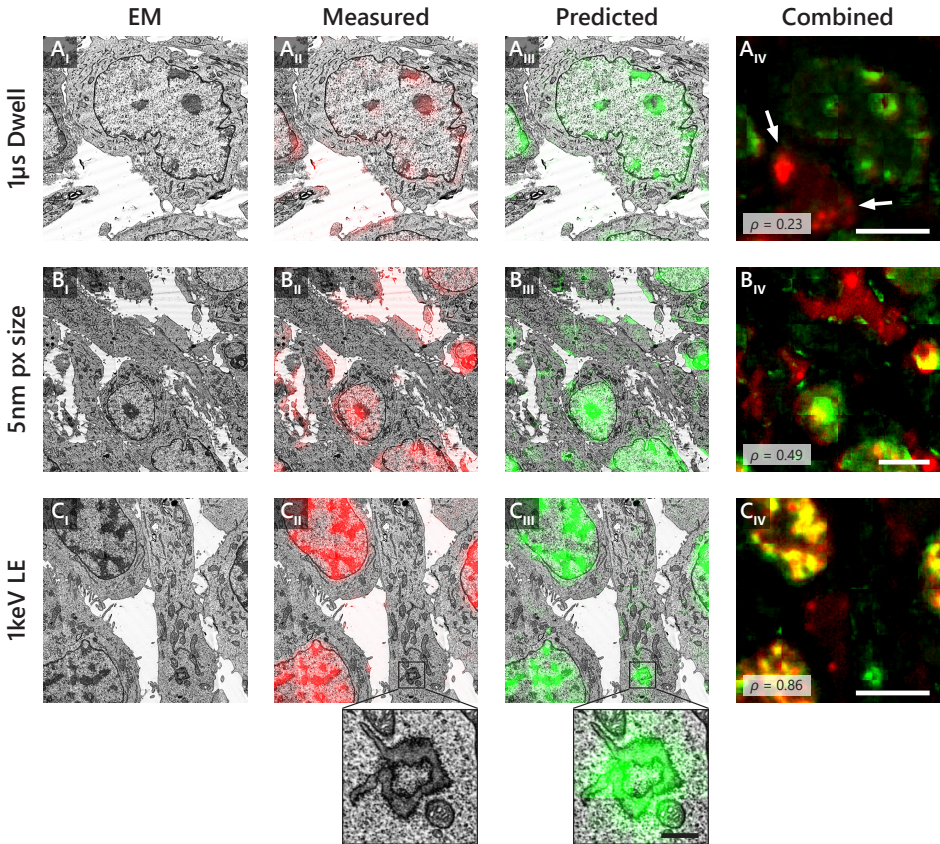


**Figure 3.S4.** Fluorescence predictions are robust to lower SNR EM images as well as those acquired with different imaging settings. Predictions were generated on resin-embedded mouse breast tumor cells acquired with varying EM imaging parameters. (A<sub>I</sub>) EM of tumor cell with reduced SNR by lowering the dwell time from 2  $\mu$ s to 1  $\mu$ s. (A<sub>II</sub>-III) Measured fluorescence and prediction overlaid onto (A<sub>I</sub>). (A<sub>IV</sub>) Combined measured fluorescence (red) and prediction (green) with white arrows indicating a high quantity of autofluorescence, nullifying the PCC (0.23). (B<sub>I</sub>-IV) Same as in (A<sub>I</sub>-IV) but for EM acquired with a larger pixel size (5 nm vs 4 nm baseline). (B<sub>III</sub>) The network generates several instances of spurious fluorescence predictions, while autofluorescence of the resin is again found to impede the PCC (0.49). (C<sub>I</sub>-IV) Same as in (A<sub>I</sub>-IV) but for EM acquired with reduced landing energy (1 keV vs 1.5 keV baseline). High correlation ( $\rho=0.86$ ) is found between the measured and predicted fluorescence aside from an unknown structure (insets). Scale bars: (A - C) 5  $\mu$ m; (C<sub>II</sub>-III, insets) 0.5  $\mu$ m.

As CLEMnet was found to predict fluorescence more uniformly throughout the nucleus, we assessed whether generating labelled images by thresholding the CLEMnet predicted data would improve results. The segmentation results (Figure 3.S6A, “Prediction Masks”), however, were comparable to those that derived from thresh-

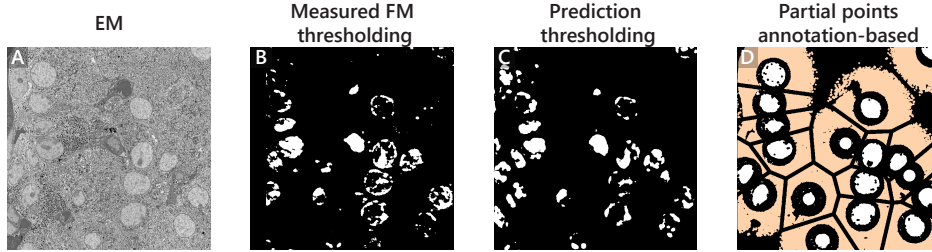


**Figure 3.S5.** Segmentation masks employed for CNN-based nuclei segmentation. (A) (Unlabelled) EM image of cell nuclei. (B) Labelled image (segmentation mask) derived from thresholding the correlative image of the measured fluorescence and (C) from thresholding the CLEMnet prediction from (A). (D) Segmentation mask derived from a combination of  $k$ -means clustering and Voronoi partitioning of the corresponding EM image. The points used in the Voronoi partition are the centroids of detected nuclei based on partial points annotation. Labelling scheme in (B – D): white – nucleus; black – background; beige – unlabelled.

olding the measured fluorescence data. While some nuclei are flood-filled, reflecting a successful segmentation, these occurrences are highly inconsistent. The intersection over union (IoU) results underscore the vast difference in segmentation performance. IoU scores for ResNet-34 trained on manually segmented nuclei average 89%, while those for ResNet-34 trained on thresholding the measured fluorescence and CLEMnet predicted signal are 44% and 43% respectively (Figure 3.S6C).

A more sophisticated approach for generating labelled images was therefore adapted from an approach by Qu et al. [31] who used partial points annotation to segment cell nuclei from histology images in a weakly supervised fashion. Compared to conventional hand-tracing of organelles, partial point annotation requires only a single point to be selected from a sample of organelles within each image. It thereby constitutes the annotation method requiring the least amount of manual time and effort, while still providing human-assisted supervision. Partial points annotation is particularly advantageous for correlative datasets as the fluorescence overlay facilitates organelle selection by the human annotator. We then trained ResNet-34 on segmentation masks derived from partial points annotations (Figure 3.S5D) as described in Section 4.4.6. The resulting segmentation performance (Figure 3.S6A, “Partial Points Masks”) improved upon the thresholding approaches with an average IoU score of 72%, despite the presence of some false positives/negatives (white arrows). While filtering segments by area would remove the vast majority of these false positives, smaller nuclei—those that were sectioned at the periphery—would also be removed.

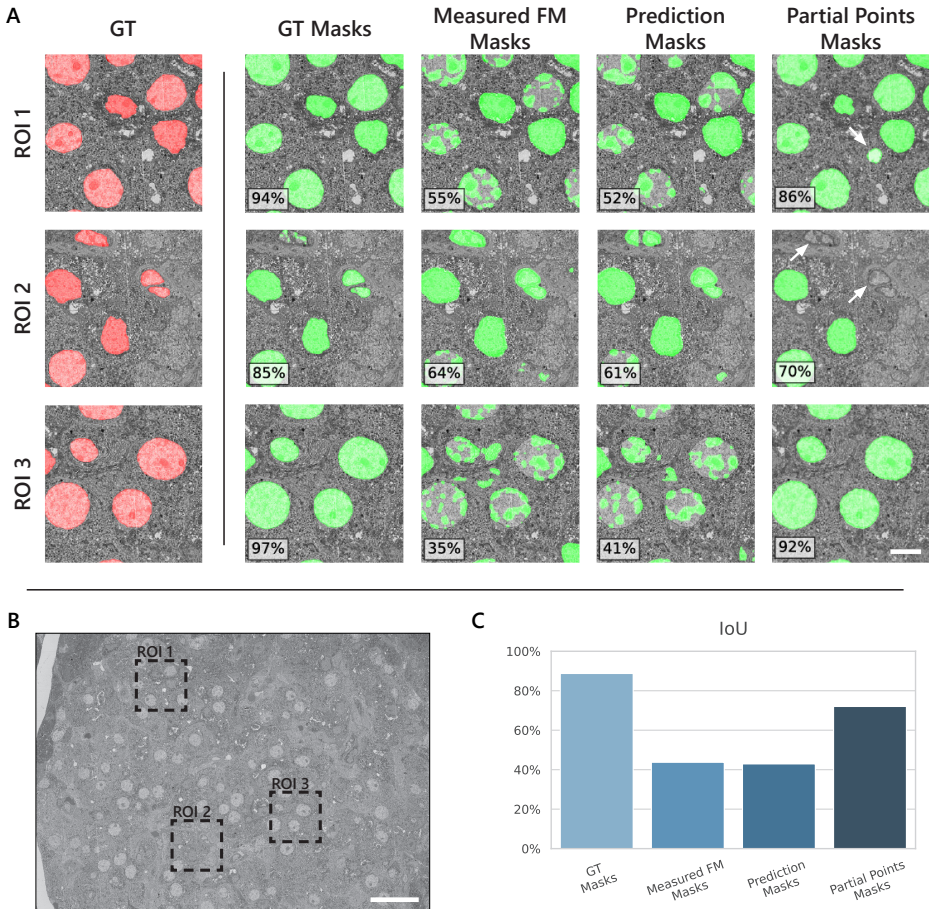


**Figure 3.S6.** CNN-based segmentation results for various labelling strategies: semi-automated labelling strategy outperforms thresholding approaches. (A) Three randomly selected regions of interest are selected from a large-scale EM dataset of rat pancreas tissue (B) to assess segmentation performance. Intersection-over-union (IoU) scores are provided in the corner of each ROI. CNN architecture for all segmentation results is based on ResNet-34. White arrows denote instances of falsely labelled nuclei. (C) Aggregate IoU scores of the four segmentation strategies across the entire section. Training on semi-automatically generated segmentation masks derived from partial points annotation together with  $k$ -means clustering and Voronoi partitioning results in improved segmentation performance. Scale bars: (A) 2  $\mu$ m; (B) 10  $\mu$ m.

### 4.3. Discussion

We have demonstrated the ability of a CNN to artificially predict biological labels in electron microscopy images based on registered CLEM training data. This has

important ramifications for many areas within cell biology in which additional labelling techniques are implemented to facilitate recognition of structures in EM [8]. In order to generate label predictions, registered EM-FM image pairs are required to train the CNN. Although in this work the accumulation of correlative datasets was facilitated by integrated CLEM, this is not a pre-requisite. Sequential CLEM methods in which light and electron microscopy are performed by different instruments in succession may also be suitable. It is unknown, however, what effects might come about from the use of fiducial markers and potentially less precise image registration across large fields of view.

While label predictions are not generalizable to arbitrary organelles outside of the training dataset, we have shown that the network is capable of transfer learning across cell types. Predictions on mouse breast tumor cell nuclei were made after supplementing a training dataset comprised primarily of rat pancreas tissue with a limited amount of correlative data from tumor cells. Aided by data augmentation, label predictions were furthermore found to be robust to changes in EM imaging parameters, additional shot noise, and sectioning artefacts. By further supplementing existing correlative datasets with data from different organisms, cell types, and microscopes, robustness could be improved even further.

The measured fluorescence and CLEMnet predicted labels fall short of providing adequate templates for fully automated segmentation. Nevertheless, we have shown that fluorescence labels are not only capable of facilitating annotation, but that as part of an image processing pipeline, they enable a framework for semi-automatic, weakly supervised segmentation. It is difficult to imagine that a deep CNN trained on automatically generated segmentation masks (i.e. no manual annotation whatsoever) could outperform the same network when trained on manually generated segmentation masks in the near future [32, 12, 33]. Even so, semi-automated and fully automated approaches may still fulfill a role in segmenting biological image data. For smaller-scale applications in which training datasets are still tractable, a segmentation model based on manually segmented organelles is likely the more sensible approach. But for large-scale or volume applications in which a pixel-perfect segmentation may not be strictly necessary, a semi-automated labelling approach may offer valuable time-savings at the cost of precision.

The deep CNN developed here offers a means to do fluorescence-like labelling of electron microscopy data at negligible cost with respect to time, effort, and money. Once the network has been sufficiently trained, label predictions can be automatically generated in seconds. This would allow research facilities to process only a handful of sections for correlative fluorescence and electron microscopy, while preparing the rest of the sample for EM only. The entire EM volume could then be overlaid with fluorescence-like labels after training on the portion of the volume set aside for correlative imaging. In addition, EM datasets could be labelled with a larger number of distinct labels than would be allowed in a single fluorescence experiment by simply labelling different targets in different subsets of the sample. Alternatively, it would enable comparative studies of multiple samples imaged by EM (e.g. [34, 9]) to be given biological labels virtually for free, providing biological insight to a wealth of grayscale data.

## 4.4. Methods

### 4.4.1. Tissue and sample preparation

#### Rat pancreas

Fresh pancreas from an 83 day old rat was cut into small pieces and fixed in 4% paraformaldehyde (PFA, Merck) + 0.1% glutaraldehyde (GA; Polysciences) as described in Ravelli et al. [27]. The sample was post-fixed in 1% osmium tetroxide and 1.5% potassium ferrocyanide in 0.1 M cacodylate buffer, dehydrated through ethanol series and embedded in EPON (Serva). 100 nm sections were cut and placed onto ITO-coated glass coverslips (Optics Balzers). Immunolabeling was performed as described previously [3]. Samples were etched with 0.1% periodic acid for 10 min, followed by a 30 min blocking step: 1% bovine serum albumin (BSA; Sanquin, Netherlands) in tris-buffered saline (TBS), pH 7.4. Next, anti-insulin was incubated for 2 hr (guinea pig; 1:50, Invitrogen, PA1-26938, RRID: AB\_794668) followed by washing and subsequent incubation for 1 hr with biotinylated secondary antibody (donkey-anti-guinea pig; 1:400, Jackson Immunoresearch) followed by washing steps. Finally, streptavidin conjugated AF594 (1:100, Jackson Immunoresearch) were incubated for 1 hr followed by washing a 10 min incubation with Hoechst and washing.

#### Mouse breast tumor cells

Mice were fixed by vascular perfusion with 4% formaldehyde (FA) in 0.1 M phosphate buffer (1.5 mL/min) for ~5 min until organs and eyes are clearly discolored. Tumors were dissected and cut immediately in blocks (~1 mm<sup>3</sup>) in 4% FA fixative at room temperature. 4% FA immersion fixation for 3 hr at room temp was continued with 2% PFA + 2.5% GA immersion fixation for 2 hr at room temperature, and the samples were stored in glass vials with 4% FA until further processed. Samples were postfixed with 1% osmium tetroxide and 1.5% potassium ferrocyanide in 0.065 M phosphate buffer for 2 hr at 4 °C and finally for 1 hr with 0.5% uranyl acetate. Dehydration was performed using a graded ethanol series. Samples were embedded in EPON resin (EMbed 812, EMS) and polymerized for 48–60 hr at 65 °C. Ultrathin section of 100 nm were cut using a microtome (Leica, UC6) and placed on ITO glass. Hoechst 33258 (Sigma) staining was performed for 120 min followed by a washing step with MilliQ water, and air dried.

### 4.4.2. CLEMnet architecture

The design of CLEMnet (Figure 3.S7) is based on U-net [35], a deep CNN comprised of convolution, pooling, upsampling, and concatenation layers, designed for biomedical image segmentation. The U-net architecture was modified in several ways to make it more suitable for fluorescence predictions. The number of upsampling layers was reduced to address the resolution mismatch between EM and FM images. Additionally, the padding of images within convolution layers was removed to preserve image dimensions. Lastly, the number of convolution layers between each downsampling layer was reduced from two to one—roughly halv-

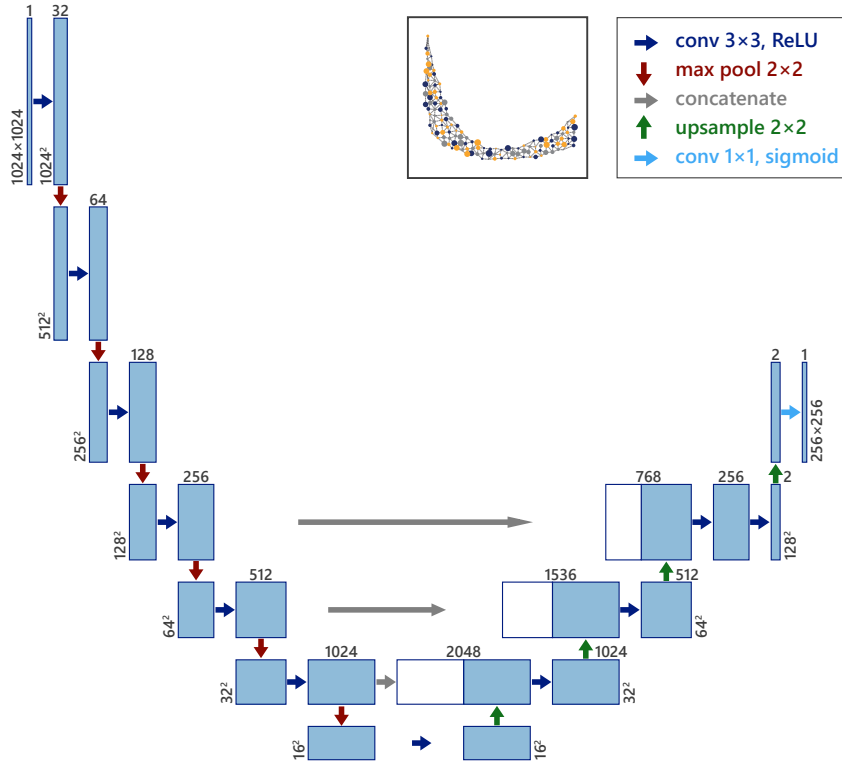


**Figure 3.S7.** CLEMnet architecture. The blue boxes correspond to multi-channel feature maps with the number of channels and image dimensions annotated above and to the side of each box, respectively. Arrows represent different possible operations as described in the legend. The asymmetric layout underlies the illustration from Figure 3.S1B.

ing the number of parameters—to prevent overfitting [36]. The model architecture was developed in Tensorflow [37], an open source library for implementing machine learning models in Python, using the Keras API [38]. All training and testing procedures were performed on NVIDIA Tesla P100 PCIe 12 GB GPU cards.

#### 4.4.3. Data acquisition

The integrated microscopy workflow for large-scale correlative imaging and reconstruction is described in Lane et al. [39]. Briefly, fluorescence imaging is done via the Delmic SECOM (Delmic B.V.), which has been retrofitted into the vacuum chamber of a Verios 460 SEM (Thermo Fisher Scientific) [23, 24]. Correlative FM and

low-magnification EM image tiles are acquired in a grid-like pattern encompassing each tissue section. The fluorescence is captured prior to EM to avoid quenching of the fluorescence. Following the acquisition of each correlative image pair, the FM tile is registered to the low-magnification EM tile by means of cathodoluminescent markers [25]. The fluorescence signal is then used to guide to regions of interest for subsequent, high-magnification EM, such as the islet of Langerhans in the case of the rat pancreas tissue. As thin sections of the mouse breast tumor cells are more or less homogeneous, acquisition areas were chosen based on minimal damage to the section.

Each FM tile consists of a 10 s exposure at 405 nm excitation for Hoechst and 555 nm excitation for AF594. The corresponding low-magnification EM tiles are acquired at 1.5 keV landing energy with a 1 kV bias potential, as described in Lane et al. [4], with a 400 pA primary beam current, 5  $\mu$ s dwell, and 150  $\mu$ m field width. The baseline imaging parameters for high magnification EM are the same as those for low-magnification EM with the exception of a 2  $\mu$ s dwell and 12  $\mu$ m field width ( $\sim$ 3 nm pixel size). Imaging parameters for the datasets of mouse breast tumor cells acquired to assess network robustness are provided in Table 4.1. All of the image data used in this work is publicly available.<sup>1</sup> Visualization and navigation of the large-scale datasets is made possible by CATMAID [40].

Z	Section ID	LE (eV)	Dwell ( $\mu$ s)	Pixelsize (nm)	N. EM images	Area ( $\mu$ m $\times$ $\mu$ m)	Time (hr)
10-19	S007A-S009C	1500	2	3	484	234 $\times$ 234	4.5
0	S002A	1500	3	3	484	234 $\times$ 234	6.8
1	S003B	1500	1	3	484	234 $\times$ 234	2.3
2	S003C	1500	2	3	484	234 $\times$ 234	4.5
3	S003D	1500	2	4	289	241 $\times$ 241	2.7
4	S004A	1500	2	5	196	249 $\times$ 249	1.8
5	S004B	1500	2	6	121	235 $\times$ 235	1.1
6	S005A	1500	5	3	484	234 $\times$ 234	11.3
7	S005B	2000	2	3	484	234 $\times$ 234	4.5
8	S006A	1000	2	3	484	234 $\times$ 234	4.5
9	S006B	3000	2	3	484	234 $\times$ 234	4.5

**Table 4.1.** Electron microscopy imaging settings used for the acquisition of resin-embedded mouse breast tumor cells. For data navigation purposes, Z index corresponds to section index within CATMAID.

#### 4.4.4. Robustness & validation

EM and FM image pairs are augmented during training to increase the robustness of the model. The objective is to improve the model's flexibility and to account for different types of imaging conditions rather than to extend it to different specimens. While the model may generate reasonable predictions of the fluorescence

<sup>1</sup><https://sonic.tnw.tudelft.nl/catmaid/>

intensity on the same cell type or organelle across different specimens, it is not generalizable to tissue or cell types it has not been trained on. Several different types of data augmentation are applied to account for the variety of imaging settings the network would reasonably encounter if tested on EM data from other instruments.

### Affine transformation

Affine transformations are applied to training data such that the model learns to adapt to modest changes in structural topology. By introducing minor adjustments to the rotation ( $\theta$ ), translation ( $t_x, t_y$ ), scale ( $z_x, z_y$ ), and shear ( $\Gamma$ ) of the training data, some degree of invariance to these transformations is embedded into the model [41]. The applied affine transformations are randomized for each EM-FM image pair such that each image pair receives the exact same transformation (Figure 3.S8).

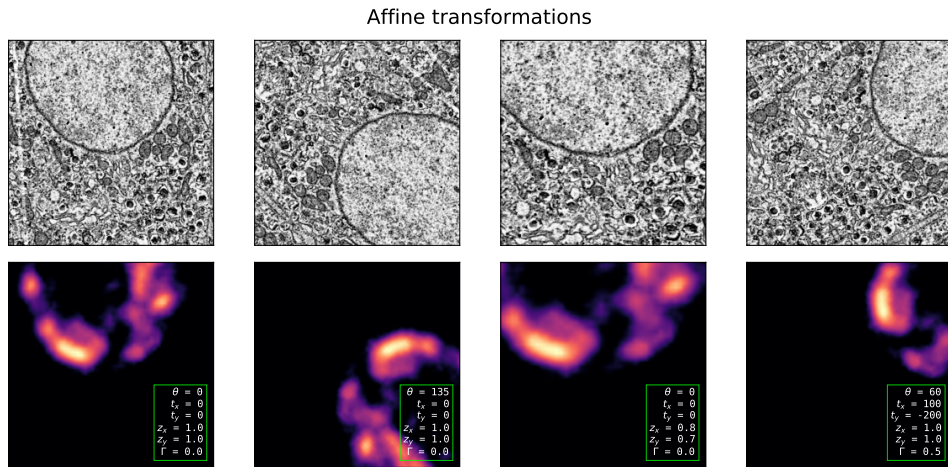


**Figure 3.S8.** Affine transformations are applied to the training data to render the model invariant to topological changes, resulting in greater robustness. The original, correlative image pair (left) may be rotated, translated, scaled, and sheared to encompass a wide variety of possible topological changes. Exact transformation parameters are provided in the text box of each transformed image pair.

### Elastic deformation

Elastic deformation was identified by Simard et al. [41] early in the development of neural networks as an effective means of augmenting training data. It was later shown by Dosovitskiy et al. [42] and reinforced by Ronneberger et al. [35] as a crucial tool for enhancing CNN training, particularly in the case of limited training samples. Elastic deformations are generated by applying a non-linear warp to the image where the warp is defined by a displacement field convolved with a Gaussian kernel of standard deviation,  $\sigma$ , and multiplied by a scaling factor,  $\alpha$  (Figure 3.S9,

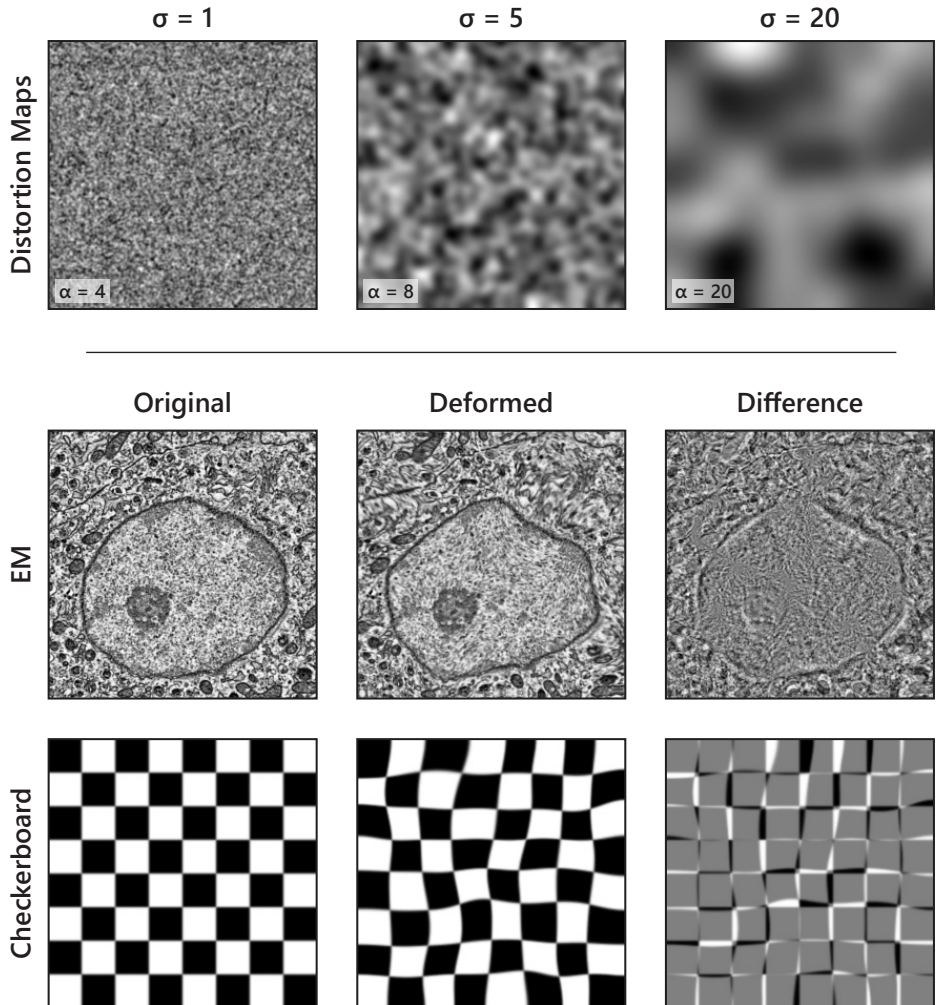


**Figure 3.S9.** Top: Distortion maps used for applying elastic deformations to training data. For small  $\sigma$  the deformation resembles the addition of white noise, while for large  $\sigma$  the deformation is more severe. Bottom: Elastic deformation applied to an EM training image and a checkerboard pattern.

top). The displacement field is initialized by a random uniform distribution where each pixel ranges from  $(-1, +1)$  with equal probability. The value for  $\alpha$  is also randomized such that the EM images are warped with varying intensity. Distortions are more apparent along the edges of features (Figure 3.S9, bottom).

## Brightness & contrast variation

To account for the expected variations to brightness and contrast in EM image data acquired across different samples, microscopes, imaging settings, (day of the week), etc. the brightness and contrast levels are given a random adjustment. The brightness is varied  $\pm 20\%$  by adding a gray-level bias, while the contrast is adjusted in the range ( $0.75 < \delta < 1.5$ ) where the value of each pixel,  $x$ , is scaled by

$$(x - \bar{x}) \delta + \bar{x} \quad (4.1)$$

where  $\bar{x}$  is the average intensity of the whole image.

## Noise augmentation

There are multiple sources of noise in the SEM detection chain, each with their own statistical distribution. The dominant source of noise on a properly operating SEM is, however, typically Poisson (shot noise) as additional contributions from the detector, scanning electronics, etc. tend to be much smaller than the statistical noise inherent in the signal [43]. Training images are therefore augmented with shot noise to improve the model's robustness with respect to low SNR images (Figure 3.S10). The probability that a random variable  $X$  is equal to  $k$  is given by

$$P(X = k; \lambda) = \frac{\lambda^k e^{-\lambda}}{k!} \quad (4.2)$$

where  $\lambda$  is the expectation value of  $X$  as well as its variance.

Poisson noise

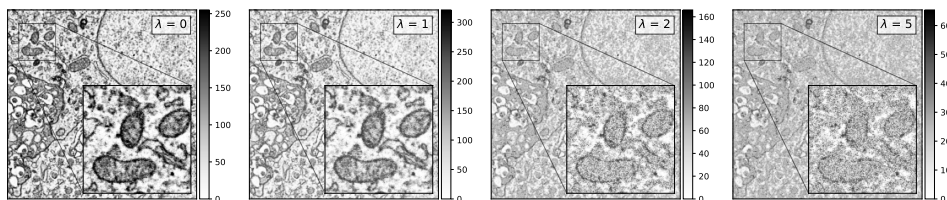


**Figure 3.S10.** Poisson noise added to an EM training image. Features become unrecognizable at high values of  $\lambda$ .

## 4.4.5. Quantitative analysis

### Cell nuclei counting

A combination of experts and trained volunteers were asked to recognize cell nuclei in datasets comprised of fluorescence signals obtained with a microscope and generated by CLEMnet. The experts consisted of two researchers from the University Medical Center Groningen who routinely examine islets of Langerhans, while the volunteers consisted of thirteen researchers from within the TU Delft Department of Imaging Physics who were trained to recognize cell nuclei in both FM and

EM image data from comparable tissue. The annotations made by the experts were weighted by a factor 3.

An unsupervised, brute-force nearest neighbors search was used to filter outlier annotations from the EM dataset. For each annotated point, the Euclidean distance to every other annotated point was calculated. If a point was found to have at least 12 neighboring points (corresponding to  $\geq 80\%$  of annotators) within a radius roughly equal to the average radius of a cell nucleus, the point was kept. Points with an insufficient amount of neighboring points were discarded, resulting in clusters of point clouds corresponding to the ground truth nuclei.  $k$ -means clustering was then used to agglomerate point clouds from which the centroid of each cluster could be computed and added to the ground truth set.

### Segmentation evaluation

Segmentation performance is evaluated by the intersection over union (IoU), a similarity coefficient used to measure the overlap of two sets  $A$  and  $B$ .

$$IoU(A, B) = \frac{|A \cap B|}{|A \cup B|} \quad (4.3)$$

### 4.4.6. Segmentation

#### Fully supervised segmentation

Segmentation masks for training were generated either by manually tracing cell nuclei in EM images of rat pancreas islets (using GIMP) or by thresholding the measured fluorescence or CLEMnet prediction images. A value of 0.2 was empirically chosen to be the threshold after rescaling the intensity range from (0, 255) to (0, 1). To reduce the burden on manual tracing, a higher zoom level was chosen than for generating fluorescence predictions. 96 images from across six different sections were manually segmented. One section was set aside for testing, while the five remaining sections were divided 80%/20% for training and validation. Implementation of the ResNet-34 model architecture was facilitated by Segmentation Models [44], which provides neural network frameworks for image segmentation compatible with Keras and Tensorflow.

#### Partial points annotation

Labelled images are generated in a two-phase process adapted from Qu et al. [31]. In the first phase (Figure 3.S11A), partial points annotation is used to generate a probability map for the location of cell nuclei. Partial points annotation was performed on the same dataset as used for the fully supervised segmentation. Though all nuclei visible in the EM were annotated, only five were chosen at random for generating Gaussian masks (PP Mask). The values for the Gaussian masks are given by

$$M_i = \begin{cases} \exp\left(-\frac{D_i^2}{2\sigma^2}\right) & \text{if } D_i < r_1, \\ 0 & \text{if } r_1 < D_i < r_2, \\ -1 & \text{otherwise} \end{cases} \quad (4.4)$$

where  $D_i$  is the radial distance from each pixel  $i$  to the nearest partial point,  $\sigma$  is the standard deviation of the Gaussian distribution over each partial point, and  $r_1$  and  $r_2$  are the typical nuclear radius (estimated from the validation dataset) and the outer radius of background labels, respectively. Here we have used  $r_1 = 5 \mu\text{m}$ ,  $r_2 = 2r_1$ , and  $\sigma = r_1/2$ . In this way each pixel is classified as either nucleus ( $> 0$ ), background (0), or remains unlabelled ( $-1$ ).

When trained on pairs of EM images and PP masks, ResNet-34 yields probability maps of predicted nuclei locations for given input EM test images. The initial probability map, though rather crude, is used to refine the PP mask to generate a better estimate of the background. The background estimate is updated according to the conditions

$$M_i^N = \begin{cases} M_i & \text{if } D_i < r_2, \\ 0 & \text{if } D_i > r_2 \quad \text{and} \quad p_i < 0.1, \\ -1 & \text{otherwise} \end{cases} \quad (4.5)$$

where  $p_i$  is the probability of that pixel belonging to the nucleus class after iteration  $N$ . The pipeline is designed in such a way to as to iteratively yield better and better probability maps. We find, however, that the maps tend to converge after  $N = 2$  for this particular dataset.

In phase two (Figure 3.S11B), segmentation masks are generated by a combination of  $k$ -means clustering and a Voronoi partitioning of the nuclei detected in phase one. These two labelling schemes are complementary to one another.  $k$ -means clustering preserves the spatial information in the EM image, providing the contour of the nuclei at the expense of having greater uncertainty, while the Voronoi partition provides accurate nuclei localization at the expense of underestimating the background label. The EM image is multiplied by the distance transform of the Voronoi diagram prior to  $k$ -means clustering to amplify nuclei. Clustering is then done with  $k = 3$ . We choose to subtract a value of 1 from the resulting image such that the background goes to  $-1$  (unlabelled). In this way the model does not train on regions of the image where a label cannot easily be inferred from either the  $k$ -means clustering or Voronoi partitioning. These regions are typically in the void between adjacent nuclei where it can be disadvantageous to make an assumption on whether a pixel belongs to the nucleus or background class, as it is possible that a nucleus was missed in phase one.

The fluorescence image is independently thresholded and intersected with the  $k$ -means clustered image. Small segments are removed via morphological opening, closing, and erosion operations. Larger segments are filtered by convexity, measured as the ratio of the area of each segment relative to the area of its convex hull. Segments with convexity less than 0.85 become unlabelled. Lastly, the merged labels from  $k$ -means clustering of the EM and thresholding of the FM are intersected with the Voronoi diagram to result in a final segmentation mask. Pairs of segmentation masks and EM images are then used to train an instance of ResNet-34 for organelle segmentation in the same manner as was described for fully supervised segmentation. Note that the fluorescence image was originally included as

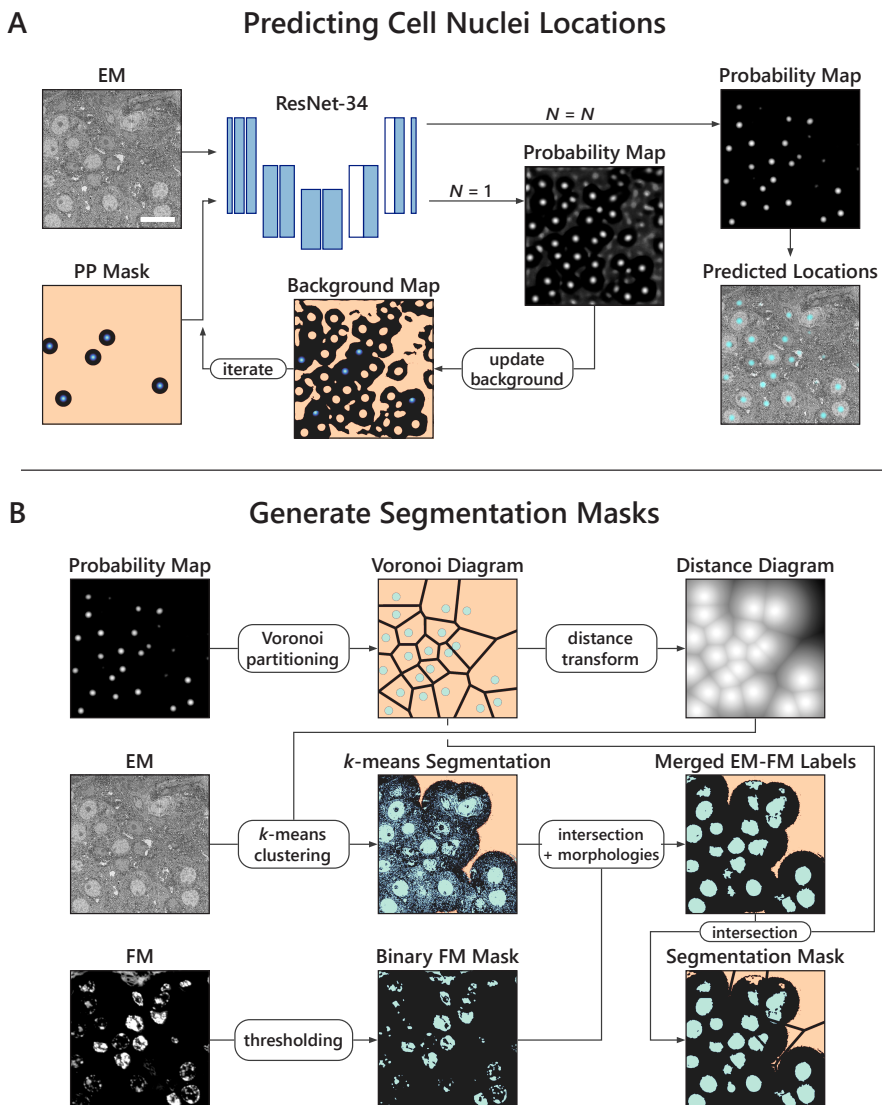


**Figure 3.S11.** Semi-automated image processing pipeline for generating segmentation masks from partial points annotation. (A) Partial points annotation is used to create Gaussian mask images to train an instance of ResNet-34 to predict nuclei locations. The predictions are refined through self-training to yield more accurate probability masks. (B) A Voronoi diagram based off of the probability map in (A) is merged with labelled images from *k*-means clustering to create segmentation masks for training a separate instance of ResNet-34 for organelle segmentation. Legend: white (or cyan) – nucleus; black – background; beige – unlabelled. Scale bar: (A) 10  $\mu\text{m}$  (scale bar in EM applies to all images).

a separate channel during  $k$ -means clustering, but the results from doing so were marginally worse: final IoU score of 67% vs 72%.

## 4.5. Supplementary material

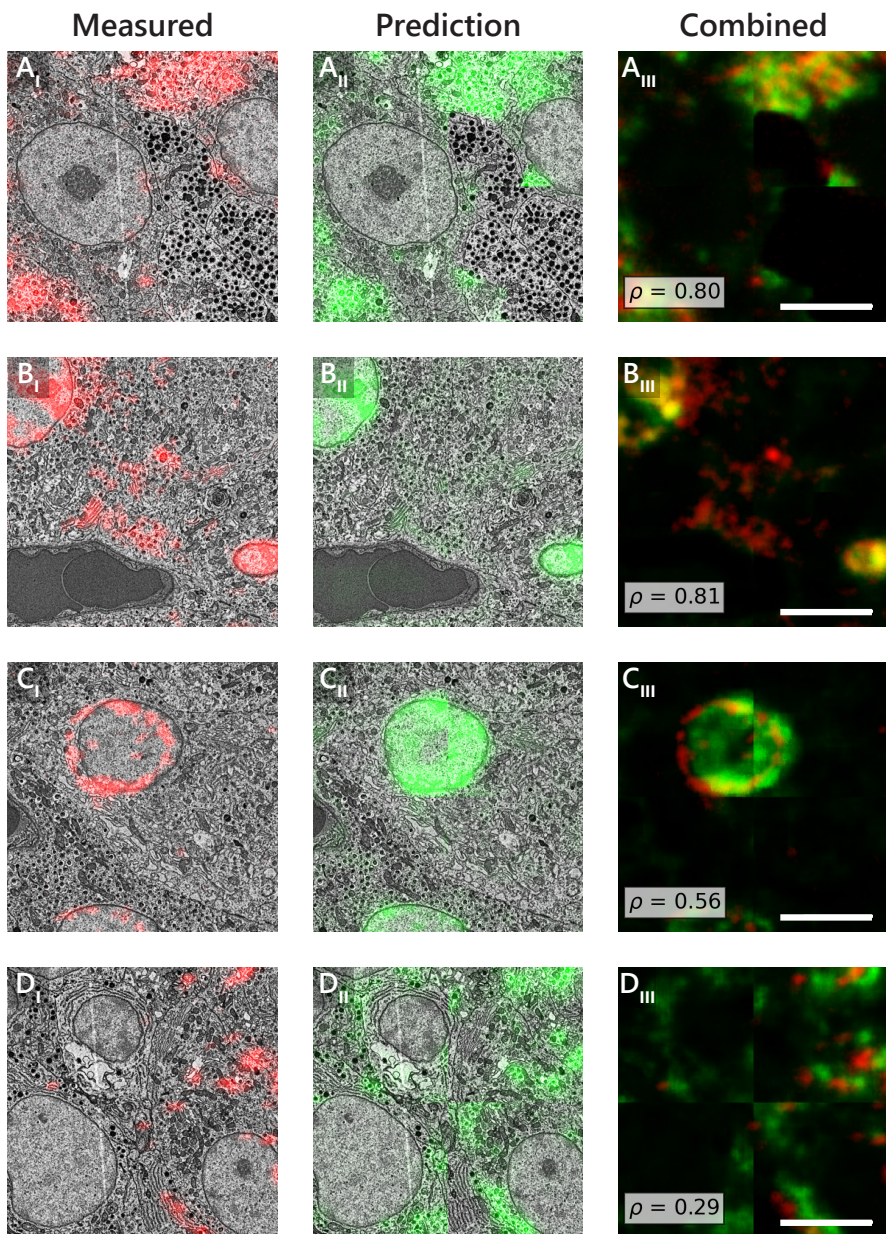


**Figure S1.** CLEMnet is able to perform nontrivial structural recognition tasks as well as mitigate issues inherent to fluorescence imaging. (Continued on next page...)

**Figure S1.** For each selected ROI (A-D), the measured fluorescence (left, red) and prediction (center, green) are overlaid onto the EM, and combined to show overlap and differences in signal intensity (right). (A) The network is able to distinguish between insulin and similar-looking glucagon granules, a difficult task for non-experts. (B) An instance of AF594 emission from 405 nm Hoechst excitation demonstrates that the network prediction is less susceptible to bleedthrough. (C) As the network generates predictions directly on structures within the EM, it is able to compensate for errors in the EM-FM registration near the edges of the field of view where the registration may be extrapolated. (D) The network is for the same reason also less susceptible to off-axis aberrations such as vignetting, which results in diminished signal at the corners of the fluorescence field of view. Note that several predictions are stitched together to compose the predicted image shown, at times giving rise to edge artefacts. Scale bars: (A-D) 5  $\mu\text{m}$ .

# REFERENCES

- [1] Ryan Lane et al. “Label-free fluorescence predictions from large-scale correlative light and electron microscopy data”. *In Preparation* (2022).
- [2] Eric M Christiansen et al. “In silico labeling: predicting fluorescent labels in unlabeled images”. *Cell* 173.3 (2018), pp. 792–803.
- [3] Jeroen Kuipers, Pascal de Boer, and Ben NG Giepmans. “Scanning EM of non-heavy metal stained biosamples: Large-field of view, high contrast and highly efficient immunolabeling”. *Experimental Cell Research* 337.2 (2015), pp. 202–207.
- [4] Ryan Lane et al. “Optimization of negative stage bias potential for faster imaging in large-scale electron microscopy”. *Journal of structural biology: X* 5 (2021), p. 100046.
- [5] Thomas Muller-Reichert and Paul Verkade. *Correlative light and electron microscopy II*. Academic Press, 2014.
- [6] Perrine Paul-Gilloteaux et al. “eC-CLEM: flexible multidimensional registration software for correlative microscopies”. *Nature methods* 14.2 (2017), pp. 102–103.
- [7] Matthew RG Russell et al. “3D correlative light and electron microscopy of cultured cells using serial blockface scanning electron microscopy”. *Journal of Cell Science* 130.1 (2017), pp. 278–291.
- [8] Pascal De Boer, Jacob P Hoogenboom, and Ben NG Giepmans. “Correlated light and electron microscopy: ultrastructure lights up!” *Nature methods* 12.6 (2015), pp. 503–513.
- [9] Pascal de Boer et al. “Large-scale electron microscopy database for human type 1 diabetes”. *Nature communications* 11.1 (2020), pp. 1–9.
- [10] Carsten Dittmayer et al. “Preparation of samples for large-scale automated electron microscopy of tissue and cell ultrastructure”. *Microscopy and Microanalysis* 27.4 (2021), pp. 815–827.
- [11] Kaiming He et al. “Deep residual learning for image recognition”. *Proceedings of the IEEE conference on computer vision and pattern recognition*. 2016, pp. 770–778.
- [12] Michał Januszewski et al. “High-precision automated reconstruction of neurons with flood-filling networks”. *Nature methods* 15.8 (2018), pp. 605–610.
- [13] Jeffrey M Ede. “Deep learning in electron microscopy”. *Machine Learning: Science and Technology* 2.1 (2021), p. 011004.

- [14] Shin-ya Takemura et al. “A visual motion detection circuit suggested by Drosophila connectomics”. *Nature* 500.7461 (2013), pp. 175–181.
- [15] Moritz Helmstaedter. “Cellular-resolution connectomics: challenges of dense neural circuit reconstruction”. *Nature methods* 10.6 (2013), pp. 501–507.
- [16] Gary B Huang and Stephen Plaza. “Identifying synapses using deep and wide multiscale recursive networks”. *arXiv preprint arXiv:1409.1789* (2014).
- [17] Larissa Heinrich et al. “Synaptic cleft segmentation in non-isotropic volume electron microscopy of the complete drosophila brain”. *International Conference on Medical Image Computing and Computer-Assisted Intervention*. Springer. 2018, pp. 317–325.
- [18] Jing Liu et al. “Automatic reconstruction of mitochondria and endoplasmic reticulum in electron microscopy volumes by deep learning”. *Frontiers in neuroscience* 14 (2020), p. 599.
- [19] Helen Spiers et al. “Deep learning for automatic segmentation of the nuclear envelope in electron microscopy data, trained with volunteer segmentations”. *Traffic* (2021).
- [20] Larissa Heinrich et al. “Automatic whole cell organelle segmentation in volumetric electron microscopy”. *bioRxiv* (2020).
- [21] Chawin Ounkomol et al. “Label-free prediction of three-dimensional fluorescence images from transmitted-light microscopy”. *Nature methods* 15.11 (2018), pp. 917–920.
- [22] Rick Seifert et al. “DeepCLEM: automated registration for correlative light and electron microscopy using deep learning”. *F1000Research* 9.1275 (2020), p. 1275.
- [23] Nalan Liv et al. “Simultaneous correlative scanning electron and high-NA fluorescence microscopy”. *PloS one* 8.2 (2013), e55707.
- [24] AC Zonnevylle et al. “Integration of a high-NA light microscope in a scanning electron microscope”. *Journal of microscopy* 252.1 (2013), pp. 58–70.
- [25] Martijn T Haring et al. “Automated sub-5 nm image registration in integrated correlative fluorescence and electron microscopy using cathodoluminescence pointers”. *Scientific reports* 7.1 (2017), pp. 1–9.
- [26] Özgün Çiçek et al. “3D U-Net: learning dense volumetric segmentation from sparse annotation”. *International conference on medical image computing and computer-assisted intervention*. Springer. 2016, pp. 424–432.
- [27] Raimond BG Ravelli et al. “Destruction of tissue, cells and organelles in type 1 diabetic rats presented at macromolecular resolution”. *Scientific reports* 3.1 (2013), pp. 1–6.
- [28] Andreas Müller et al. “3D FIB-SEM reconstruction of microtubule–organelle interaction in whole primary mouse  $\beta$  cells”. *Journal of Cell Biology* 220.2 (2021).
- [29] Larissa Heinrich et al. “Whole-cell organelle segmentation in volume electron microscopy”. *Nature* 599.7883 (2021), pp. 141–146.

- [30] Ryan W Conrad and Kedar Narayan. “Instance segmentation of mitochondria in electron microscopy images with a generalist deep learning model.” *bioRxiv* (2022).
- [31] Hui Qu et al. “Weakly Supervised Deep Nuclei Segmentation Using Partial Points Annotation in Histopathology Images”. *IEEE Transactions on Medical Imaging* 39.11 (2020), pp. 3655–3666.
- [32] Sven Dorkenwald et al. “Automated synaptic connectivity inference for volume electron microscopy”. *Nature methods* 14.4 (2017), pp. 435–442.
- [33] Joris Roels et al. “Domain adaptive segmentation in volume electron microscopy imaging”. *2019 IEEE 16th International Symposium on Biomedical Imaging (ISBI 2019)*. IEEE. 2019, pp. 1519–1522.
- [34] Ena Sokol et al. “Large-scale electron microscopy maps of patient skin and mucosa provide insight into pathogenesis of blistering diseases”. *Journal of Investigative Dermatology* 135.7 (2015), pp. 1763–1770.
- [35] Olaf Ronneberger, Philipp Fischer, and Thomas Brox. “U-net: Convolutional networks for biomedical image segmentation”. *International Conference on Medical image computing and computer-assisted intervention*. Springer. 2015, pp. 234–241.
- [36] Luuk WP Balkenende. “CLEMnet: Predicting fluorescence in electron microscopy images”. MEP thesis. Delft University of Technology, 2020.
- [37] Martín Abadi et al. *TensorFlow: Large-Scale Machine Learning on Heterogeneous Systems*. Software available from tensorflow.org. 2015. URL: <https://www.tensorflow.org/>.
- [38] François Chollet et al. *Keras*. <https://keras.io>. 2015.
- [39] Ryan Lane et al. “Integrated array tomography for 3D correlative light and electron microscopy”. *Frontiers in neuroscience* (2022).
- [40] Stephan Saalfeld et al. “CATMAID: collaborative annotation toolkit for massive amounts of image data”. *Bioinformatics* 25.15 (2009), pp. 1984–1986.
- [41] Patrice Y Simard, David Steinkraus, John C Platt, et al. “Best practices for convolutional neural networks applied to visual document analysis.” *Icdar*. Vol. 3. 2003. 2003.
- [42] Alexey Dosovitskiy et al. “Discriminative unsupervised feature learning with convolutional neural networks”. *Advances in neural information processing systems* 27 (2014), pp. 766–774.
- [43] David C Joy. “Noise and its effects on the low-voltage SEM”. *Biological Low-Voltage Scanning Electron Microscopy*. Springer, 2008, pp. 129–144.
- [44] Pavel Yakubovskiy. *Segmentation Models*. [https://github.com/qubvel/segmentation\\_models](https://github.com/qubvel/segmentation_models). 2019.

# 5

## VALORISATION, OUTLOOK, AND CONCLUSION

### 5.1. Prospects for integrated array tomography

This thesis presents a novel workflow for three-dimensional correlative light and electron microscopy (3D CLEM) in the form of integrated array tomography. The method involves correlative imaging of and volume reconstruction from serial sections of biological tissue using an integrated fluorescence and electron microscope, which offers several advantages over alternative approaches for 3D CLEM.

- (I) Semi-automated imaging and fully-automated registration facilitate the correlative acquisition of large numbers of serial sections. We have demonstrated the scalability of our method to 64 sections of zebrafish pancreas in which the only limitation was on the number of serial sections that were prepared (Chapter 3). Additionally, the correlative reconstruction routine supports the alignment of an arbitrarily large number of sections.
- (II) *In-situ* targeting of ROIs expedites throughput by limiting imaging volumes to those regions expressed by fluorescence. In practice we have experienced tenfold decreases in imaging volume with corresponding reductions to acquisition times and dataset sizes (Chapter 3).
- (III) Because the specimen is simultaneously prepared for both FM and EM, the reconstructed volumes of correlative data have matching axial resolution. This means that the fluorescence data does not have to be projected or interpolated in  $z$  as is the case with certain sequential CLEM approaches. Furthermore, specimen warping and shrinkage between imaging modalities, which might otherwise occur in conventional array tomography methods, is prevented due to the absence of intermediate sample preparation.

- (IV) Precise overlay of biological molecules and structural context at high resolution is achievable in all three dimensions. We have demonstrated sub-100 nm typical overlay accuracy and worst-case-scenario misalignment of ~1 µm (Chapter 3).
- (V) Array tomography allows for re-evaluation of sections, if necessary, as opposed to serial blockface (SBF-SEM) or focused ion beam (FIB-SEM) techniques in which the specimen is destroyed as it is imaged.

While the method has its advantages, it is not, of course, without its limitations. Chief among them is the manual intervention needed for certain navigation and focusing tasks. Although the ability to detect regions of interest on-the-fly based on fluorescence is one of the main benefits of integrated array tomography, these regions must still be navigated to manually. To further automate the workflow, ROI positions for each section could be extrapolated based on an initial selection, as in Gabarre et al. [1]. Slight variations in section shape can be accounted for by a geometrical transformation of each serial section to the reference section from which the ROI was initially selected. An alternative approach for fully automated ROI detection and navigation involves recognition of the fluorescent markers of interest based on artificial intelligence (AI). Delpiano et al. [2] investigated this approach for the automated detection of fluorescent cells, finding that current state-of-the-art machine learning techniques required significant quantities of ground truth training data as well as postprocessing for separating merged cells. Thus, while fully automated AI-based approaches for ROI detection may not yet be suitable, opportunities for extending automated navigation do exist.

The other component of the workflow that stands to benefit most from automation are the EM and FM focusing routines. Effort has been invested in developing an autofocus procedure for the fluorescence microscope (Appendix A), which involved analyzing the performance of several dozen focus metrics. The results were ultimately incorporated into the autofocus routine implemented in the integrated microscope control software, Odemis. Developing an EM autofocus routine has been a more complex task as it requires access to proprietary software for controlling the lens voltages. With the development of FAST-EM [3], access to these controls has become available through an extension to Odemis. The potential for fully automated focus routines is therefore in place, however, questions surrounding the robustness of these routines remain. Therefore, the choice was made to forgo autofocusing routines during large-scale acquisitions to prevent the possibility of a failure compromising subsequent acquisitions.

Many of the sub-routines involved in integrated array tomography have been fully automated (Figure S1). This is particularly true of the alignment and reconstruction procedures, which are executed through a series of interactive jupyter notebooks that have been made publicly available.<sup>1</sup> The section detection phase is similarly guided by a series of jupyter notebooks that perform the serial section segmentation and tile mapping (partitioning the ROI into low- and high-magnification

<sup>1</sup><https://github.com/hoogenboom-group/iCAT-workflow>

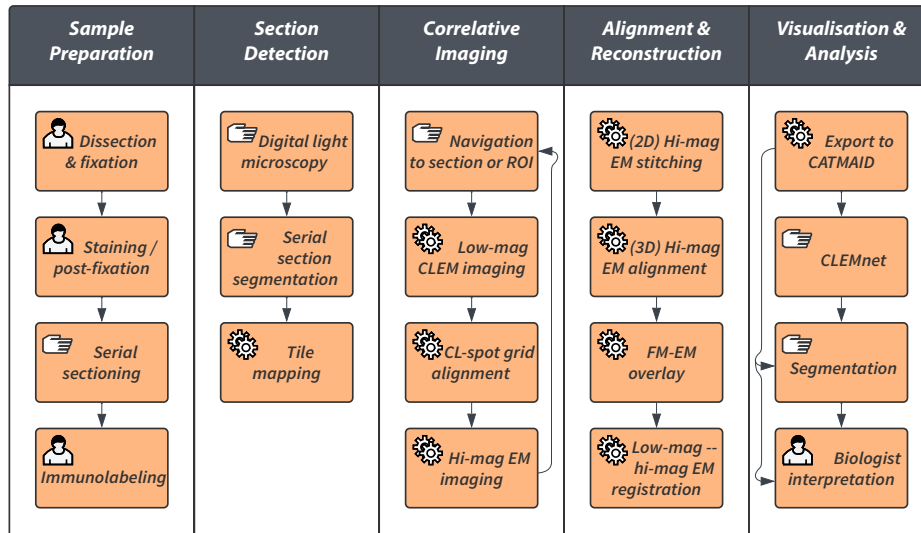


**Figure S1.** Workflow diagram for integrated array tomography. Icons represent the extent to which each subroutine is automated: human – fully manual, hand – semi-automated or human-assisted, gears – fully automated. Note that a sub-routine may still be considered fully automated even if it might benefit from further automation (e.g. implementing auto-focus within high-magnification EM imaging).

image tiles) sub-routines.<sup>2</sup> Note that the segmentation step is denoted as semi-automatic in Figure S1 since connected ribbons of serial sections often require manual correction to obtain an optimal instance segmentation. Software for acquiring grids of image tiles (including the CL-spot alignment during low-magnification CLEM) are available as a plugin in Odemis,<sup>3</sup> which is fully open-source. This level of automation should in principle enable anyone with familiarity in fluorescence and electron microscopy as well as programming experience in Python to follow the integrated array tomography workflow with relative ease.

Challenges pertaining to sample preparation were described in Section 3.4. In short, fluorescent probes, such as fluorescent proteins, are generally incompatible with conventional fixation and staining procedures used for EM. Despite efforts towards developing probes for retaining fluorescence post-embedding [4, 5, 6], compromises between the strength of the fluorescence and the quality of the ultrastructure remain unavoidable. These compromises are made more difficult by conducting fluorescence imaging in high vacuum conditions where intensities are expected to be lower as fluorescent probes are typically optimized for (if not dependent on) aqueous environments [6].

Finally, fluorescence preservation or post-embedding relabeling of genetic flu-

<sup>2</sup><https://github.com/hoogenboom-group/secdetect>

<sup>3</sup><https://github.com/delmic/odemis>

orophores may facilitate linking ultrastructural observations to live, intravital fluorescence microscopy. Prior to array tomography, photoactivatable probes could be used to mark where cells can be assessed for function. These markers could then be activated as part of the integrated workflow, thus linking the ultrastructural data to not only fluorescence expression but also to function and development [7]. If combined with advances in automation, this could lead towards the development of dedicated integrated CLEM instruments with complete and fully automated workflows for high-throughput and high-yield volume CLEM.

## 5.2. Applications for multibeam SEM

For certain applications such as connectomics, in which the goal is to comprehensively reconstruct neuronal circuitry [8], fluorescence-based ROI targeting may be insufficient for limiting imaging volumes. The brains of small organisms, for example, can easily reach cubic millimeter volumes. Assuming 5 nm isotropic pixel size (synaptic resolution), such volumes would take decades to image with a single electron beam due to limits on detector bandwidth and the amount of current that can be concentrated into a focused probe [9, 10]. For this reason a multibeam SEM, which parallelizes electron beam scanning by focusing multiple electron beamlets onto a specimen, has long been a research topic both inside [11, 12, 13] and outside [9, 14, 15, 16] Delft. Recently, early adopter units of a multibeam system (FAST-EM, [3]) have been installed at UMC Groningen and TU Delft.

Despite its dramatic increases in imaging speeds, multibeam SEM bears the same limitation as conventional SEM with respect to the inability to provide inherent biological specificity. While for single beam SEM we addressed this problem by integrating a fluorescence microscope into the vacuum chamber, the same cannot be done for FAST-EM as sections are placed on a (nontransparent) scintillator substrate, the light from which serves as the detection mechanism. Alternatively, biological specificity could be added artificially (Fig S2). This could be done by preparing the same specimen for both FAST-EM and integrated array tomography. After initial processing of the specimen, the vast majority of serial sections would be placed onto a scintillator substrate for FAST-EM, while a small fraction ( $\leq 20$ ) would be reserved for the integrated microscope. Following correlative imaging and reconstruction, the datasets would be used for training CLEMnet to predict on FAST-EM data. We have already seen that CLEMnet is capable of generating predictions on EM data acquired with different imaging settings than it was trained on (Section 4.2.4). Early results have indicated that CLEMnet has the potential to generate fluorescence predictions on optical STEM data as well, given minor image processing augmentations [17].

There are, however, caveats to this approach that must be taken into consideration. First, there is no concrete means of verifying the fluorescence prediction as there is no measured fluorescence to serve as ground truth. Less precise verification methods do exist such as validating the predictions on sections adjacent to those for which the fluorescence was recorded. This may only be reliable, however, for structures significantly larger than the section thickness (e.g. cell nuclei,

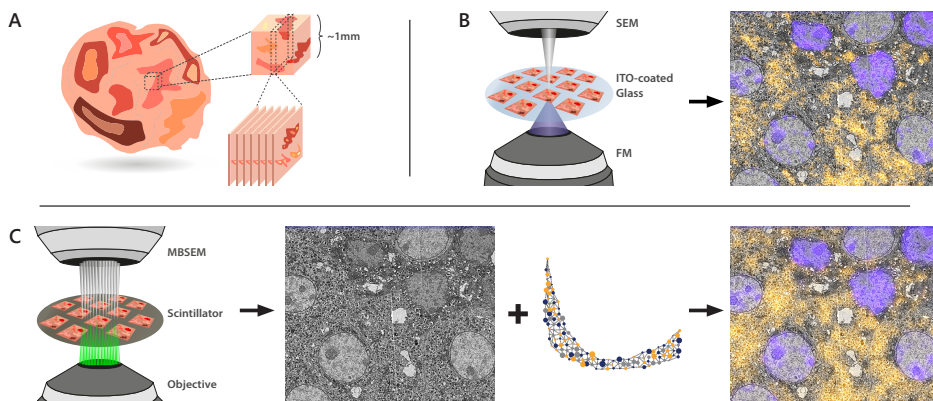


**Figure S2.** Prospective workflow for adding AI-generated fluorescence to multibeam SEM data. (A) Ultrathin sections are prepared for EM with some fraction additionally prepared for integrated CLEM and placed onto ITO-coated glass (B). A correlative dataset is then recorded via integrated array tomography. (C) The vast majority of the serial sections are placed onto a scintillator substrate and acquired by multibeam SEM. The correlative dataset (acquired in B) could then be used to train a neural network to generate predictions of the fluorescence signal.

but not mitochondria, lysosomes, or granules). An alternative approach would be to manually segment the labelled structures in a subset of the FAST-EM data to establish a quasi-ground truth set for assessing the accuracy of the prediction. Another caveat is that there will be sections missing from the FAST-EM imaging volume due to the transfer of sections to ITO-coated glass. However, because the transferred sections will still be imaged with (single beam) SEM, they can be inserted into the image stack for 3D reconstruction, provided they are imaged at the same resolution.

## 5.3. Conclusion

The goal of this thesis was to develop a method for 3D CLEM utilizing an integrated light and electron microscope. We began with the realization that conventional SEM imaging of weakly-stained specimen prepared for fluorescence microscopy required highly impractical dwell times. Thus, we implemented a negative bias potential to enhance the backscattered electron (BSE) yield. An empirical optimization of the stage bias, informed by electron optics simulations, ultimately led to orders of magnitude improvement in the signal-to-noise (SNR) ratio. This solved the throughput problem for large-scale, integrated CLEM, which allowed us to develop a scalable workflow for integrated array tomography. The method we created further expedited acquisitions by limiting high-resolution EM to select ROI targeted by fluorescence expression, while high precision EM-FM overlay is achieved using cathodoluminescent markers [18].

After successfully demonstrating our workflow on pancreatic tissue from different organisms, we explored the potential for large-scale CLEM datasets to be used as training data for machine learning applications. It was found that a modified U-net [19], trained on such correlative datasets, was capable of generating high-fidelity predictions of the fluorescence signal from EM. As linking structure to function is one of the primary goals in cell biology, we then tested whether this data would be advantageous in organelle segmentation. While naive approaches of thresholding the measured and predicted fluorescence signals for use as segmentation masks proved unremarkable, more complicated mask generation techniques seem promising. Finally, we discussed the ways in which integrated array tomography could be expanded into a fully automated workflow as well as potential applications for multibeam SEM. Coupling these improvements together with advances in fluorescent probes would bring integrated array tomography to the forefront of volume CLEM, lending new insight to a host of questions within structural biology.

# REFERENCES

- [1] Sergio Gabarre et al. “A workflow for streamlined acquisition and correlation of serial regions of interest in array tomography”. *BMC biology* 19.1 (2021), pp. 1–15.
- [2] J Delpiano et al. “Automated detection of fluorescent cells in in-resin fluorescence sections for integrated light and electron microscopy”. *Journal of microscopy* 271.1 (2018), pp. 109–119.
- [3] Job Fermie et al. “High-throughput imaging of biological samples with Delmic’s FAST-EM”. *Microscopy and Microanalysis* 27.S1 (2021), pp. 558–560.
- [4] Shigeki Watanabe et al. “Protein localization in electron micrographs using fluorescence nanoscopy”. *Nature methods* 8.1 (2011), pp. 80–84.
- [5] Wanda Kukulski et al. “Correlated fluorescence and 3D electron microscopy with high sensitivity and spatial precision”. *Journal of Cell Biology* 192.1 (2011), pp. 111–119.
- [6] Christopher J Peddie et al. “Correlative and integrated light and electron microscopy of in-resin GFP fluorescence, used to localise diacylglycerol in mammalian cells”. *Ultramicroscopy* 143 (2014), pp. 3–14.
- [7] Lucy M Collinson, Elizabeth C Carroll, and Jacob P Hoogenboom. “Correlating 3D light to 3D electron microscopy for systems biology”. *Current Opinion in Biomedical Engineering* 3 (2017), pp. 49–55.
- [8] Kevin L Briggman and Davi D Bock. “Volume electron microscopy for neuronal circuit reconstruction”. *Current opinion in neurobiology* 22.1 (2012), pp. 154–161.
- [9] AL Eberle et al. “High-resolution, high-throughput imaging with a multibeam scanning electron microscope”. *Journal of microscopy* 259.2 (2015), pp. 114–120.
- [10] Jörgen Kornfeld and Winfried Denk. “Progress and remaining challenges in high-throughput volume electron microscopy”. *Current opinion in neurobiology* 50 (2018), pp. 261–267.
- [11] Y. Zhang. “A 100-electron-beam source from a high brightness Schottky emitter for fast patterning applications”. PhD thesis. Delft University of Technology, 2008.
- [12] A. Mohammadi-Gheidari. “196 Beams in a Scanning Electron Microscope”. PhD thesis. Delft University of Technology, 2013.
- [13] Y. Ren. “Imaging systems in the Delft Multi-Beam Scanning Electron Microscope 1”. PhD thesis. Delft University of Technology, 2017.

- [14] Anna Lena Eberle and Dirk Zeidler. “Multi-beam scanning electron microscopy for high-throughput imaging in connectomics research”. *Frontiers in Neuroanatomy* (2018), p. 112.
- [15] C Riedesel et al. “First demonstration of a 331-beam SEM”. *Metrology, Inspection, and Process Control for Microlithography XXXIII*. Vol. 10959. SPIE. 2019, pp. 669–673.
- [16] Donglai Wei et al. “MitoEM dataset: large-scale 3D mitochondria instance segmentation from EM images”. *International Conference on Medical Image Computing and Computer-Assisted Intervention*. Springer. 2020, pp. 66–76.
- [17] M. Abels. “On CLEMnet: Fluorescence prediction on electron microscopy data without complementary fluorescence data”. BEP thesis. Delft University of Technology, 2022.
- [18] Martijn T Haring et al. “Automated sub-5 nm image registration in integrated correlative fluorescence and electron microscopy using cathodoluminescence pointers”. *Scientific reports* 7.1 (2017), pp. 1–9.
- [19] Olaf Ronneberger, Philipp Fischer, and Thomas Brox. “U-net: Convolutional networks for biomedical image segmentation”. *International Conference on Medical image computing and computer-assisted intervention*. Springer. 2015, pp. 234–241.

# A

## AUTOMATIC FOCUSING OF THE FLUORESCENCE MICROSCOPE

### 1.1. Original autofocus implementation

Acquisition of in-focus fluorescence microscopy (FM) images comprises an essential aspect of the workflow for integrated array tomography. Focusing the objective lens of the fluorescence microscope can be done manually or by an autofocus routine implemented in the microscope control software, Odemis,<sup>1</sup> which performs a dichotomic search for optimal focus (Algorithm 1). In this routine an image is recorded at the initial position of the objective lens, after which the lens is translated upwards and downwards by a fixed amount. At each position the focus level is measured by the variance of Laplacian (Algorithm 2).

The objective is vertically translated by a given step size in the direction that increases the focus measure until a decrease is observed. The objective is then iteratively raised and lowered by smaller and smaller increments until a minimum change in the focus measure is reached or the algorithm exceeds the maximum number of attempts. While conceptually sound, it was observed that the autofocus routine is susceptible to errors (Figure S1), even when executed with seemingly favorable initial conditions (i.e. beginning the routine while in focus). The primary issue is thought to originate from an open loop focus actuator, resulting in objective movements with limited precision. This is evidenced by a significant drop in the focus measure for an image acquired as the objective returns to its starting position (Figure S1, yellow circle). Photobleaching may also play a role in the decrease of the focus measure.

---

<sup>1</sup><https://github.com/delmic/odemis>

**Algorithm 1** Odemis autofocus routine.

---

```

while  $s \geq s_{min}$  and  $n < n_{max}$  do
     $M_{mid} \leftarrow \text{acquire\_and\_assess}()$ 
     $z \leftarrow +s$                                  $\triangleright$  Objective is raised
     $M_{up} \leftarrow \text{acquire\_and\_assess}()$ 
     $z \leftarrow -2s$                              $\triangleright$  Objective is lowered
     $M_{dwn} \leftarrow \text{acquire\_and\_assess}()$ 
    if  $M_{up} == M_{dwn}$  then                   $\triangleright$  Minimized step size reached
        break
    else if  $M_{up} > M_{mid}$  then
         $z \leftarrow z_0 + s$ 
    else if  $M_{dwn} > M_{mid}$  then
         $z \leftarrow z_0 - s$ 
    else                                          $\triangleright$  Best focus found at center
         $z \leftarrow z_0$ 
         $s \leftarrow s/2$                             $\triangleright$  Reduce step size by half
    end if
     $n \leftarrow n + 1$ 
end while

```

---

**Algorithm 2** Variance of Laplacian.

---


$$L \leftarrow \begin{pmatrix} 1/6 & 2/3 & 1/6 \\ 2/3 & -10/3 & 2/3 \\ 1/6 & 2/3 & 1/6 \end{pmatrix}$$

$\triangleright$  Laplacian kernel

$$I^* \leftarrow \text{convolve}(I, L)$$
**return**  $\text{var}(I^*)$ 


---

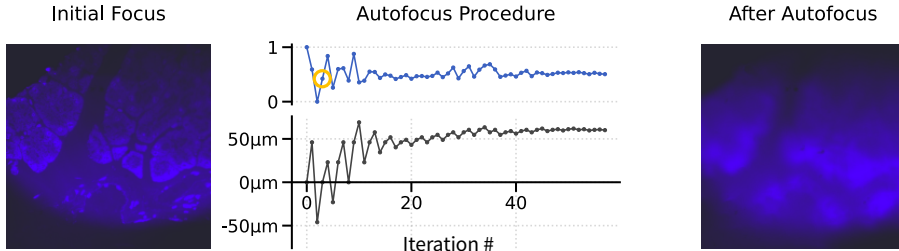


**Figure S1.** Odemis autofocus routine converging on an out-of-focus image. (Left) image from the initial focus position, (center) data from the iterative procedure, (right) image from the final focus position. The two plots show the normalized focus measures (top) and the position of the microscope objective (below) resulting from the dichotomic search. The yellow circle marks the decrease in focus measure when the objective returns to its starting position.

## 1.2. Analysis of FM focus sweeps

The results of Figure S1 suggest that a dichotomic search may not be a suitable approach for the autofocus algorithm. Moreover, as will be shown later, Laplacian-based focus measures tend to skew more highly for over-focused images. In order to develop a more robust autofocus algorithm, a series of focus sweeps were conducted over several different  $z$  ranges, regions of interest, and fluorescence channels (Figure S2). The focus sweeps are analyzed by a selection of different focus metrics (Table A.1) compiled from Pertuz et al. [1], which examines different focus metrics across a variety of imaging settings and applications. Many of the metrics belong to particular subgroups such as those that involve computing the image gradient (GRAE, GRAT, and GRAS) or the Laplacian (LAPE, LAMP, LAPV, and LAPD). Metrics within each subgroup tend to respond similarly to noise, contrast and window size such that the relative performance depends highly on the particular set of imaging settings [1]. The focus metrics were translated from their original Matlab implementation [2] to Python [3].

To assess the relative performance of each focus metric, we perform a consensus analysis to determine how far off each metric is from selecting the correct focus position (Figure S3). For each focus sweep, the correct focus position is determined by taking the modal value among the 20 focus measures. To better visualize which metrics more frequently return out-of-focus positions, the further away from the modal value a particular curve peaks, the more red that curve appears in the plot. From this analysis it is straightforward to eliminate metrics such as ACMO, CURV, and HISE for which there are multiple red curves. The Laplacian-based metrics can likewise be discarded for their bias towards over-focused images. As expected, there is also a certain degree of redundancy within subgroups. For instance, GRAS (the squared gradient) is virtually equal to GRAT (the thresholded gradient).

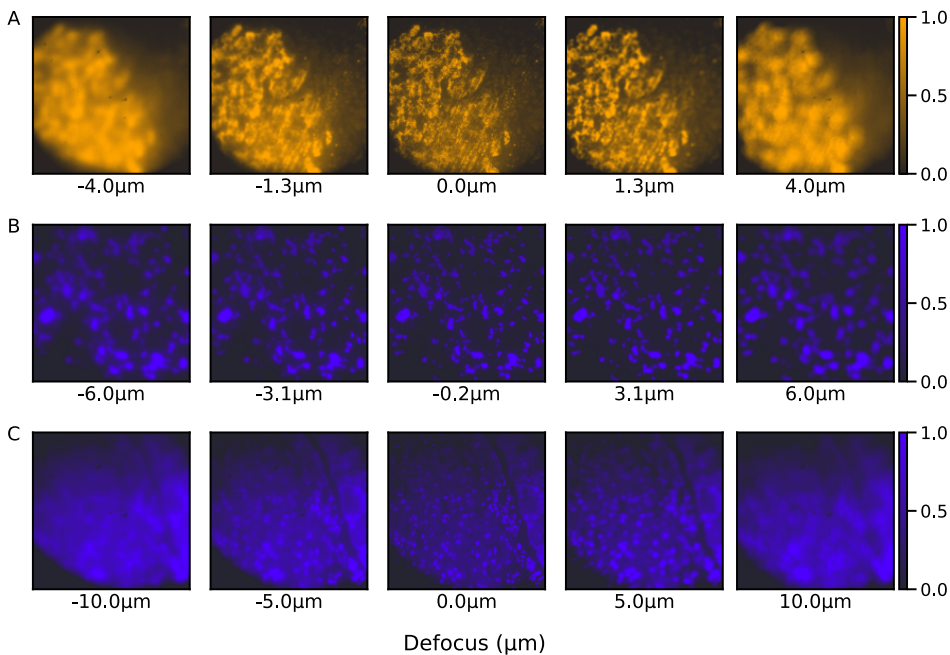


**Figure S2.** Sample focus sweeps of the fluorescence microscope. (A) An 8  $\mu\text{m}$  sweep over an islet of Langerhans with 555 nm excitation. (B) A 12  $\mu\text{m}$  sweep over fluorescent debris on the ITO-coated glass substrate with 405 nm excitation. (C) A 20  $\mu\text{m}$  sweep over an islet of Langerhans with 405 nm excitation.

After consolidating the candidate focus metrics, we can examine more stringent imaging conditions to explore where the different methods might diverge. To this end, a second round of focus sweeps was recorded in which the images were acquired with decreased exposure times and resolution to present the focus metrics with more challenging settings. The sweeps were then analyzed with the filtered set of candidate focus metrics (Figure S4). The same consensus analysis that was done for the initial set of focus sweeps could not be repeated as the modal value was often erroneous as determined by visual inspection. The correct focus position therefore had to be determined by eye.

One metric in particular, TENV, which computes the variance of the image after applying horizontal and vertical Sobel edge detection (Algorithm 3), consistently returned the correct focus position independent of scene, exposure time, and resolution (Figure S4A & B). A new autofocus routine was therefore developed with TENV as the focus metric and a simple sweep through focus to set the objective position (Algorithm 4). To improve precision, the objective position is refined with quadratic interpolation. The new autofocus routine was implemented as an Odemis plugin which could then be integrated into the automated tile acquisitions. Validation was done by automated fluorescence acquisitions on sections of fluo-

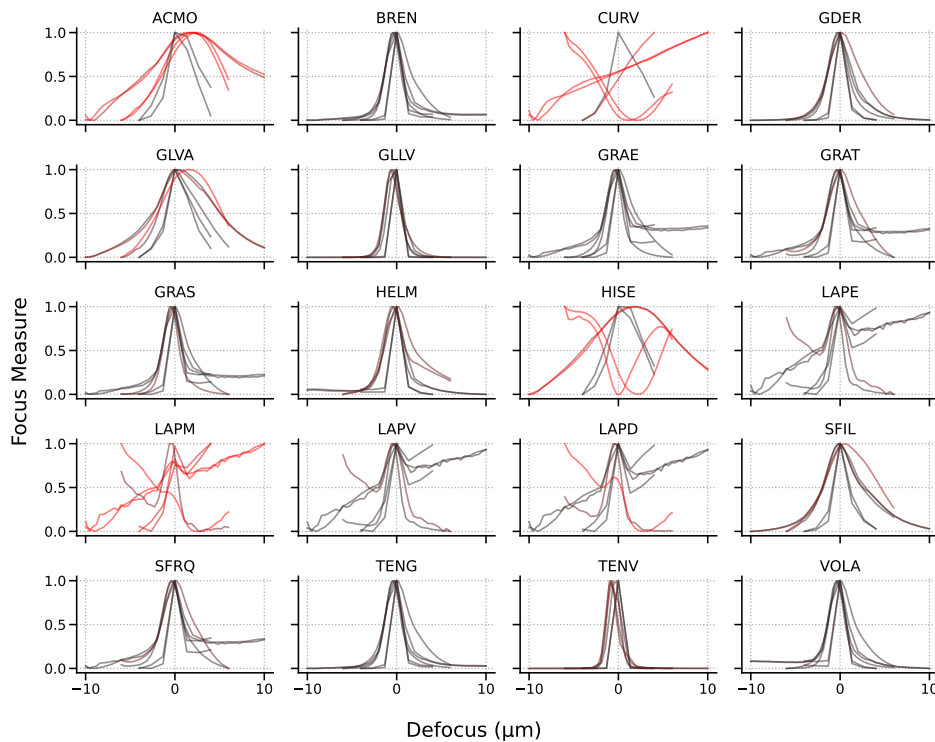


**Figure S3.** Analysis of 20 potential focus metrics. Each subplot shows the focus measures across the six focus sweeps for a particular metric. A black color indicates that the peak of the curve is in the consensus (i.e. that the metric returned the correct focus position for that particular sweep). Red indicates that the peak of the curve falls outside the consensus, with brighter red signifying that the peak is further away.

rescent HeLa cells embedded in Lowicryl HM20 (Figure S5), resulting in a grid of sharp, well-focused fluorescence images.

**Algorithm 3** Tenengrad variance.

---


$$S_H \leftarrow \begin{pmatrix} 1 & 2 & 1 \\ 0 & 0 & 0 \\ -1 & -2 & -1 \end{pmatrix} \quad \triangleright \text{Horizontal Sobel filter}$$

$$S_V \leftarrow \begin{pmatrix} 1 & 0 & -1 \\ 2 & 0 & -2 \\ 1 & 0 & -1 \end{pmatrix} \quad \triangleright \text{Vertical Sobel filter}$$

$$I_H^* \leftarrow \text{convolve}(I, S_H)$$

$$I_V^* \leftarrow \text{convolve}(I, S_V)$$
**return**  $\text{var}((I_H^*)^2 + (I_V^*)^2)$ 


---

**Algorithm 4** Autofocus algorithm based on sweep through focus.

---


$$M_{max} = 0$$

$$z \leftarrow -\Delta z/2$$
**for**  $i$  **in range**  $N$  **do**

$$M \leftarrow \text{acquire\_and\_assess}()$$

$$M_{max} = \text{max}(M, M_{max})$$

$$z \leftarrow +\Delta z/N$$
**end for**

$$z \leftarrow \text{QIFFT}([M_{max-1}, M_{max}, M_{max+1}]) \quad \triangleright \text{Quadratic interpolation}$$


---

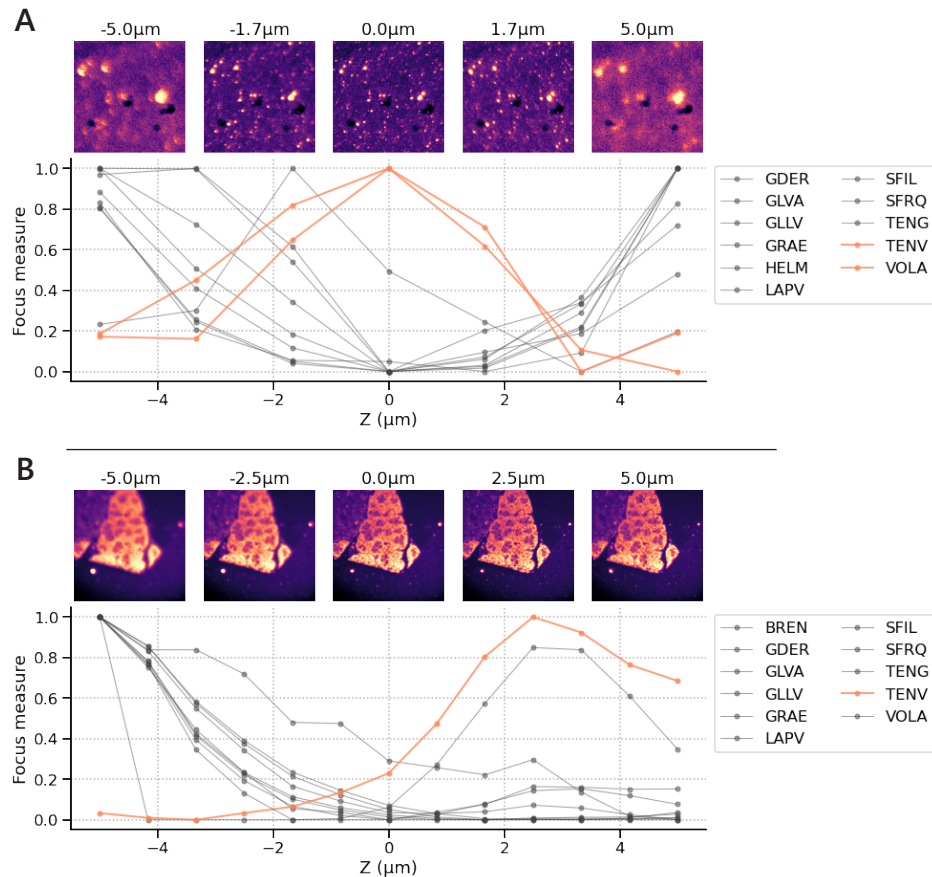


**Figure S4.** Select focus sweeps revealing the robustness of TENV as a focus metric for use with the fluorescence microscope. As many of the metrics peaked far from the apparent best focus level, the correct focus position was determined visually. (A) A relatively low resolution ( $256 \times 256$  px) focus sweep conducted on the ITO-coated glass background for which only TENV and VOLA yielded the correct focus position. (B) A focus sweep acquired on exocrine pancreas tissue with a relatively low exposure time (100 ms) for which only TENV yielded the correct focus position.

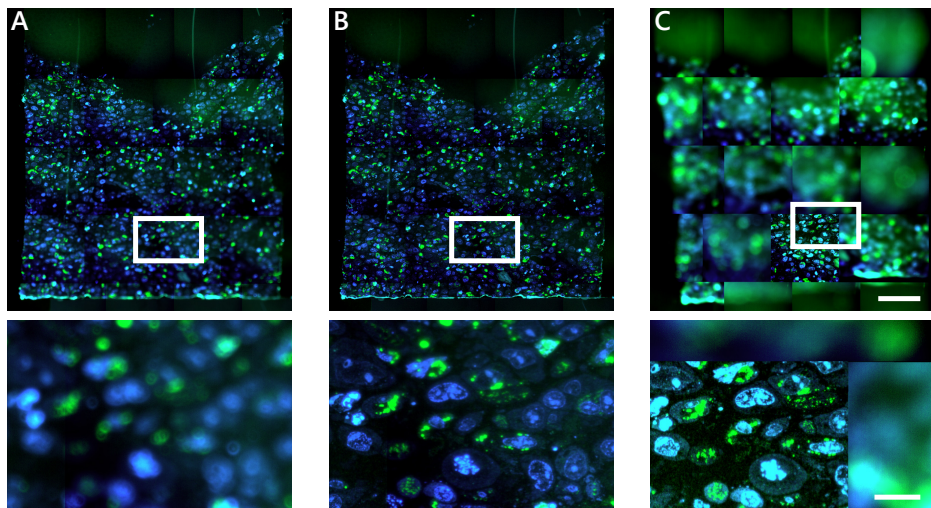


**Figure S5.** Autofocus routine based on focus sweeps and TENV yields best results for automated fluorescence imaging. (A) no autofocus routine, (B) the autofocus routine described here, and (C) the default autofocus routine implemented in Odemis. All automated fluorescence acquisitions were conducted on the same section of fluorescent HeLa cells. Scale bars: (A – C) 100  $\mu\text{m}$ ; (insets) 20  $\mu\text{m}$ .

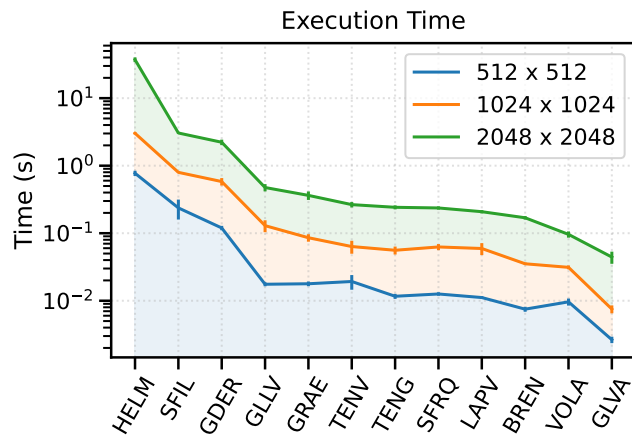


**Figure S6.** Execution times for the filtered set of candidate focus metrics. 512  $\times$  512, 1024  $\times$  1024, and 2048  $\times$  2048 denote the image dimensions.

**Table A.1.** Reference list for focus metrics.

	Focus metric	Reference
ACMO	Absolute central moment	[4]
BREN	Brenner's focus measure	[5]
CURV	Image curvature	[6]
GDER	Gaussian derivative	[7]
GLVA	Gray-level variance	[8]
GLVV	Gray-level local variance	[9]
GRAE	Energy of gradient	[10]
GRAT	Thresholded gradient	[5]
GRAS	Squared gradient	[11]
HELM	Helmlis's measure	[6]
HISE	Histogram entropy	[8]
LAPE	Energy of Laplacian	[10]
LAPM	Modified Laplacian	[12]
LAPV	Variance of Laplacian	[9]
LAPD	Diagonal Laplacian	[13]
SFIL	Steerable filters-based	[14]
SFRQ	Spatial frequency	[11]
TENG	Tenegrad	[8]
TENV	Tenengrad variance	[9]
VOLA	Vollat's correlation-based	[5]

# REFERENCES

- [1] Said Pertuz, Domenec Puig, and Miguel Angel Garcia. “Analysis of focus measure operators for shape-from-focus”. *Pattern Recognition* 46.5 (2013), pp. 1415–1432.
- [2] Said Pertuz. *Focus Measure*. Version 2.2.0.0. Aug. 2017. URL: <https://www.mathworks.com/matlabcentral/fileexchange/27314-focus-measure>.
- [3] Ryan Lane. *focus-metrics*. Version 0.1. June 2022. URL: <https://github.com/hogenboom-group/focus-metrics>.
- [4] Mukul V Shirvaikar. “An optimal measure for camera focus and exposure”. *Thirty-Sixth Southeastern Symposium on System Theory, 2004. Proceedings of the IEEE*. 2004, pp. 472–475.
- [5] Andrés Santos et al. “Evaluation of autofocus functions in molecular cytogenetic analysis”. *Journal of microscopy* 188.3 (1997), pp. 264–272.
- [6] Franz Stephan Helmlí and Stefan Scherer. “Adaptive shape from focus with an error estimation in light microscopy”. *ISPA 2001. Proceedings of the 2nd International Symposium on Image and Signal Processing and Analysis. In conjunction with 23rd International Conference on Information Technology Interfaces (IEEE Cat. IEEE*. 2001, pp. 188–193.
- [7] Jan-Mark Geusebroek et al. “Robust autofocusing in microscopy”. *Cytometry: The Journal of the International Society for Analytical Cytology* 39.1 (2000), pp. 1–9.
- [8] Eric Krotkov and J-P Martin. “Range from focus”. *Proceedings. 1986 IEEE International Conference on Robotics and Automation*. Vol. 3. IEEE. 1986, pp. 1093–1098.
- [9] José Luis Pech-Pacheco et al. “Diatom autofocusing in brightfield microscopy: a comparative study”. *Proceedings 15th International Conference on Pattern Recognition. ICPR-2000*. Vol. 3. IEEE. 2000, pp. 314–317.
- [10] Murali Subbarao, Tae-Sun Choi, and Arman Nikzad. “Focusing techniques”. *Machine Vision Applications, Architectures, and Systems Integration*. Vol. 1823. International Society for Optics and Photonics. 1992, pp. 163–174.
- [11] Ahmet M Eskicioglu and Paul S Fisher. “Image quality measures and their performance”. *IEEE Transactions on communications* 43.12 (1995), pp. 2959–2965.
- [12] Shree K Nayar and Yasuo Nakagawa. “Shape from focus: An effective approach for rough surfaces”. *Proceedings., IEEE International Conference on Robotics and Automation*. IEEE. 1990, pp. 218–225.

- [13] Andrea Thelen et al. “Improvements in shape-from-focus for holographic reconstructions with regard to focus operators, neighborhood-size, and height value interpolation”. *IEEE Transactions on Image Processing* 18.1 (2008), pp. 151–157.
- [14] Rashid Minhas et al. “3D shape from focus and depth map computation using steerable filters”. *International conference image analysis and recognition*. Springer. 2009, pp. 573–583.